



Universität Hamburg

DER FORSCHUNG | DER LEHRE | DER BILDUNG

Biophysical characterization of the pyrophosphatase NUDT9 and the NUDT9- homologous domain of the TRPM2 channel

Dissertation for the acquisition of a doctoral degree (Dr. rer. nat.)

at the Department of Chemistry

Faculty of Mathematics, Informatics and Natural Sciences

University of Hamburg

submitted by

Ellen Gattkowski

MAY 2021

This work was done from November 2016 to May 2021 at the Department of Chemistry,
University of Hamburg under the supervision of Prof. Dr. Henning Tidow.

1st reviewer: Prof. Dr. Henning Tidow

2nd reviewer: Dr. Ralf Fliegert

Date of Disputation: 2021/08/20

Table of Contents

Abstract	I
Zusammenfassung	III
Publications associated with this thesis	V
List of Figures	VI
List of Tables	IX
List of Abbreviations	XI
1 Introduction	1
1.1 Adenosine-diphosphate ribose (ADPR).....	1
1.2 ADPR generation and function in mitochondria.....	2
1.3 ADPR generation in the nucleus.....	3
1.4 ADPR generation in the cytosol.....	4
1.5 ADPR degradation by NUDIX enzymes.....	4
1.5.1 NUDT9.....	6
1.6 The TRPM2 channel is gated by ADPR.....	7
1.6.1 TRPM2 regulation by Ca ²⁺	11
1.6.2 TRPM2 regulation by temperature.....	12
1.6.3 ADPR-alternative TRPM2 agonists.....	13
1.6.4 Evolutionary adaption of the NUDT9H domain.....	15
2 Aim of the Thesis	15
3 Analysis of ligand-binding and resulting conformational changes in pyrophosphatase NUDT9	16
3.1 Abstract.....	16
3.2 Results.....	16
3.2.1 Expression and purification of NUDT9.....	16
3.2.2 NUDT9 binds ADPR as well as its derivative 2'-deoxy ADPR.....	17
3.2.3 Biophysical characterization of NUDT9 reveals sequential unfolding and large conformational changes upon substrate binding.....	21

TABLE OF CONTENTS

3.2.4	Mutation of the NUDIX box inactivates pyrophosphatase NUDT9.....	28
3.2.5	ADPR and 2'-deoxy-ADPR bind to the identical site as determined by NMR..	31
3.2.6	Development of a FRET probe for ADPR based on NUDT9	34
3.2.6.1	ADPR FRET sensor: NUDT9 fused to fluorescent proteins	35
3.2.6.2	ADPR FRET sensor: NUDT9 coupled to Alexa Fluor dyes.....	42
3.3	Discussion.....	47
3.3.1	2'-deoxy-ADPR is a novel ligand of the ADPR pyrophosphatase NUDT9	47
3.3.2	ADPR and 2'-deoxy-ADPR bind to the identical binding site in NUDT9.....	48
3.3.3	The NUDT9 E230I F231L mutant can bind but not hydrolyze ADPR and 2'- deoxy-ADPR	49
3.3.4	NUDT9 undergoes substantial conformational changes upon substrate binding.....	50
3.3.5	NUDT9 can be developed into an ADPR FRET sensor	52
3.3.5.1	Genetically encoded FRET sensor.....	52
3.3.5.2	Alexa Fluor labelled NUDT9.....	53
4	Calmodulin binding to and regulation of TRPM2.....	56
4.1	Abstract.....	56
4.2	Results.....	56
4.2.1	Identification and characterization of two novel Calmodulin binding sites in addition to the established IQ-like motif in MHR1/2.....	56
4.2.2	Novel Calmodulin binding motif in NUDT9H contributes to temperature sensitivity of TRPM2.....	63
4.2.2.1	BEST-TROSY NMR spectra confirm interaction of VL24 and Ca ²⁺ - Calmodulin.....	63
4.2.2.2	The partially unfolded NUDT9H domain binds Ca ²⁺ -Calmodulin.....	64
4.2.2.3	Calmodulin binding to the NUDT9H domain affects the temperature- dependent activation of the TRPM2 channel	70
4.3	Discussion	72
4.3.1	High affinity binding of the known IQ-like binding site to Calmodulin.....	72

TABLE OF CONTENTS

4.3.2	A novel Calmodulin binding site in the TRP domain of TRPM2 might be involved in Ca ²⁺ -dependent channel regulation	74
4.3.3	Novel Calmodulin-binding motif in its NUDT9H domain contributes to temperature sensitivity of TRPM2.....	75
5	Perspective	78
6	Material and Methods.....	79
6.1	Material.....	79
6.1.1	Chemicals.....	79
6.1.2	Buffers and solutions	84
6.1.3	Culture media.....	85
6.1.4	Plasmid Vectors	86
6.1.5	Primers	87
6.2	Methods	90
6.2.1	Maintenance and growth of bacteria.....	90
6.2.2	Preparation and transformation of chemically competent <i>E.coli</i> cells.....	90
6.2.3	Preparation and transformation of electrocompetent <i>E.coli</i> cells.....	91
6.2.4	Molecular Biology	91
6.2.4.1	Amplification PCR	91
6.2.4.2	<i>QuikChange</i> site-directed mutagenesis PCR.....	92
6.2.4.3	Restriction enzyme digest.....	92
6.2.4.4	DNA fragment ligation	92
6.2.4.5	Agarose gel electrophoresis	93
6.2.5	Protein Expression and purification	93
6.2.5.1	NUDT9 wt, genetically encoded FRET sensors, and NUDT9 for Alexa Fluor dye labeling.....	94
6.2.5.2	NUDT9trC, NUDT9trC RIL, ¹⁵ N- or ² H, ¹³ C, ¹⁵ N-NUDT9trC RIL.....	94
6.2.5.3	NUDT9H	94
6.2.5.4	Calmodulin.....	95
6.2.6	Sodium-dodecyl sulfate-polyacrylamide gel electrophoresis (SDS PAGE)	95

TABLE OF CONTENTS

6.2.7	Isothermal titration calorimetry (ITC)	96
6.2.8	ADPR and 2'-deoxy-ADPR hydrolysis analyzed by HPLC	96
6.2.9	Differential scanning fluorimetry (nDSF)	97
6.2.10	Circular dichroism (CD) spectroscopy	98
6.2.11	Förster or fluorescence resonance energy transfer (FRET)	98
6.2.11.1	Genetically encoded FRET sensors	100
6.2.11.2	Alexa Fluor dye labeling	100
6.2.11.3	Fluorescence spectrometry of FRET sensors	101
6.2.12	Fluorescence measurement of VL24 peptide and Ca ²⁺ -Calmodulin	102
6.2.13	Protein crystallization and crystal structure determination	102
6.2.14	Small-angle X-ray scattering (SAXS)	102
6.2.15	Nuclear magnetic resonance (NMR) spectroscopy	104
6.2.15.1	Expression of uniformly labeled protein	104
6.2.15.2	NMR data acquisition	105
6.2.16	HEK293 cell culture and transfection	106
6.2.17	Surface expression assay	107
6.2.18	Electrophysiology and patch clamp technique	108
6.2.18.1	TRPM2 recordings	110
7	References	112
8	Safety and Disposal	126
8.1	GHS hazards statements	126
8.2	GHS precautional statements	127
8.3	Disposal	128
9	Appendix	128
9.1	NMR backbone resonance assignment of NUDT9trC _{W339} RIL/ADPR	128
	Acknowledgement	135
	Eidesstattliche Versicherung	136

Abstract

ADPR is an important nucleotide that is used as a cleavage product of nicotinamide adenine dinucleotide for the post-translational modification of the mono- and poly-ADP-ribosylation of biomolecules and acts as a secondary messenger itself. Accordingly, ADPR is involved in many cellular processes. Precise control of ADPR levels is important to maintain cell homeostasis, especially since accumulation of ADPR is potentially toxic. The pyrophosphatase NUDT9 exhibits high ADPR specificity and hydrolyzes the nucleotide to AMP and ribose 5-phosphate in the presence of Mg^{2+} and thereby controls cellular ADPR levels. NUDT9 is widely expressed among various cell types and localized in mitochondria and the cytosol. 2'-deoxy-ADPR was identified as a novel NUDT9 substrate and the binding kinetics as well as the binding affinities for ADPR and 2'-deoxy-ADPR were determined to be comparable. Both nucleotides bind to an identical binding site as shown by TROSY-NMR experiments. Backbone resonance assignment identified residues so far unknown to be involved in the ligand binding. Interestingly, ligand binding not only thermally stabilized NUDT9 but also induced a more compact conformation of the complex. Based on these results, a prototype of a NUDT9 FRET sensor chemically labelled with Alexa Fluor was developed, which will visualize ADPR signaling pathways in cells in the future.

The TRPM2 channel is a non-selective cation channel in the plasma membrane permeable for Ca^{2+} , Na^{+} and K^{+} ions. The C-terminal domain is homologous to NUDT9 and the channel is activated by cooperative binding of ADPR and Ca^{2+} . Further, TRPM2 is regulated by Calmodulin and temperature. In addition to the established Calmodulin binding site in the N-terminus of TRPM2, two novel potential Calmodulin binding sites were identified. The first one is located C-terminal but in vicinity to the transmembrane section of the channel. Apo and Ca^{2+} -Calmodulin bound to respective peptides but the exact binding mode could not be determined as it contained both endothermic and exothermic parts. The second novel Calmodulin binding site is located in the NUDT9H domain. The formation of a complex with Ca^{2+} -Calmodulin thermally stabilized the isolated NUDT9H domain. Alanine substitution of the anchor residues Trp1355 and

Ile1368 in the binding site abolished Calmodulin-dependent temperature sensitivity of TRPM2.

Zusammenfassung

ADPR ist ein wichtiges Nukleotid, das als Spaltprodukt von Nikotinamidadenindinukleotid zur posttranslationalen Modifikation der Mono- und Poly-ADP-Ribosylierung von Biomolekülen verwendet wird sowie selbst als sekundärer Botenstoff fungiert. Folglich ist ADPR an vielen zellulären Vorgängen beteiligt. Eine genaue Kontrolle der ADPR-Spiegel ist essentiell, um die Zellhomöostase aufrechtzuerhalten, insbesondere da ADPR potenziell toxisch ist.

Die Pyrophosphatase NUDT9 weist eine hohe Spezifität für ADPR auf und hydrolysiert das Nukleotid in Anwesenheit von Mg^{2+} zu AMP und Ribose-5-phosphat und reguliert dadurch den zellulären ADPR-Spiegel. NUDT9 wird in verschiedenen Zelltypen exprimiert und ist in Mitochondrien und im Cytosol lokalisiert. 2'-desoxy-ADPR wurde als neues NUDT9-Substrat identifiziert und die Bindungskinetik sowie die Bindungsaffinitäten für ADPR und 2'-desoxy-ADPR wurden als vergleichbar bestimmt. Durch TROSY-NMR-Experimente wurde gezeigt, dass beide Nukleotide im gleichen aktiven Zentrum in NUDT9 binden. Mit Hilfe der Zuordnung von NMR-Resonanzen des Proteinerückgrats wurde Aminosäure-Seitenketten identifiziert, von denen bisher unbekannt war, dass sie an der Ligandenbindung beteiligt sind. Interessanterweise stabilisierte die Ligandenbindung NUDT9 nicht nur thermisch, sondern induzierte auch eine kompaktere Konformation des Komplexes. Basierend auf diesen Ergebnissen wurde ein Prototyp eines mit Alexa Fluor chemisch markierten NUDT9-FRET-Sensors entwickelt, der in Zukunft die Visualisierung von ADPR-Signalwegen in Zellen ermöglichen kann.

TRPM2 ist ein nicht selektiver Kationenkanal in der Plasmamembran, der für Ca^{2+} -, Na^{+} - und K^{+} -Ionen durchlässig ist. Seine C-terminale Domäne ist homolog zu NUDT9 und der Kanal wird durch kooperative Bindung von ADPR und Ca^{2+} aktiviert. Zudem wird TRPM2 durch Calmodulin und Temperatur reguliert. Zusätzlich zu der etablierten Calmodulin-Bindungsstelle im N-Terminus von TRPM2 wurden zwei neue potenzielle Calmodulin-Bindungsstellen identifiziert.

Die erste befindet sich auf der C-terminalen Seite der Transmembranregion. Sowohl apo- als auch Ca^{2+} -Calmodulin band an entsprechende synthetische Peptide, aber der

Bindungsverlauf mit exo- als auch endothermen Merkmalen war untypisch und konnte nicht weiter aufgeklärt werden. Die zweite neue Calmodulin-Bindungsstelle befindet sich in der NUDT9H-Domäne. Die Komplexbildung mit Ca^{2+} -Calmodulin stabilisierte die isolierte NUDT9H-Domäne thermisch. Alaninsubstitution der Ankerreste Trp1355 und Ile1368 verhinderte eine Calmodulin-abhängige Sensitivierung von TRPM2 bei erhöhter Temperatur.

Publications associated with this thesis

Gattkowsky E, Johnsen A, Bauche A, Möckl F, Kulow F, Garcia Alai M, Rutherford TJ, Fliegert R and Tidow H, *Novel CaM-binding motif in its NudT9H domain contributes to temperature sensitivity of TRPM2*. Biochim Biophys Acta Mol Cell Res. 2019; 1866(7):1162-1170.

Gattkowsky E, Rutherford TJ, Möckl F, Bauche A, Sander S, Fliegert R and Tidow H, *Analysis of ligand-binding and resulting conformational changes in pyrophosphates NUDT9*, in revision

Niebling S, Burastero O, Bürgi J, Günther C, Defelipe L, Sander S, Gattkowsky E, Anjanappa R, Wilmanns M, Springer S, Tidow H and García-Alai M, *FoldAffinity: Binding affinities from nDSF experiments*, Scientific reports 11, 9572 (2021), DOI: 10.1038/s41598-021-88985-z

List of Figures

Figure 1.1: ADPR results from the hydrolysis of NAD ⁺ , cyclic-ADPR and (poly-)ADP-ribosylated proteins.	1
Figure 1.2: Generation and function of ADPR in mitochondria.....	2
Figure 1.3: Crystal structures of human NUDT enzymes with ADPR specificity show structural diversity.	5
Figure 1.4: Cartoon representation of the TRPM2 channel (pdb: 6PUS).....	8
Figure 1.5: Interaction of the MHR1/2 and NUDT9H domain in the closed and open conformation of <i>dr</i> TRPM2 and <i>hs</i> TRPM2.	11
Figure 1.6: ADPR and derivatives acting as agonists on TRPM2.	13
Figure 3.1: Purification of NUDT9 wt.	17
Figure 3.2: NUDT9 wt hydrolyzes ADPR and 2'-deoxy-ADPR to AMP or 2'-deoxy-AMP and ribose 5-phosphate.....	18
Figure 3.3: Binding affinities for ADPR and 2'-deoxy-ADPR to NUDT9 determined by ITC.	19
Figure 3.4: The breakdown products of ADPR, ribose 5-phosphate and AMP do not bind to wild type NUDT9 as measured by ITC.	20
Figure 3.5: NUDT9 wt does not hydrolyze ADPR using Ca ²⁺ as co-factor.	21
Figure 3.6: CD spectra of NUDT9 wt with or without ligand bound.	22
Figure 3.7: NUDT9 wt is thermally stabilized by binding of ADPR or 2'-deoxy-ADPR. ...	22
Figure 3.8: NUDT9 wt bound to ADPR is more compact than the apo NUDT9 wt as revealed by SAXS.	23
Figure 3.9: Scattering plots of apo NUDT9 wt and NUDT9 wt in complex with ADPR compared to calculated scattering curves derived from the crystal structures of NUDT9 (1q33 and 1qvj).....	24
Figure 3.10: NUDT9trC is thermally stabilized by binding of ADPR or 2'-deoxy-ADPR. 26	
Figure 3.11: NUDT9trC in complex with ADPR or 2'-deoxy-ADPR is more compact than the apo NUDT9trC as revealed by SAXS.....	27
Figure 3.12: Crystallization trials of NUDT9trC in complex with ADPR.....	27

Figure 3.13: Binding affinities for ADPR and 2'-deoxy-ADPR to NUDT9trC RIL as determined by ITC.	28
Figure 3.14: NUDT9trC RIL shows no significant pyrophosphatase activity against ADPR or 2'-deoxy-ADPR.	29
Figure 3.15: NUDT9trC RIL is thermally stabilized by binding of ADPR or 2'-deoxy-ADPR.	30
Figure 3.16: NUDT9trC RIL bound to ADPR or 2'-deoxy-ADPR is more compact than the apo NUDT9trC RIL revealed by SAXS.	31
Figure 3.17: ^1H - ^{15}N -TROSY NMR spectra for apo NUDT9trC RIL and in complex with ADPR or 2'-deoxy-ADPR indicate large conformational changes for the complex but only minor differences for the ligands.	32
Figure 3.18: Backbone resonance assignment of ADPR bound NUDT9trC RIL covers 85 % of the signals.	33
Figure 3.19: Ligand binding pocket of NUDT9 with residues interacting with the ligands identified by crystallography and NMR.	34
Figure 3.20: Illustration of potential NUDT9 based FRET sensors for ADPR.	35
Figure 3.21: Purification of mTFP1-full length NUDT9 RIL-mVenus FRET sensor from <i>E.coli</i>	36
Figure 3.22: Fluorescent measurements of mTFP1-mVenus FRET proteins show FRET. ...	37
Figure 3.23: ITC measurements of mTFP1-mVenus fusion proteins of NUDT9trC _{W339} and NUDT9trC _{D336} (EAAAK) ₅ confirm a nanomolar binding affinity.	38
Figure 3.24: Genetically encoded mTFP1-mVenus NUDT9 FRET fusion proteins undergo subtle conformational changes upon ADPR binding.	39
Figure 3.25: Conjugation reaction of a cysteine residue in NUDT9 to Alexa Fluor Maleimide gives an Alexa Fluor coupled NUDT9 FRET probe.	42
Figure 3.26: Cys207 in NUDT9 does not affect the binding affinity of ADPR.	43
Figure 3.27: Purification and comparison of unlabelled and Alexa Fluor labelled NUDT9trC RIL.	44
Figure 3.28: Normalized fluorescence spectra for all Alexa Fluor labelled NUDT9trC variations.	46

Figure 3.29: Multiple sequence alignment of *hsNUDT9*, the NUDT9H domain of *hsTRPM2* and *nvTRPM2* shows high sequence similarities but also important differences in the NUDIX box. 50

Figure 3.30: The terminal tail occupies the binding pocket of the symmetry mate in the crystal structure of NUDT9 (pdb: 1Q33)..... 52

Figure 4.1: Identification of potential Calmodulin binding sites in TRPM2. 57

Figure 4.2: The RK26 peptide binds Ca²⁺-Calmodulin with nanomolar affinity but not apo Calmodulin..... 58

Figure 4.3: The LK24 peptide and the longer LK29 bind apo Calmodulin but the shorter LK18 does not. 59

Figure 4.4: LK18 binds Ca²⁺-Calmodulin and shows a biphasic binding pattern. 60

Figure 4.5: Binding of LK24 and LK29 to Ca²⁺-Calmodulin indicates several binding events as measured by ITC. 61

Figure 4.6: The VL24 peptide binds Ca²⁺-Calmodulin with nanomolar affinity but it does not bind apo Calmodulin..... 62

Figure 4.7: Purification of peptide Ca²⁺-Calmodulin complex by size exclusion chromatography. 63

Figure 4.8: BEST-TROSY NMR spectra of apo Ca²⁺-Calmodulin and in complex with the VL24 peptide. 64

Figure 4.9: Purification of the NUDT9H domain of TRPM2. 65

Figure 4.10: CD spectra of the isolated NUDT9H domain indicated correct protein folding. 65

Figure 4.11: Size exclusion chromatography of the Ca²⁺-Calmodulin/NUDT9H complex. 66

Figure 4.12: Ca²⁺-Calmodulin binds partially unfolded NUDT9H as shown by nDSF..... 67

Figure 4.13: The tryptophan residue in the VL24 peptide is shielded in the complex with Ca²⁺-Calmodulin. 68

Figure 4.14: Ca²⁺-Calmodulin stabilizes NUDT9H at elevated temperatures..... 69

Figure 4.15: Ca²⁺-Calmodulin binds NUDT9H at 35 °C with nanomolar affinity as determined by ITC. 69

Figure 4.16: Comparison of the surface expression of TRPM2 wild type and the W1355A/I1368A mutant. 70

Figure 4.17: Calmodulin binding to the NUDT9H domain in TRPM2 influences its temperature-dependent activation by ADPR and 2'-deoxy-ADPR. 71

Figure 4.18: Localization of the IQ-like motif in TRPM2..... 73

Figure 4.19: Calmodulin binding site in NUDT9H interacts with the EF-loop of the neighboring MHR1/2 in the closed TRPM2 conformation. 76

Figure 6.1: Basic principles for Förster resonance energy transfer (FRET). 99

Figure 6.2: SAXS data analysis. 104

Figure 6.3: Electronic model of the plasma membrane of an intact cell..... 109

List of Tables

Table 3-1: Kinetic parameters for the hydrolysis of ADPR and 2'-deoxy-ADPR by NUDT9 determined by HPLC analysis. 18

Table 3-2: Thermodynamic parameters for binding of ADPR and 2'-deoxy-ADPR to wild type NUDT9 with Ca²⁺ as cofactor determined by ITC. 20

Table 3-3: Thermodynamic parameters for the binding of ADPR and 2'-deoxy-ADPR to NUDT9trC RIL using Mg²⁺ as co-factor as determined by ITC. 29

Table 3-4: Summary of calculated acceptor to donor ratios for apo FRET proteins, the ADPR-bound form and the relative change of the ratios. 37

Table 3-5: Summary of calculated acceptor to donor ratios for apo FRET proteins, the ADPR bound form and the relative change of the ratios for several cp variants of the mTFP1 and mVenus FRET pair. 40

Table 3-6: Summary of calculated acceptor to donor ratios for apo FRET proteins, the ADPR bound form and the relative change of the ratios for several cp variants of the CFP-YFP FRET pair..... 41

Table 3-7: Proposed distances between mutated cysteine pairs chosen for Alexa Fluor labelling in NUDT9trC. 43

Table 3-8: Spectral properties of the used Alexa Fluor dye combinations..... 45

Table 3-9: Summary of FRET results for Alexa Fluor labelled NUDT9trC. 47

LIST OF TABLES

Table 4-1: List of peptides of Calmodulin binding motifs in TRPM2 used for binding assays.	58
Table 6-1: Chemicals.....	79
Table 6-2: Composition of buffers and solutions.....	85
Table 6-3: Composition of Culture Media.....	86
Table 6-4: Plasmid Vectors.	86
Table 6-5: Primers.	87
Table 6-6: Parameters for the individual FRET pairs used for fluorescence measurements.	101
Table 9-1: Assigned NMR backbone resonances of the NUDT9trC _{W339} -RIL/ADPR complex.	128

List of Abbreviations

α	alpha
Å	Angstrom
A	Ampere
ADP	Adenosine-5'-diphosphate
ADPR	Adenosine-5'-diphosphoribose
ALA	Alanine
AMP	Adenosine-5'-monophosphate
Amp	Ampicillin
ARG	Arginine
ARH	ADP-ribosylhydrolase
ART	ADP-ribosyltransferase
ASN	Asparagine
ASP	Aspartic acid/Aspartate
β	Beta
BSA	Bovine serum albumin
C	Celsius
Ca ²⁺	Calcium ions
cADPR	Cyclic-ADP-ribose
CaM	Calmodulin
CD	Circular dichroism
CD	Cluster of differentiation
C _m	Membrane capacitance
cv	Column volume
CYS	Cysteine
Da	Dalton
D _{max}	Maximum particle dimension
DMEM	Dulbecco's Modified Eagle Medium
DNA	Deoxyribonucleic acid
D-PBS	Dulbecco's phosphate-buffered saline
DSF	Differential scanning fluorimetry

LIST OF ABBREVIATIONS

DTT	1,4-Dithiothreitol
Δ	Delta
E	Potential/voltage
<i>E.coli</i>	<i>Escherichia coli</i>
eV	Electron volt
F	Farad
GHz	Gigahertz
g	Gram
GLN	Glutamine
GLU	Glutamic acid/Glutamate
GLY	Glycine
GST	Glutathione-S-transferase
h	Hour
HEK	Human embryonal kidney
HEPES	4-(2-Hydroxyethyl)piperazine-1-ethanesulfonic acid
HIS	Histidine
HPLC	high pressure/performance liquid chromatography
HRP	Horseradish peroxidase
I	Current or Intensity
IDPR	Inosine-diphosphate ribose
IMAC	Immobilized metal affinity chromatography
IPTG	Isopropyl - β -D-thiogalactopyranoside
ILE	Isoleucine
K	Kelvin
k	Kilo
kat	katal (mol s ⁻¹)
K _D	Dissociation constant
λ	Wavelength
L	Liter
LB	Lennox-Broth
LEU	Leucine
LYS	Lysine

LIST OF ABBREVIATIONS

MET	Methionine
min	Minute
Mg ²⁺	Magnesium ions
MHD	TRPM homology domain
MHz	Megahertz
mL	Milliliter
mol	Mole
M	Molar
MW	Molecular weight
MWCO	Molecular weight cut off
μ	Micro
NAADP	Nicotinic acid adenine dinucleotide phosphate
NAD	Nicotinamide adenine dinucleotide
NADase	NAD hydrolase
nDSF	Nano differential scanning fluorimetry
Ni-NTA	Nickel-Nitrilotriacetic acid
nm	Nanometer
ns	Nanosecond
NUDIX	nucleoside diphosphates linked to another moiety x
Ω	Ohm
OD	Optical density
PARG	Poly-ADPR glycohydrolase
PARP	Poly-ADPR polymerase
PDB	Protein Data Bank
PHE	Phenylalanine
PRO	Proline
PVDF	polyvinylidene difluoride
Q	charge
R	Resistance
R _g	Radius of gyration
rpm	Rounds per minute
s	Second

LIST OF ABBREVIATIONS

SAXS	Small-angle X-ray scattering
SEC	Size exclusion chromatography
SER	Serine
SDS PAGE	Sodium-dodecyl sulfate-polyacrylamide gel electrophoresis
T	Temperature
TEV	Tobacco etch virus
THR	Threonine
TM	Trans membrane
TRP	Tryptophan
TRPM2	Transient receptor potential Melastatin subfamily member 2
TYR	Tyrosine
UV	Ultraviolet
V	Volt
VAL	Valine
v/v	Volume per volume
wt	Wild type
W	Watt
w/v	Weight per volume

1 Introduction

An efficient and dynamic communication between cellular macromolecules is crucial to control fundamental biological processes. Protein function and rapid control of numerous cellular processes is regulated by post-translational modifications of proteins. These post-translational modifications allow for dynamic changes of the protein function by modifying its conformation, activity, stability, and interaction among proteins. Mono- and poly-ADP-ribosylation is a prominent posttranslational modification where a single or multiple units of adenosine-diphosphate ribose (ADPR) are transferred from NAD^+ to amino acid side chains of proteins, nucleic acids (1) or even small molecules (2). Further, free ADPR acts as signaling molecule itself (3, 4). The precise control of ADPR levels in cells is therefore crucial to maintain cellular homeostasis.

1.1 Adenosine-diphosphate ribose (ADPR)

ADPR belongs to the class of purine nucleotide sugars and is composed of adenosine linked by a diphosphate bridge to a second ribose. ADPR is generated by multiple pathways carried out in mitochondria, the nucleus, and the cytosol. Most ADPR results from the hydrolysis of nicotinamide adenine dinucleotide (NAD^+), cyclic-ADPR and poly-ADP-ribosylated proteins (Figure 1.1).

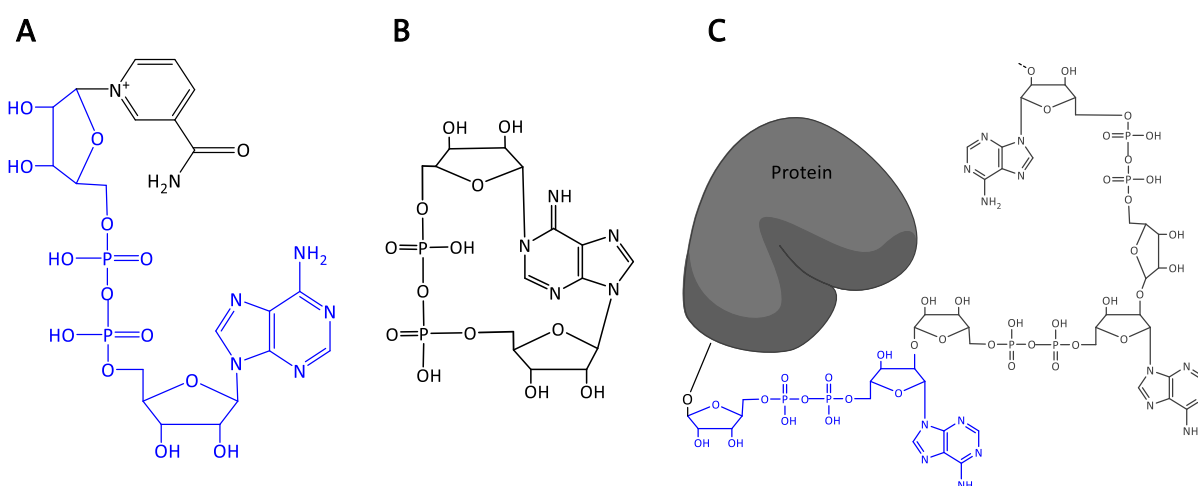


Figure 1.1: ADPR results from the hydrolysis of NAD^+ , cyclic-ADPR and (poly-)ADP-ribosylated proteins. Chemical structure of NAD^+ with highlighted ADPR moiety in blue. (B) A N^1 -glycosidic bond is formed between the terminal ribose and the adenine base in cyclic-ADPR. (C) Representation of a poly-ADP-ribosylated protein with one ADPR subunit highlighted in blue.

1.2 ADPR generation and function in mitochondria

Mitochondria represent one source for ADPR in the cell as they contain the major pool of cellular NAD^+ (5, 6), a key molecule in mitochondrial metabolism acting as redox coenzyme in metabolism as well as signaling molecule (Figure 1.2).

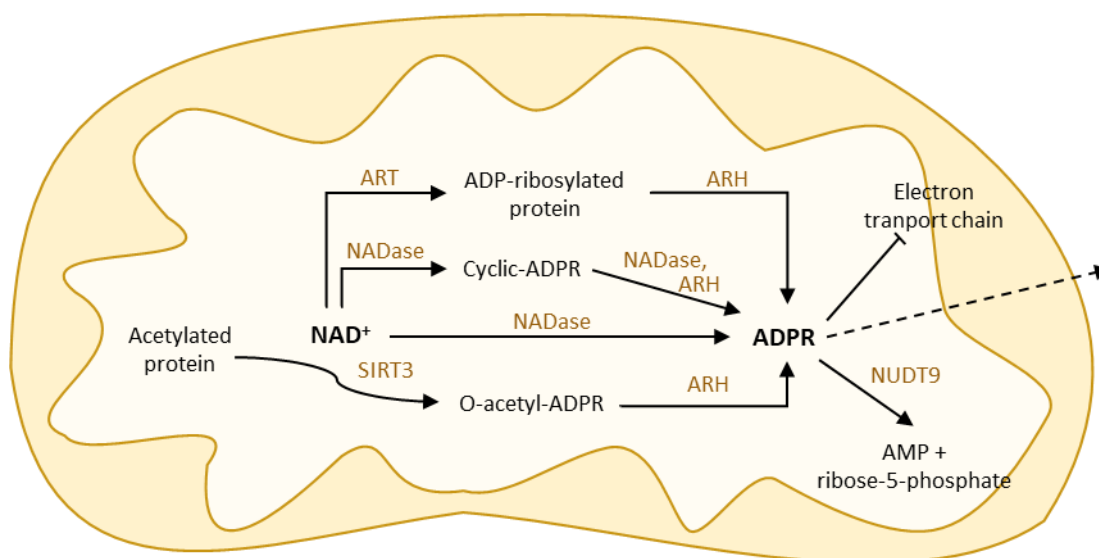


Figure 1.2: Generation and function of ADPR in mitochondria. NAD^+ is metabolized by various mitochondrial enzymes (brown) to regulate mitochondrial proteins or to generate the second messengers cyclic-ADPR and ADPR. Acetylated mitochondrial proteins were activated by sirtuin 3 (SIRT3), which transfers the acetyl moiety onto NAD^+ , releasing nicotinamide and generating O-acetyl-ADPR. Mitochondrial proteins are regulated by NAD -dependent ADP-ribosylation by ADP-ribosyltransferases (ARTs). NAD^+ is cyclized to cyclic-ADPR or hydrolyzed to ADPR by an unidentified NADase. ADP-ribosylhydrolase 3 (ARH3) generates ADPR from ADP-ribosylated proteins, cyclic-ADPR or O-Acetyl-ADPR. ADPR inhibits the complex I of the electron transport chain, is hydrolyzed by NUDT9 or released into the cytosol.

Acetylation regulates all major mitochondrial processes, mitochondrial enzymes are inhibited by N- ϵ -lysine acetylation and their activity is restored by deacetylation (7). Deacetylases of the silent information regulator like protein (sirtuin, SIRT) family carry out the NAD -dependent deacetylation. From the three mitochondrial sirtuins SIRT3-5 (8), SIRT3 is the major regulator with a broad target spectrum (9). Following cleavage and release of nicotinamide from NAD^+ , the acetyl moiety from lysine is transferred onto the 2''-position of ADPR generating 2''-O-acetyl-ADPR (10, 11).

ADP-ribosylation describes the transfer of an ADPR molecule from NAD^+ to a target protein carried out by ADP-ribosyltransferases (ARTs) (12, 13). Several mitochondrial enzymes are regulated by mono-ADP-ribosylation, e.g. the glutamate-dehydrogenase is

inhibited by mono-ADP-ribosylation by SIRT4 (13, 14) and non-enzymatic mono-ADP-ribosylation of mitochondrial proteins trigger Ca^{2+} release from mitochondria (15).

Besides ADPR, the Ca^{2+} -releasing second messengers nicotinic acid adenine dinucleotide phosphate (NAADP) (16) and cyclic-ADPR (17) are generated from NAD^+ by NADases. Although the mitochondrial NADase has not been identified yet, NADase (or more precise ADP-ribosylcyclase) activity has been repeatedly demonstrated for mitochondria (18–20). The direct conversion of NAD^+ to ADPR, as well as the cleavage of cyclic-ADPR to ADPR is also assigned to this enzyme.

O-acetyl-ADPR, ADP-ribosylated proteins and cyclic-ADPR are cleaved by the ADP-ribosylhydrolase 3 (ARH3) and liberate ADPR (21–23). Free ADPR inhibits the complex I of the electron transport chain and therefore directly affects mitochondria (24). Thus, appropriate ADPR clearance is essential to maintain mitochondrial function. ADPR is hydrolyzed to AMP and ribose 5-phosphate by NUDIX enzymes (25, 26) or can be released from mitochondria (4) via the mitochondrial permeable transition pore (27) or an unidentified ADPR transporter.

1.3 ADPR generation in the nucleus

ADPR generation in the nucleus involves consecutive enzymatic reactions catalyzed by poly-ADPR polymerase (PARP) and poly-ADPR glycohydrolase (PARG).

The 18 members of the PARP family are involved in cell proliferation, cell death (28), nucleic acid metabolism, chromatin remodeling and DNA synthesis (29). PARP1 is the most prominent member of the PARP family. Upon oxidative stress and resulting DNA damage, PARP1 is activated (30, 31). PARP1 generates and attaches poly-ADPR chains on proteins and thereby initiates DNA repair (28, 29), which is necessary for normal cell cycle progression (32) since genomically instable cells accumulate in cell cycle arrest. PARP transfers ADPR to aspartic acid or glutamic acid side chains of proteins forming ester bonds or to serine side chains forming an O-glycosidic bond (33, 34). Poly-ADP-ribosylated proteins can contain up to 200 single ADPR units linked by O-glycosidic ribose-ribose bonds.

PARG efficiently hydrolyses the specific O-glycosidic ribose–ribose bonds of poly-ADP-ribosylated proteins to generate free ADPR (35–37). Different splice variants of PARG are

targeted to the nucleus or the cytosol and ensure the turnover of poly-ADPR-ribosylated proteins (38, 39).

1.4 ADPR generation in the cytosol

Cluster of differentiation lymphocyte antigen CD38 and to a lesser extent the paralog CD157 (also named BST-1 for bone marrow stroma cell antigen 1, (40)) catalyze the formation of cyclic-ADPR from NAD⁺ and hydrolyze cyclic-ADPR to generate ADPR (41–43). CD38 thus harbors competitive NADase and cyclase activity. CD38 is regulated by ADPR-product inhibition and ATP inhibits the cyclic-ADPR activity (42, 44). CD38 is a glycoprotein expressed on the cell surface with a single transmembrane helix. Since it is mainly expressed as a type II configuration in the plasma membrane with an extracellular catalytic C-terminus (45), it has long been discussed how conversion and transport of the cytosolic educts and products can occur. It has been shown that the extracellular NAD⁺ precursor nicotinamide mononucleotide (NMN) is generated from nicotinamide riboside by CD38 and transported into the cell for NAD⁺ biosynthesis (46). Further, the discovery that CD38 occurs not only in type II but also in type III configuration enables cytosolic NAD⁺ conversion and suggests a regulatory function of signaling activity through interconversion of the two configurations (47).

Control of free ADPR ribose levels in the cytosol is essential for cell homeostasis since it inhibits for example the glyceraldehyde-3-phosphate dehydrogenase (GAPDH) (48, 49), one of the key enzymes in glycolysis.

1.5 ADPR degradation by NUDIX enzymes

Proteins of the NUDIX superfamily have been found in all branches of the phylogenetic tree (50) and consist mainly of pyrophosphohydrolases. The name of the protein family was initially MuT family based on its founding member *Escherichia coli* protein MutT (50), but was then changed to NUDIX proteins to reflect the general structure of substrates, which are nucleoside diphosphate linked to another moiety X (50–52). The general NUDIX motif with the consensus 23 amino acid sequence G_xEx₅[UA]_xREx₂EExGU (where X represents any amino acid and U represents an aliphatic hydrophobic amino acid) is responsible for catalysis (50, 52). The highly conserved glutamate residues in the central

RE₂EE motif are essential for coordination of divalent cations that facilitate catalysis (53). The NUDIX fold spans about 130 amino acids and forms a helix-loop-helix structure (52, 54). Apart from the similarities in the NUDIX hydrolase domain itself, the positioning of this domain within the individual proteins is very different (55).

Based on their broad substrate spectrum, NUDIX hydrolases are involved in various cellular processes including cellular metabolism, homeostasis, and mRNA processing (51, 52). They are considered as metabolic detoxifiers since they hydrolyze and thereby remove potentially harmful molecules like ADPR. The human genome encodes 24 NUDIX hydrolase genes of which NUDT5, NUDT9, NUDT12 and NUDT14 (listed in order of decreasing ADPR pyrophosphatase activity) show ADPR specificity (55). Apart from that, their substrate specificity varies distinctively as substrate binding is not only directed by the NUDIX fold domain but also by residues outside the motif (55–57).

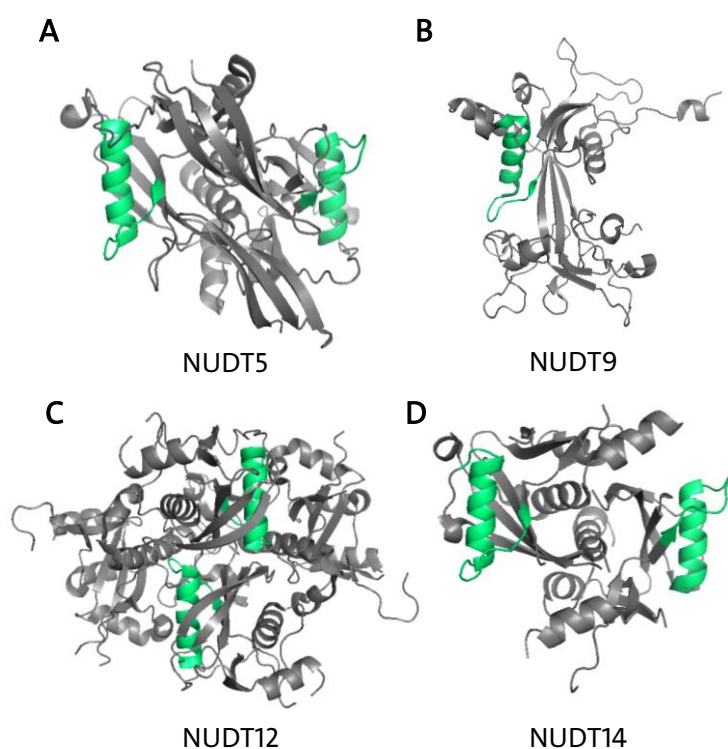


Figure 1.3: Crystal structures of human NUDT enzymes with ADPR specificity show structural diversity. The characteristic NUDIX fold is highlighted (green). (A) Crystal structure of the homodimer NUDT5 (pdb: 2DSC). (B) Crystal structure of NUDT9 (pdb: 1QVJ). (C) Crystal structure of NUDT12 (pdb: 6SCX). (D) Crystal structure of NUDT14 (pdb: 3Q91).

NUDT5 exhibits the highest ADPR pyrophosphatase activity among the four NUDIX enzymes, but also hydrolyzes other ADP-sugars like ADP-mannose and ADP-glucose (55). The enzyme is widely expressed in a variety of cell types (58, 59) and has been shown to be involved in nuclear ATP generation (60). NUDT5 and NUDT14 exhibit homodimerization and are structurally related (61, 62). Both share activity towards ADPR and ADP-glucose (55). NUDT12 shows peroxisomal localization and besides ADPR also hydrolyzes NAD⁺ as well as the derivatives NADH and NADPH (63).

NUDT5, NUDT9 and NUDT14 are highly expressed in cancer tissues and are involved in cancer progression (55, 60, 64–66). Based on the involvement of their substrates in major cell pathways, the upregulation of these NUDIX enzymes in cancer cells was suggested to shift cancer cell metabolism to promote cell survival under hypoxic conditions (65).

1.5.1 NUDT9

Structural and sequence analysis identified NUDT9 as an evolutionary ancestor of all human NUDT enzymes (55). It is the only NUDT enzyme active as monomer (26, 57) and shows the highest substrate specificity (55). NUDT9 exhibits high substrate specificity towards ADPR, but high concentrations of 2'-phospho ADPR (67), O-acetyl-ADPR (68) and inosine-diphosphate ribose (IDPR) (26, 69) were also hydrolyzed with reduced activity. An intact NUDIX motif and Mg²⁺ ions were required for pyrophosphatase activity (70). Using Mn²⁺ ions, NUDT9 exhibits a reduced activity towards ADPR, no activity was detected using Zn²⁺, Cu²⁺ or Co²⁺ as co-factor (70, 71). Interestingly, NUDT9 changes its preference for the activating divalent cation from Mg²⁺ to Mn²⁺ under oxidizing conditions; the effect was reversed by DTT treatment (71). NUDT9 exhibits optimal activity at neutral pH (70).

NUDT9 is mainly expressed in heart, skeletal muscle, liver, kidney and pancreas (26). Two splice variants exist: NUDT9 α shows clear mitochondrial localization due to an additional N-terminal mitochondrial leader sequence, NUDT9 β shows no clear cellular localization and is evenly distributed in the cytosol (26, 70). NUDT9 α encodes a 350 amino acid protein with a predicted molecular mass of 39.1 kDa and represents the predominant form (26). NUDT9 β encodes a 300 amino acid protein with a predicted molecular mass of 33.8 kDa and represents an alternative splice form (26).

The NUDT9 crystal structure revealed a two domain structure with the catalytic center in the protein core (57). The C-terminal core domain hosts the substrate binding pocket including the characteristic NUDIX fold and preserves full specific ADPR pyrophosphatase activity after proteolysis (57, 70). The N-terminal cap domain is proteolytically labile and enhances the substrate affinity of the core domain (57, 70). The crystal structure of apo NUDT9 and NUDT9 in complex with the break-down product ribose 5-phosphate and Mg^{2+} were determined (57), but a crystal structure in complex with ADPR is still missing. Apart from the characteristic NUDIX fold, NUDT9 reveals no structure-based homology to other NUDIX enzymes (55).

1.6 The TRPM2 channel is gated by ADPR

The transient receptor potential melastatin type 2 (TRPM2) was cloned at the end of the past millennium and suggested to be a Ca^{2+} channel (72) based on its homology to lately discovered human TRP channels (73, 74). In 2001, ADPR-dependent activation of TRPM2 was discovered and TRPM2 was further characterized as non-selective cation channel permeable for Na^+ and Ca^{2+} ions (3, 75). By this, a signaling function was assigned to ADPR leading to its classification as a second messenger.

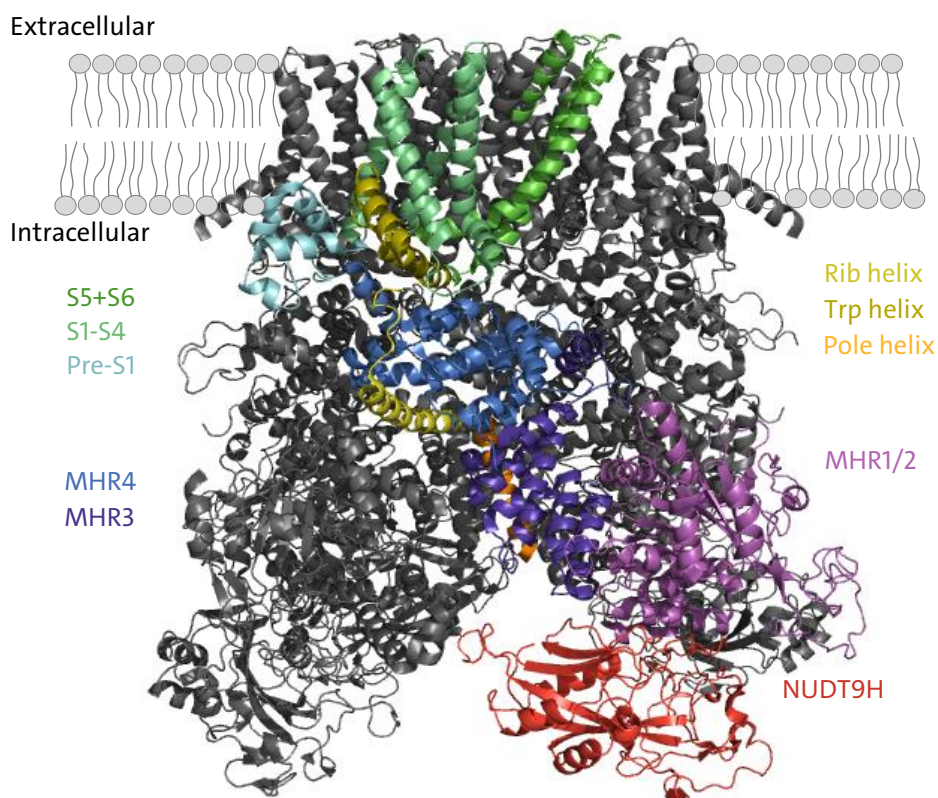


Figure 1.4: Cartoon representation of the TRPM2 channel (pdb: 6PUS). Individual domains of one subunit of the homotetrameric channel are colored.

The functional channel is assembled by four subunits surrounding a central ion-permeating pore. Each subunit contains six transmembrane helices and two large cytosolic domains: The N-terminal melastatin homology domain (MHR) conserved among the TRPM family members (76, 77) and a unique C-terminal domain homologous to ADPR pyrophosphatase NUDT9 (3). TRPM2 gating induced by ADPR-binding to the so-called NUDT9-homology (NUDT9H) domain and subsequent conformational channel rearrangements was assumed (3, 75). NUDT9H is indispensable for channel gating as demonstrated by a NUDT9H-deletion TRPM2 variant (78) and impaired ADPR-binding due to mutational analyses of the NUDIX box (4, 79).

NUDT9 and *human (hs)* NUDT9H comprise about 50 % sequence homology (3), the characteristic NUDIX fold is conserved but the NUDIX box reveals several sequence discrepancies causing an impaired pyrophosphatase activity of *hs*NUDT9H. Restoration of the canonical sequence prevents channel gating due to ADPR hydrolysis (4, 78) but the

non-hydrolyzable ADPR derivative α - β -methylene ADPR (AMPCPR) still activated TRPM2 (80).

A physiological pathway for ADPR-dependent TRPM2 activation was revealed when its role in the process of oxidative stress-mediated apoptosis was demonstrated. Characteristic ADPR-dependent channel activation due to extracellular application of hydrogen peroxide onto *hs*TRPM2-expressing cells (3, 81, 82) could be explained by increased activity of ADPR producing enzymes PARP and PARG in response to oxidative stress (1, 83). Since no channel activation was observed in inside-out patch clamp studies, a direct effect of hydrogen peroxide on TRPM2 appears to be unlikely (84).

A second novel ADPR binding site was recently discovered in the cleft of the N-terminal MHR1/2 domain of TRPM2 orthologues from human (85) and zebrafish *danio rerio* (*dr*) (86, 87) using cryo-electron microscopy (cryo-EM). Previous studies of the evolutionary TRPM2 ancestor from the sea anemone *nematostella vectensis* (*nv*) already implicated an additional ADPR binding site as this channel is activated by ADPR independently of its NUDT9H domain (88). However, the resolution of the N-terminal domain in the cryo-EM structure of this orthologue was insufficient to reveal the additional ADPR binding site (89).

The proposed amino acids involved in N-terminal ADPR binding are highly conserved in orthologues from the TRPM2 family (85), while the N-terminal region composed of MHR1-4 is a general characteristic of the TRPM family (76, 77). TRPM2 and TRPM8 are the closest relatives in the TRPM family in terms of structure but they differ in their mode of activation; TRPM8 is voltage-dependently gated and activated by cold and the cooling agent menthol (90). The amino acid sequence containing the N-terminal ADPR binding site in TRPM2 is fairly conserved in TRPM8 (89) but even a channel chimera with a C-terminal NUDT9H domain was insensitive to ADPR (91). The interaction of both functional ADPR binding sites as well as the contribution of the differential phosphatidylinositol-4,5-bisphosphate dependent regulation of TRPM2 (89, 92) and TRPM8 (93, 94) was considered as an additional factor.

Apart from the *nv*TRPM2 structure, in which the NUDT9H domain is not resolved (89), all TRPM2 structures show extensive interactions between MHR1/2 and NUDT9H (85, 87,

95). Functional studies of TRPM2-NUDT9(H) chimeras have implied that the interaction between the NUDT9H core subdomain and the cytosolic N-terminus of the channel stabilizes an open conformation of TRPM2, emphasizing the importance of this secondary interface in channel opening (96). Ca^{2+} as well as ADPR binding induce individual conformational rearrangements of the two domains mediated by substantial interfacial interactions which differ among the orthologues. The degree of interaction of the ADPR-binding MHR1/2 and NUDT9H domains increased in the course of evolution, which was possibly accompanied by an adapted channel regulation. Due to the lack of interactions and the resulting flexibility of the NUDT9H domain, the domain could not be resolved in the cryo-EM structure of *nv*TRPM2 (89). In comparison, the NUDT9H domain is already better resolved in the *dr*TRPM2 structure (87) and shows the best resolution in the *hs*TRPM2 structure (85). This was explained by expanded interactions between the NUDT9H domain and the rest of the channel (85, 97). In the closed conformation of *dr*TRPM2, NUDT9H predominantly interacts with intra-subunit MHR1/2 but is located as a flexible domain at the bottom of the channel. In contrast, in the open conformation of *dr*TRPM2, the NUDT9H domain moves and interacts also with the MHR1/2 domain from the neighboring subunit (86). In closed *hs*TRPM2, NUDT9H forms intra- as well as inter-subunit interfaces with MHR1/2 (85, 95). Upon ADPR binding, the interactions between the subunits are rearranged by the rotation of NUDT9H and MHR1/2; the conformational changes are transferred to the entire protein and ultimately result in the opening of the pore (85, 95).

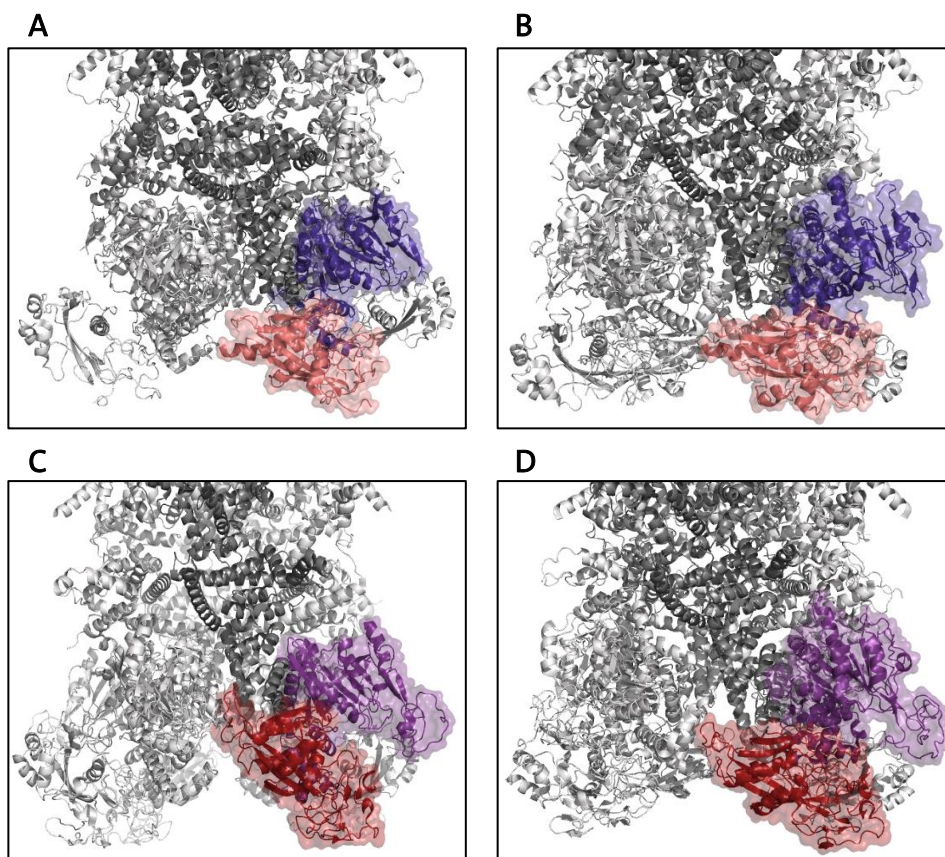


Figure 1.5: Interaction of the MHR1/2 and NUDT9H domain in the closed and open conformation of *drTRPM2* and *hsTRPM2*. Cytosolic part of the channels is shown. The NUDT9H domains from a single subunit are highlighted in salmon (*drTRPM2*) or firebrick (*hsTRPM2*) and the MHR1/2 domains from a single subunit are highlighted in violet blue (*drTRPM2*) or violet (*hsTRPM2*). (A+B) Interaction of MHR1/2 and NUDT9H in the (A) closed (pdb: 6DRK) and (B) open *drTRPM2* (pdb: 6drj) reveals increasing interactions of the NUDT9H domain with the rest of the channel in the ADPR and Ca^{2+} bound open conformation. (C+D) The NUDT9H domain in *hsTRPM2* shows extensive intra- as well as intersubunit interactions with MHR1/2 in the (C) closed (pdb: 6PUO) and (D) open (pdb: 6PUS) conformation when ADPR and Ca^{2+} are bound.

1.6.1 TRPM2 regulation by Ca^{2+}

ADPR-dependent TRPM2 activation essentially depends on Ca^{2+} (98). Without intracellular Ca^{2+} , TRPM2 cannot be activated by ADPR (99). Ca^{2+} stimulates ADPR-evoked currents of TRPM2 due to a positive feedback mechanism (99, 100), where Ca^{2+} enters the pore of already activated channels and saturates intracellular binding sites (89, 101); four Ca^{2+} ions cooperatively support TRPM2 activation (101). Extracellular Ca^{2+} is not sensed by the closed channel but Ca^{2+} ions entering the opened pore stabilize the open configuration and therefore affect the kinetics of channel gating (101). Accordingly,

the Ca²⁺ binding sites must be accessible from the cytosolic site and probably located close to the pore (101).

The cryo-EM structure of *hs*TRPM2 shows a Ca²⁺ ion coordinated by E843 and Q846 in helix S2 as well as N869 and D872 in helix S3 and E1073 presented by the TRP helix (85). These residues are conserved among the TRPM2 channels from different orthologues and the Ca²⁺-sensitive TRPM4, TRPM5 and TRPM8 (94, 102–104). Protein binding sites for Ca²⁺ are often formed by the so-called EF-hand motif that forms helix-loop-helix secondary structures with the EF-loop presenting the Ca²⁺ (105, 106). Two EF-loops were identified in the N-terminus of TRPM2, with D267 and D278 essentially contributing to the Ca²⁺ sensitivity of TRPM2 as well as the synergy of Ca²⁺ and ADPR-dependent TRPM2 activation (107). In addition to direct regulation by Ca²⁺, indirect regulation by Ca²⁺-Calmodulin is possible. An IQ-like Calmodulin binding site was identified in the N-terminus of TRPM2 and an additional Calmodulin binding site with lower affinity for Calmodulin in the C-terminus was suggested (108). Calmodulin binding to the N-terminus is required for TRPM2 activation (108).

Further, phosphatidylinositol bisphosphate (PI(4,5)P₂), a phosphoinositide from the inner membrane leaflet known to regulate TRP channels (109), regulates the apparent Ca²⁺ affinity of TRPM2 (92). It has been suggested that both Ca²⁺ and PI(4,5)P₂ stabilize the open channel configuration or alternatively that PI(4,5)P₂ directly participates in Ca²⁺-binding (92).

1.6.2 TRPM2 regulation by temperature

All living organisms have evolved adaptive behavioral responses to changes in ambient temperature. The so-called thermo-TRP channels constitute important temperature sensors (110). TRPM2 is one of them (111–113), the channel senses non-noxious heat (113), limits fever response and thereby prevents body overheating (112). Application of hydrogen peroxide lowers the temperature threshold for TRPM2 activation from ~41 °C to body temperature (84, 114) probably due to oxidation of Met215 (114). However, the underlying molecular mechanism of thermoregulation has not been identified.

concentrations via binding to the ligand binding site in the NUDT9H domain but not in the MHR1/2 domain (69). While ADPR as well as IDPR evoked currents and kinetics were comparable for *hs*TRPM2, they significantly differ for *nv*TRPM2 (69). Based on this, a NUDT9H domain dependent regulation of *nv*TRPM2 via IDPR was suggested (69).

The second messenger cyclic-ADPR mobilizes Ca^{2+} from intracellular stores (120) and also triggers Ca^{2+} entry (121) but the molecular target is still debated. Cyclic-ADPR activates TRPM2 at millimolar concentrations and evokes 95 % decreased currents compared to ADPR (122). Applied together with ADPR, cyclic-ADPR acts synergistically and lowers the concentration-dependent ADPR response by two orders of magnitude (122). In addition, TRPM2 activation by cyclic-ADPR but not by ADPR is inhibited by 8-bromo-cyclic-ADPR (122) suggesting different binding sites for the two agonists. Recent cryo-EM structures of *hs*TRPM2 in complex with ADPR showed different ligand conformations in the two binding sites: ADPR adopted a horseshoe conformation (similar to the cyclic-ADPR conformation) in the N-terminal binding sites but an elongated conformation in the C-terminal binding site (85). Another cryo-EM structure of *hs*TRPM2 in complex with 8-bromo-cyclic-ADPR localized the antagonist in the N-terminal binding site (85). However, due to the instable N1-glycosidic bond of cyclic-ADPR, commercial cyclic-ADPR contains about 20-25 % ADPR contamination (67, 100) leading to an controversy about cyclic-ADPR as a TRPM2 agonist (123). The controversy was fueled by a recent study from Yu *et al.*, in which they reported cyclic-ADPR dependent TRPM2 activation at more physiological micromolar concentrations via binding to the NUDT9H domain (124).

A superagonist is significantly more potent or efficacious than other agonists. 2'-deoxy-ADPR activates TRPM2 with comparable potency but higher efficacy compared to ADPR and is therefore considered as TRPM2 superagonist (116). Further, 2'-deoxy-ADPR activation is less Ca^{2+} -dependent, which enables an increased channel open probability and 10-fold higher currents at physiological Ca^{2+} concentrations (116). Biosynthesis of 2'-deoxy-ADPR was demonstrated *in vitro* via generation of 2'-deoxy-NAD from NMN and 2'-deoxy-ATP by the cytosolic nicotinamide mononucleotide adenylyltransferase 2 (NMNAT-2) and subsequent hydrolysis to 2'-deoxy-ADPR and nicotinamide by CD38 (116). Interestingly, CD38 showed higher substrate preference for 2'-deoxy-NAD compared to

NAD (116). As increased ADPR generation induced under pathological situations depletes the cellular NAD pool, this likely affects cellular energy metabolism and NAD-dependent signaling processes. Therefore, it has been suggested that 2'-deoxy-ADPR-dependent TRPM2 activation plays a role under physiological conditions such as insulin secretion or neutrophil chemotaxis (116, 125, 126).

1.6.4 Evolutionary adaption of the NUDT9H domain

The function of the NUDT9H domain has changed decidedly during evolution. The NUDT9H domain in *nvTRPM2*, the most ancient TRPM2 channel, shows 49 % sequence identity to the pyrophosphatase NUDT9 and is catalytically active (127). Activation of *nvTRPM2* is independently of the NUDT9H domain, as removal of the domain maintains the channel responsive to ADPR via binding to the N-terminal binding site (127, 128). Further, *nvTRPM2* does not respond to hydrogen peroxide stimulation, because the catalytically active NUDT9H domain prevents ADPR accumulation through hydrolysis (88). During evolution, the pyrophosphatase activity of the NUDT9H domain was lost as it has been shown for *hsTRPM2* (96). Differences in channel gating properties such as activation and deactivation kinetics are further associated with differences in the NUDT9H domain (129).

2 Aim of the Thesis

ADPR is an important signaling molecule in the cell that is transferred from NAD⁺ onto proteins for posttranslational modification and regulates ion channel activation but is also potentially toxic for the cell. The pyrophosphatase NUDT9 and the ion channel TRPM2 are essential components of the ADPR signaling pathway. The aim of this thesis was the biophysical characterization of the pyrophosphatase NUDT9 and the homologous C-terminal domain of the TRPM2 channel. Investigating the substrate specificity of NUDT9 and its activity will also help our understanding of the NUDT9H domain of TRPM2. TRPM2 is activated by ADPR and regulated by Ca²⁺, Calmodulin and temperature. Using a broad spectrum of biophysical techniques, the understanding of the interplay between the regulatory factors should be improved.

3 Analysis of ligand-binding and resulting conformational changes in pyrophosphatase NUDT9

3.1 Abstract

So far, ADPR had been the only known physiologically relevant substrate of the pyrophosphatase NUDT9 (55). 2'-deoxy-ADPR was identified as an additional substrate, which is hydrolyzed to 2'-deoxy-AMP and ribose 5-phosphate with similar kinetics. The binding affinity for both ligands was determined to be in the nanomolar range. Only subtle differences between ADPR-binding and 2'-deoxy-ADPR binding were observed using several biophysical methods. Indeed, both ligands bind to an identical binding sites as shown by TROSY-NMR. Interestingly, substantial conformational changes occur once the ligands bind to NUDT9, suggesting a more compact and stable ligand bound form. Exchange of two amino acids in the NUDIX box of NUDT9 inactivates the pyrophosphatase, while the binding affinity for the ligands remains unchanged. Together with the ligand-induced conformational changes and the extraordinary ligand specificity, NUDT9 appears to be a suitable candidate for an ADPR FRET sensor. Development of genetically encoded fusion proteins with fluorescent proteins fused to the termini of NUDT9 failed. However, coupling of Alexa Fluor dyes to cysteine side chains of NUDT9 revealed a promising FRET sensor candidate that could serve as a starting point for further optimization.

3.2 Results

3.2.1 Expression and purification of NUDT9

The pET51b(+) vector was used to overexpress NUDT9 (residues 59-350, named NUDT9 wt) fused to a His₁₀ tag in BL21 (DE2) Gold *E.coli* cells. After cell lysis by sonication and removal of the cell debris, NUDT9 wt was purified from the supernatant using Ni²⁺-IMAC. The elution fractions were subjected to SEC analysis where NUDT9 wt mainly eluted as monomer at 16.8 mL (Figure 3.1 A). SDS-PAGE analysis confirmed the purity of the isolated NUDT9 wt protein and showed a single band at approx. 48 kDa (Figure 3.1 B).

3 ANALYSIS OF LIGAND-BINDING AND RESULTING CONFORMATIONAL CHANGES IN PYROPHOSPHATASE NUDT9

The expected size of NUDT9 wt is 35.4 kDa; a large discrepancy between observed and theoretical band size was also observed for other proteins (e.g. Calmodulin). Mass spectrometry confirmed the identity of NUDT9 wt.

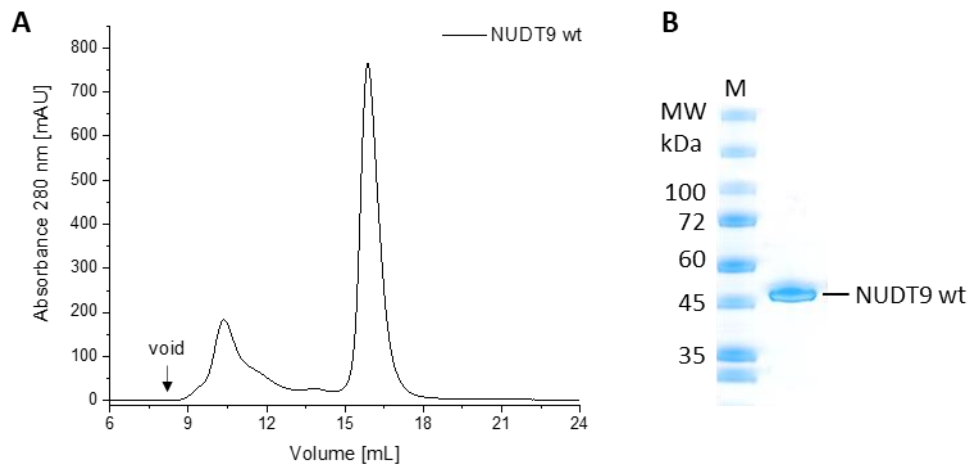


Figure 3.1: Purification of NUDT9 wt. (A) Size-exclusion chromatography (SEC) profile of Ni²⁺-IMAC elution fraction shows mainly monomeric NUDT9 wt that elutes at 16.8 mL on a S200 G10/300 column. (B) SDS-PAGE confirmed high purity of the isolated NUDT9 and showed a single band at approx. 48 kDa.

Although NUDT9 has been described as a monomer (70), in this work oligomeric forms such as dimers and large oligomers were also observed during size exclusion chromatography. The ratio between monomer, dimer and large oligomers varied and was not reproducible. Several of the following analyses were performed with all three forms, but no significant differences were detected. The monomeric NUDT9 appeared to be the most stable form. The following results were acquired with the monomeric NUDT9.

3.2.2 NUDT9 binds ADPR as well as its derivative 2'-deoxy ADPR

To this point, ADPR has been the only known endogenous substrate of NUDT9. ADPR is hydrolyzed to AMP and ribose 5-phosphate (3). Recently, Fliegert *et. al.* (116) discovered 2'-deoxy-ADPR as a ligand for the TRPM2 channel. They reported binding to the homologous NUDT9H domain of TRPM2. This raised the question whether 2'-deoxy-ADPR is also a substrate of NUDT9. To address this question 0.3 ng/ μ L NUDT9 wt were

3 ANALYSIS OF LIGAND-BINDING AND RESULTING CONFORMATIONAL CHANGES IN PYROPHOSPHATASE NUDT9

incubated with 1 μM , 3 μM , 10 μM or 30 μM ADPR or 2'-deoxy-ADPR, respectively. The results proved 2'-deoxy-ADPR to be a substrate for NUDT9 (Figure 3.2B). Using HPLC analysis, the breakdown products AMP and 2'-deoxy-AMP were quantified and the kinetic parameters K_M and v_{max} of the reactions were calculated (Table 3-1). These experiments were performed by Franziska Möckl.

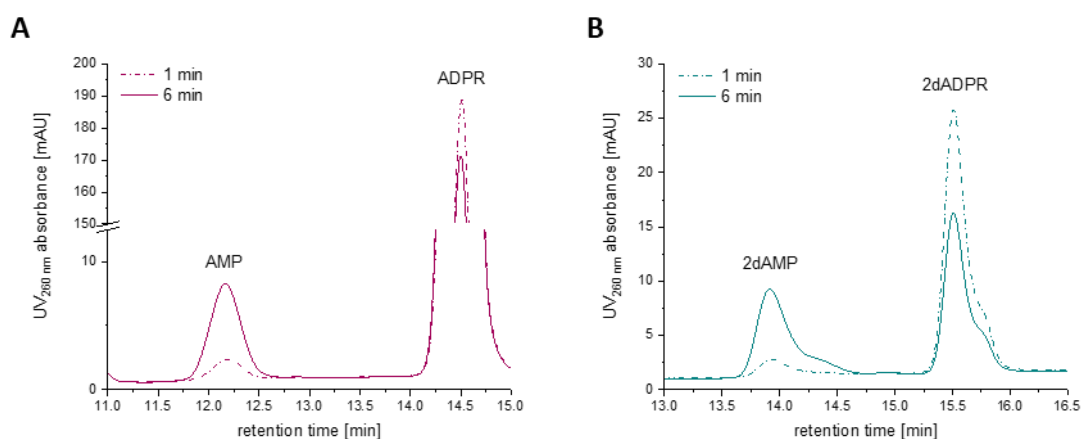


Figure 3.2: NUDT9 wt hydrolyzes ADPR and 2'-deoxy-ADPR to AMP or 2'-deoxy-AMP and ribose 5-phosphate. (A) AMP formation after 1 min and after 6 min incubation of 30 μM ADPR with 0.3 $\text{ng}/\mu\text{L}$ NUDT9 are shown. (B) 2'-deoxy-AMP formation after 1 min and after 6 min incubation of 30 μM 2'-deoxy-ADPR with 0.3 $\text{ng}/\mu\text{L}$ NUDT9 are shown.

Table 3-1: Kinetic parameters for the hydrolysis of ADPR and 2'-deoxy-ADPR by NUDT9 determined by HPLC analysis. K_M values do not differ significantly but v_{max} is significantly lower for 2'-deoxy-ADPR ($p < 0.005$). Values were determined from six independent experiments for ADPR and five independent experiments for 2'-deoxy-ADPR.

	K_M [$\mu\text{mol L}^{-1}$]	v_{max} [$\text{nmol min}^{-1} \mu\text{g}^{-1} \text{enzyme}$]	Specific enzyme activity [nkat mg^{-1}]
ADPR	3.0 ± 0.4	42.3 ± 1.5	2.4
2'-deoxy-ADPR	0.8 ± 0.3	17.4 ± 1.2	1.3

Statistical testing (extra sum-of-squares F test) revealed no significant differences for the K_M values but the v_{max} value was significantly lower for 2'-deoxy-ADPR ($p < 0.05$). NUDT9 showed an increased enzyme activity towards ADPR (2.4 nkat/mg) compared to 2'-deoxy-ADPR (1.3 nkat/mg).

3 ANALYSIS OF LIGAND-BINDING AND RESULTING CONFORMATIONAL CHANGES IN PYROPHOSPHATASE NUDT9

After confirming the hydrolysis of 2'-deoxy-ADPR by NUDT9 the potential differences of the two substrates were investigated. Binding measurements with Mg^{2+} as co-factors revealed a fast and highly exothermic reaction, which did not allow the deduction of binding affinities. Using Ca^{2+} as co-factor, the binding affinities could be determined (Figure 3.3).

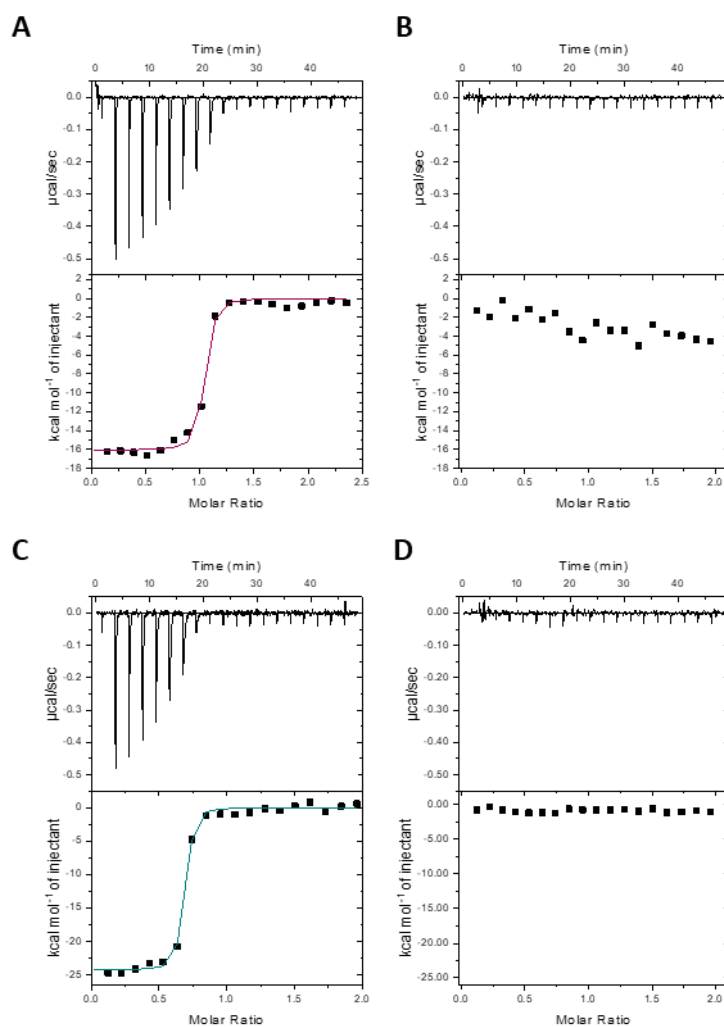


Figure 3.3: Binding affinities for ADPR and 2'-deoxy-ADPR to NUDT9 determined by ITC. (A) 200 μM ADPR binds to 10 μM NUDT9 with a K_D of 13 nM. (B) Control experiment of ADPR titrated into buffer. (C) 200 μM 2'-deoxy-ADPR binds to 10 μM NUDT9 with a K_D of 9 nM. (D) Control experiment of 2'-deoxy-ADPR titrated into buffer. All measurements were carried out at 20 $^\circ\text{C}$ and data were fitted using a single binding site model.

According to the thermodynamic parameters, binding of ADPR and 2'-deoxy-ADPR to NUDT9 wt is similar (Table 3-2). Both binding events are highly exothermic, the ΔH values differ by 887 cal/mol. The entropy of binding is negative for both ligands.

3 ANALYSIS OF LIGAND-BINDING AND RESULTING CONFORMATIONAL CHANGES IN PYROPHOSPHATASE NUDT9

Table 3-2: Thermodynamic parameters for binding of ADPR and 2'-deoxy-ADPR to wild type NUDT9 with Ca^{2+} as cofactor determined by ITC. Values were calculated from three independent experiments and are shown as average \pm standard deviation.

	K [M^{-1}]	K_D [nM]	ΔH [cal/mol]	ΔS [cal/mol $^{-1}$ /deg $^{-1}$]
NUDT9 wt + ADPR	$9.4\text{e}7 \pm 2.6\text{e}7$	12 ± 4	-1528 ± 70	-16 ± 3
NUDT9 wt + 2'- deoxy-ADPR	$1.1\text{e}8 \pm 2.4\text{e}7$	9 ± 2	-2415 ± 22	-46 ± 1

In comparison to ADPR, the breakdown products AMP and ribose 5-phosphate showed no binding to wild type NUDT9, neither did ADP (Figure 3.4).

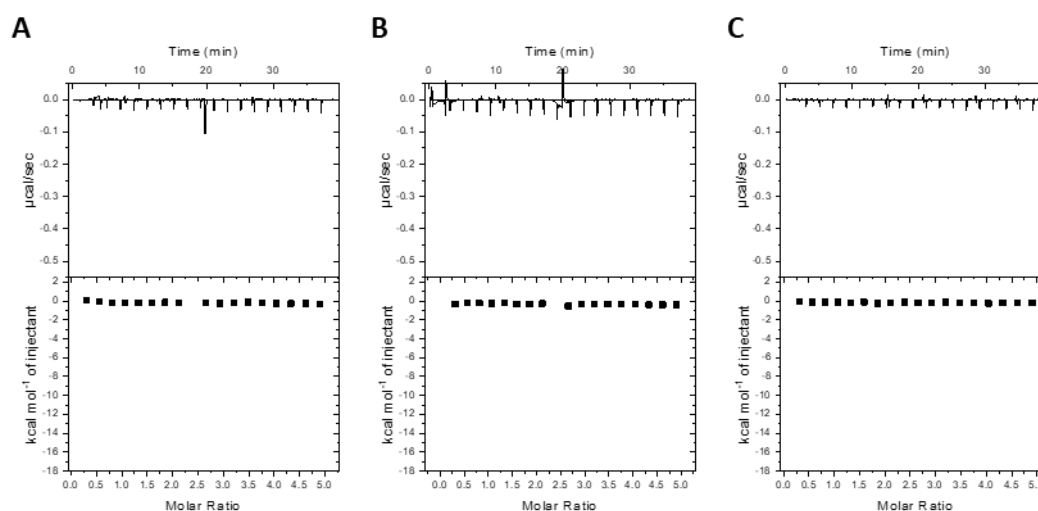


Figure 3.4: The breakdown products of ADPR, ribose 5-phosphate and AMP do not bind to wild type NUDT9 as measured by ITC. (A) 500 μM ribose 5-phosphate showed no binding to 10 μM wild type NUDT9. (B) 500 μM AMP showed no binding to 10 μM NUDT9 wt. (C) 500 μM ADP was titrated into 10 μM wild type NUDT9 and showed no binding. Mg^{2+} was used as cofactor in all measurements, which were carried out at 20 $^{\circ}\text{C}$.

Next to Mg^{2+} , also Zn^{2+} , Co^{2+} , Mn^{2+} and Cu^{2+} had been tested before as co-factors for the NUDT9 pyrophosphatase activity. Only with 20 mM Mn^{2+} as co-factor, NUDT9 was partially active and hydrolyzed ADPR (70). Since Ca^{2+} functioned as co-factor for binding ADPR and 2'-deoxy-ADPR (Figure 3.3), pyrophosphatase activity of wild type NUDT9 was analyzed by HPLC. 100 μg ADPR were incubated with 10 ng NUDT9 wt for 5 min and the

3 ANALYSIS OF LIGAND-BINDING AND RESULTING CONFORMATIONAL CHANGES IN PYROPHOSPHATASE NUDT9

amount of the breakdown product AMP was estimated by comparison with standard solutions (Figure 3.5).

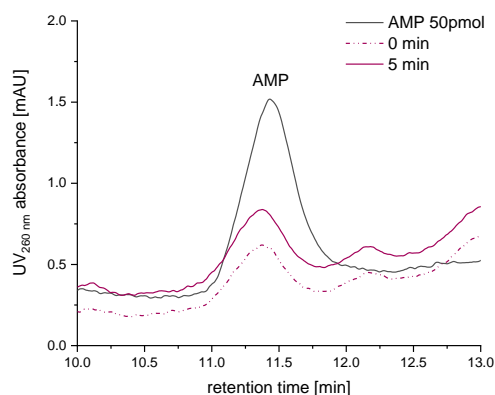


Figure 3.5: NUDT9 wt does not hydrolyze ADPR using Ca^{2+} as co-factor. Less than 50 pmol AMP were released by the hydrolysis of 180 nmol ADPR by NUDT9 wt using Ca^{2+} as co-factor.

Less than 50 pmol AMP were formed by NUDT9 wt out of 180 nmol ADPR within 5 min of incubation at 37 °C using Ca^{2+} as co-factor. This confirms that NUDT9 can bind ADPR in the presence of Ca^{2+} but cannot hydrolyze it like it does in the presence of Mg^{2+} .

3.2.3 Biophysical characterization of NUDT9 reveals sequential unfolding and large conformational changes upon substrate binding

To address potential differences in binding of ADPR or 2'-deoxy-ADPR to NUDT9 wt, various biophysical techniques were applied.

Circular dichroism (CD) spectroscopy revealed information about the folding of the protein. The CD spectrum of wild type NUDT9 showed predominantly α -helical folding with characteristic minima at 222 nm and 208 nm. This result was not altered by ligand binding (Figure 3.6).

3 ANALYSIS OF LIGAND-BINDING AND RESULTING CONFORMATIONAL CHANGES IN PYROPHOSPHATASE NUDT9

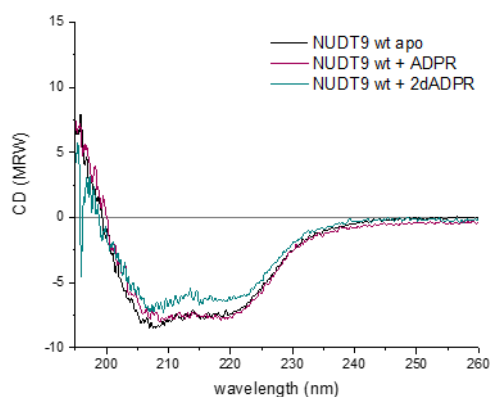


Figure 3.6: CD spectra of NUDT9 wt with or without ligand bound. The apo NUDT9 wt (black line) shows predominantly α -helical fold with minima at 222 nm and 208 nm. NUDT9 wt + ADPR (purple line) and NUDT9 wt + 2'-deoxy-ADPR (cyan line) show similar CD spectra.

The thermodynamic stability of wild type NUDT9 with or without ligand was analyzed by differential scanning fluorimetry. 10 μ M NUDT9 were melted in the presence of increasing concentrations of ADPR or 2'-deoxy-ADPR (50-1000 μ M each) and the intrinsic tryptophan fluorescence was monitored (Figure 3.7).

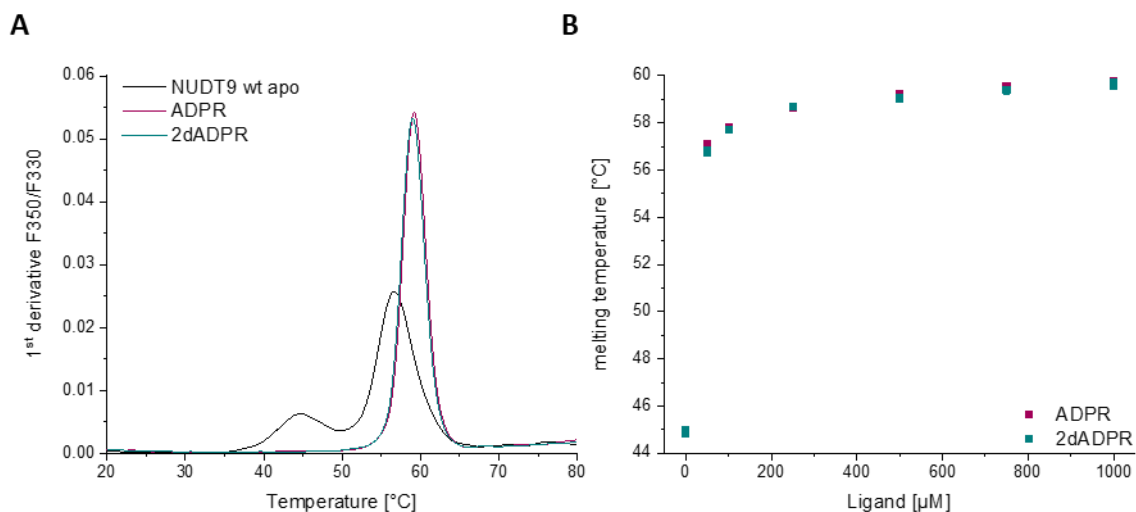


Figure 3.7: NUDT9 wt is thermally stabilized by binding of ADPR or 2'-deoxy-ADPR. (A) apo NUDT9 wt unfolds in two steps (black line) at 44.9 °C and 56.8 °C. NUDT9 wt bound to its ligands is more stable and unfolds at 59.2 °C with 500 μ M ADPR (purple line) or at 59.1 °C with 500 μ M 2'-deoxy-ADPR (cyan line). (B) NUDT9 wt is stabilized by increasing ligand concentrations. There is no difference between ADPR (purple squares) and 2'-deoxy-ADPR (cyan squares).

3 ANALYSIS OF LIGAND-BINDING AND RESULTING CONFORMATIONAL CHANGES IN PYROPHOSPHATASE NUDT9

Apo wild type NUDT9 showed an unfolding profile with two peaks with maxima at 44.9 °C and 56.8 °C. In the presence of ADPR or 2'-deoxy-ADPR however, wild type NUDT9 unfolded in one step. The ligand-bound protein was stabilized and melts at 59.2 °C or 59.1 °C (Figure 3.7A). With increasing ligand concentrations, wild type NUDT9 was stabilized to a greater extent; there were no differences between ADPR and 2'-deoxy-ADPR (Figure 3.7B).

In order to assess structural properties of ligand binding to NUDT9, small angle X-ray scattering (SAXS) was applied. SAXS is a technique that allows the analysis of proteins under near physiological conditions. Conformational changes in response to variations in external conditions are observed. Low q SAXS values reveal the size of a particle and mid q values give information about inter-particle interactions. SAXS curves were recorded for apo wild type NUDT9 and compared to those from NUDT9 bound to ADPR (Figure 3.8).

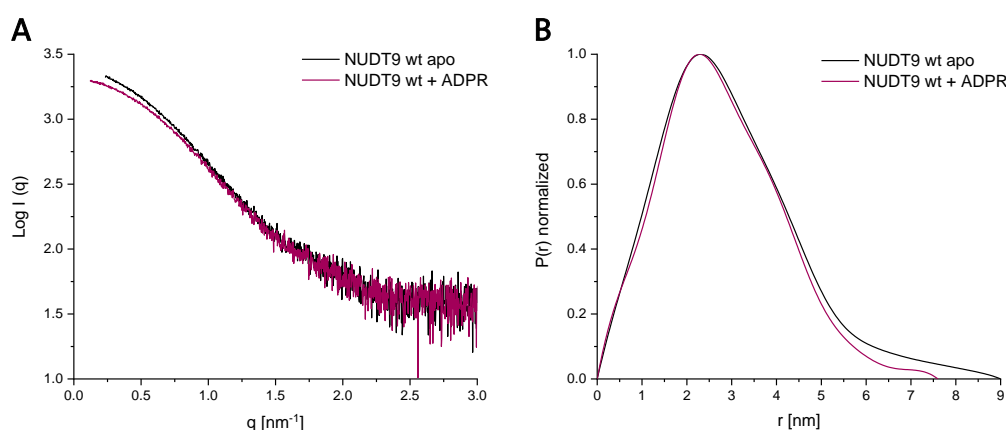


Figure 3.8: NUDT9 wt bound to ADPR is more compact than the apo NUDT9 wt as revealed by SAXS. (A) The scattering plot for apo NUDT9 wt (black curve) compared to NUDT9 wt bound to ADPR shows significant differences in the low q range. (B) The distance distribution function reveals a maximum particle dimension for apo NUDT9 wt of 9.0 Å compared to 7.6 Å for the ADPR bound form.

The comparison of the scattering plots of apo wild type NUDT9 and the ADPR-bound NUDT9 revealed a significant difference in the low q range, indicating a large conformational change upon ligand binding (Figure 3.8A). This observation was confirmed by the distance distribution function: The ADPR-bound NUDT9 had a more

3 ANALYSIS OF LIGAND-BINDING AND RESULTING CONFORMATIONAL CHANGES IN PYROPHOSPHATASE NUDT9

compact form than the apo NUDT9 (Figure 3.8B). The maximum particle dimension for apo wild type NUDT9 was 9.0 Å and decreased to 7.6 Å once ADPR was bound.

In 2003 the crystal structure of NUDT9 was determined (57). Two different structures were published: the apo NUDT9 (pdb: 1Q33) and NUDT9 in complex with ribose 5-phosphate and Mg^{2+} (pdb: 1QVJ). Up to now, a crystal structure of NUDT9 in complex with ADPR is not available. In order to compare the SAXS data to the crystal structure, theoretical SAXS curves of the crystal structures were calculated using CRY SOL in the ATSAS software package (Figure 3.9).

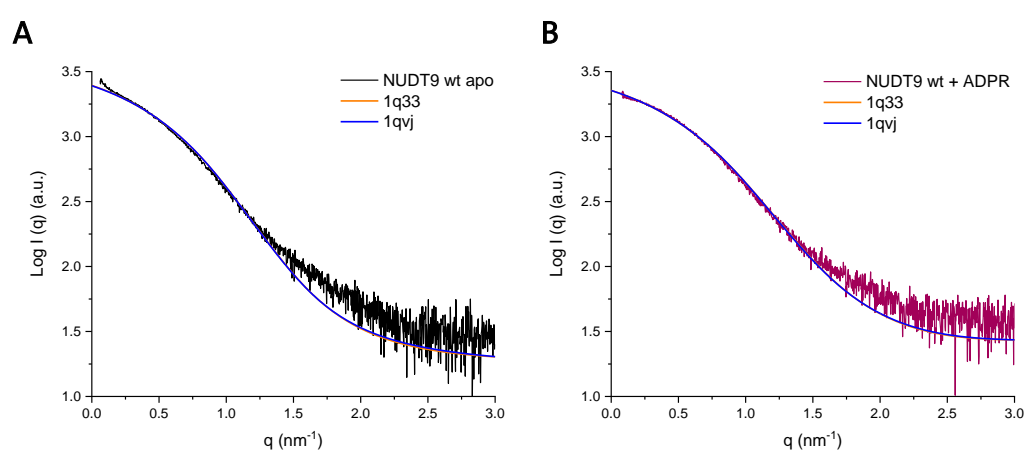


Figure 3.9: Scattering plots of apo NUDT9 wt and NUDT9 wt in complex with ADPR compared to calculated scattering curves derived from the crystal structures of NUDT9 (1q33 and 1qvj). (A) The comparison of the scattering curves of the crystal structures of apo NUDT9 (1q33, orange line) and NUDT9 in complex with ribose 5-phosphate and Mg^{2+} (1qvj, blue line) as well as the scattering plot of apo NUDT9 wt (black curve) reveals differences, in particular in the low q range. (B) The scattering plot of the ADPR-bound NUDT9 wt (purple curve) and the calculated scattering curves of the crystal structures superimpose to a high degree.

The alignment of the calculated scattering curves of the two crystal structures of NUDT9 revealed no differences at all. In comparison to the SAXS scattering plots of apo wild type NUDT9 and the ADPR-bound form, the calculated scattering curves of the crystal structures superimposed much better to the ADPR-bound NUDT9 (Figure 3.9B). The curves superimpose especially in the low q range, suggesting that the crystal structures represent the more compact conformation of wild type NUDT9.

The crystal structures of NUDT9 show a mainly disordered C-terminus. To verify that the conformational changes upon ligand binding observed by SAXS were independent of the

flexible C-terminus, a version of a truncated C-terminus (residue 59-339, named NUDT9trC) was created. This truncation also deleted a cysteine residue within the C-terminal linker, which might have been responsible for oligomeric forms of NUDT9 due to intermolecular disulfide bridges.

Protein expression and purification of NUDT9trC was similar to wild type NUDT9. A TEV cleavage site was introduced to remove the C-terminal His₁₀-tag. In addition to the wild type NUDT9 purification protocol, a second Ni²⁺-IMAC was performed after TEV cleavage to remove the TEV protease and the cleaved His₁₀-tag. Large oligomeric complexes disappeared in the size exclusion chromatograms but the dimeric NUDT9trC was still observed in several purifications. Thus, the oligomerization of NUDT9 cannot only be dependent on intermolecular disulfide bridging between the C-terminal linkers. A second cysteine in vicinity to the proposed ADPR binding pocket is still present in NUDT9trC which may also be responsible for oligomerization. Only the monomeric NUDT9trC was used for the following analyses.

The thermal stability addressed by nDSF confirmed the stabilization of NUDT9trC once the ligands ADPR or 2'-deoxy-ADPR bind (Figure 3.10). The two-step unfolding of the apo NUDT9trC is less distinct than it was for the wild type NUDT9 (Figure 3.7A) but a pre-shoulder of the peak is still present (Figure 3.10A). NUDT9trC in complex with ADPR or 2'-deoxy-ADPR is stabilized up to 57.3 °C and 57.4 °C (Figure 3.10B).

3 ANALYSIS OF LIGAND-BINDING AND RESULTING CONFORMATIONAL CHANGES IN PYROPHOSPHATASE NUDT9

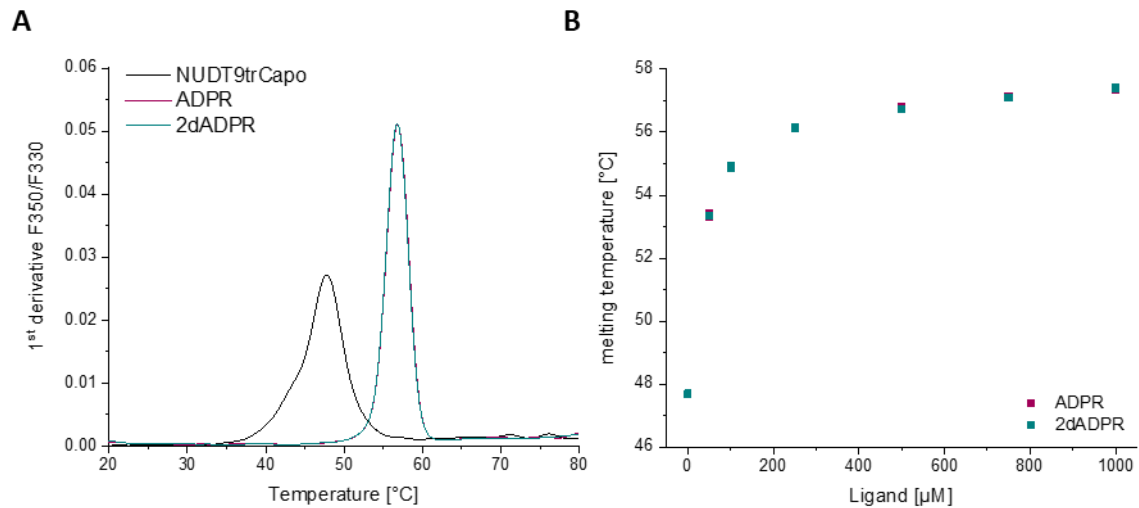


Figure 3.10: NUDT9trC is thermally stabilized by binding of ADPR or 2'-deoxy-ADPR. (A) apo NUDT9trC (black line) unfolds at 47.7 °C. NUDT9trC bound to its ligands is more stable and unfolds at 57.3 °C with 500 μM ADPR (purple line) or at 57.4 °C with 500 μM 2'-deoxy-ADPR (cyan line). (B) NUDT9trC is stabilized by increasing ligand concentrations. There is no difference between ADPR (purple squares) and 2'-deoxy-ADPR (cyan squares).

SAXS analysis of NUDT9trC confirmed the more compact form of the ligand-bound form (Figure 3.11). The conformational differences of the apo and ligand bound form in the scattering plots (Figure 3.11A) was less obvious compared to wild type NUDT9 (Figure 3.9A) but could be confirmed by the distance distribution functions (Figure 3.11B). Apo NUDT9trC had a maximum particle dimension of 8.0 Å that decreased to 7.2 Å or 7.4 Å once ADPR or 2'-deoxy-ADPR were bound.

3 ANALYSIS OF LIGAND-BINDING AND RESULTING CONFORMATIONAL CHANGES IN PYROPHOSPHATASE NUDT9

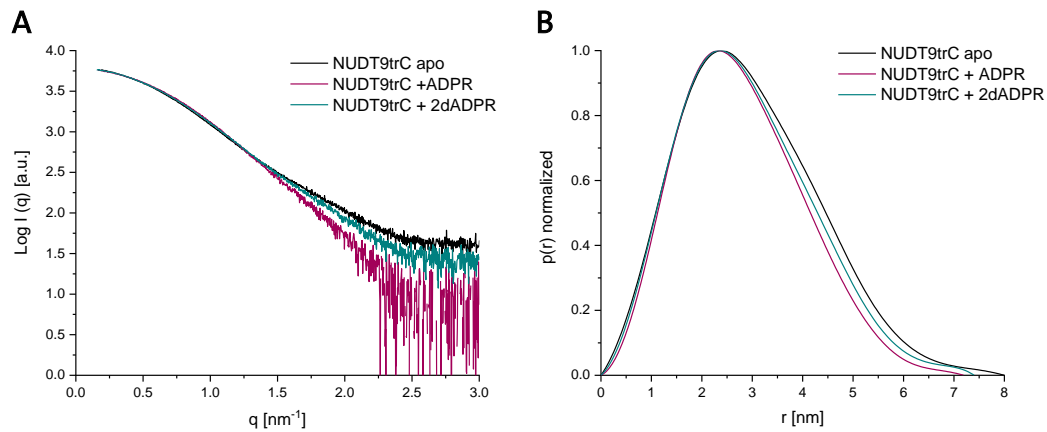


Figure 3.11: NUDT9trC in complex with ADPR or 2'-deoxy-ADPR is more compact than the apo NUDT9trC as revealed by SAXS. (A) Scattering plots observed for apo NUDT9trC (black curve), NUDT9trC bound to ADPR (purple curve) and bound to 2'-deoxy-ADPR (cyan curve). (B) The distance distribution function reveals a maximum particle dimension for apo NUDT9trC of 8.0 Å (black) compared to 7.2 Å for the ADPR-bound form (purple) and 7.4 Å for the 2'-deoxy-ADPR-bound form (cyan).

The NUDT9trC construct was used for extensive crystallization trials to obtain a crystal structure in complex with ADPR or 2'-deoxy-ADPR. Several crystals appeared in conditions with high ammonium sulfate concentrations, but reasonable diffraction images were only obtained from one crystal.

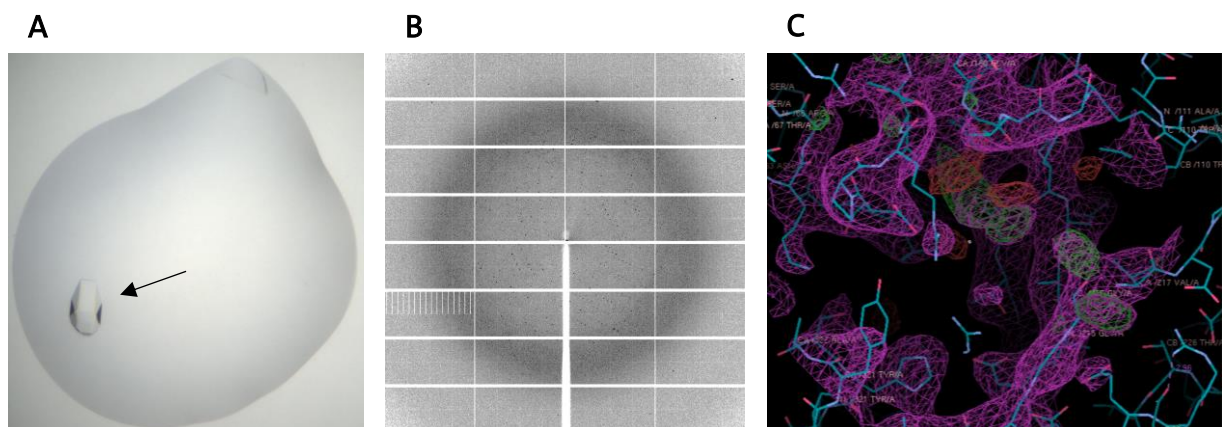


Figure 3.12: Crystallization trials of NUDT9trC in complex with ADPR. (A) Two large crystals were obtained in 5 % PEG300, 150 mM MES, pH 6, 2 M $(\text{NH}_4)_2\text{SO}_4$. (B) Diffraction images with spots up to 2 Å were recorded. (C) The obtained crystal structure superimposed mainly with the published structures of NUDT9 (pdb: 1Q33 or 1QVJ) and showed no density for ADPR.

Molecular replacement using the published NUDT9 crystal structures (pdb: 1Q33 and 1QVJ) allowed model building for the new X-ray data. Unfortunately, the binding pocket of NUDT9 showed no electron density for ADPR (Figure 3.12C).

3.2.4 Mutation of the NUDIX box inactivates pyrophosphatase NUDT9

NUDT9 shows a high sequence similarity of 50 % to the C-terminal NUDT9H domain of the *hs*TRPM2 channel (3). The NUDT9H domain is indispensable for TRPM2 gating by ADPR but it was never separately shown, that ADPR binds the NUDT9H domain. In addition, a remaining pyrophosphatase activity of the NUDT9H domain was long debated. Several amino acids in the NUDIX box are proposed to be responsible for the pyrophosphatase activity (3, 78). A NUDT9trC variant with mutations of the amino acids E230 and F231 (E230I, F231L) was cloned and named NUDT9trC RIL.

Using ITC, binding affinities for ADPR and 2'-deoxy-ADPR to NUDT9trC RIL were determined (Figure 3.13); Mg^{2+} served as co-factor.

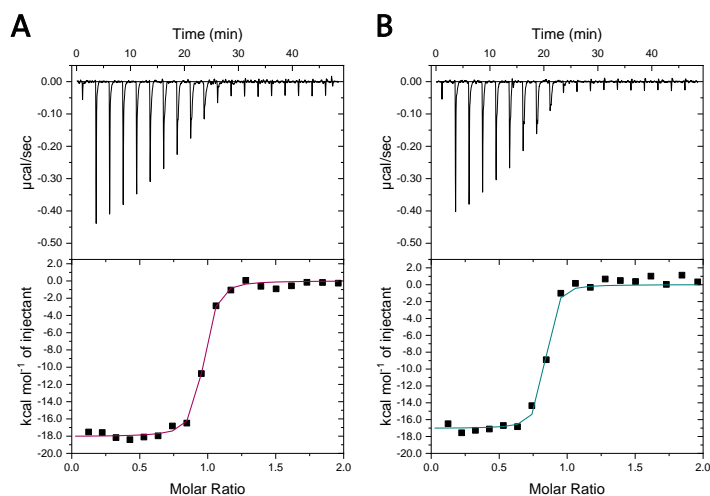


Figure 3.13: Binding affinities for ADPR and 2'-deoxy-ADPR to NUDT9trC RIL as determined by ITC. (A) 200 μM ADPR binds to 10 μM NUDT9 with a K_D of 19 nM. (B) 200 μM 2'-deoxy-ADPR binds to 10 μM NUDT9trC RIL with a K_D of 14 nM. Measurements were performed at 20 $^{\circ}\text{C}$ and data were fitted using a single binding site model.

3 ANALYSIS OF LIGAND-BINDING AND RESULTING CONFORMATIONAL CHANGES IN PYROPHOSPHATASE NUDT9

Table 3-3: Thermodynamic parameters for the binding of ADPR and 2'-deoxy-ADPR to NUDT9trC RIL using Mg^{2+} as co-factor as determined by ITC. Values were calculated from three independent experiments and are shown as average \pm standard deviation.

	K [M^{-1}]	K_D [nM]	ΔH [cal/mol]	ΔS [cal/mol ⁻¹ /deg ⁻¹]
NUDT9trC RIL + ADPR	$6.4e7 \pm 1.6e7$	16 ± 4	-1795 ± 17	-26 ± 1
NUDT9trC RIL + 2'- deoxy-ADPR	$1.3e8 \pm 1.2e8$	12 ± 7	-1656 ± 48	-20 ± 2

The binding affinities for ADPR and 2'-deoxy-ADPR to NUDT9trC RIL are comparable to each other (Table 3-3) and to those obtained for wild type NUDT9 (Figure 3.3, Table 3-2). Neither the shortening of the C terminus, nor the mutation of the NUDIX box affects the binding affinity of the ligands to NUDT9. However, the binding enthalpies and entropies of the two ligands are very similar, in contrast to the differences measured for the wild type NUDT9 (Table 3-2).

The ITC profile with reasonable signal intensities proposed no pyrophosphatase activity for NUDT9trC RIL and this was confirmed by HPLC analysis of the breakdown products AMP or 2'-deoxy-AMP. 100 μg ADPR or 2'-deoxy-ADPR were incubated with 10 ng NUDT9trC RIL for up to 1 h at 37 °C. None of the substrates was significantly hydrolyzed, less than 50 pmol AMP or 2'-deoxy-AMP was produced within 1 h (Figure 3.14).

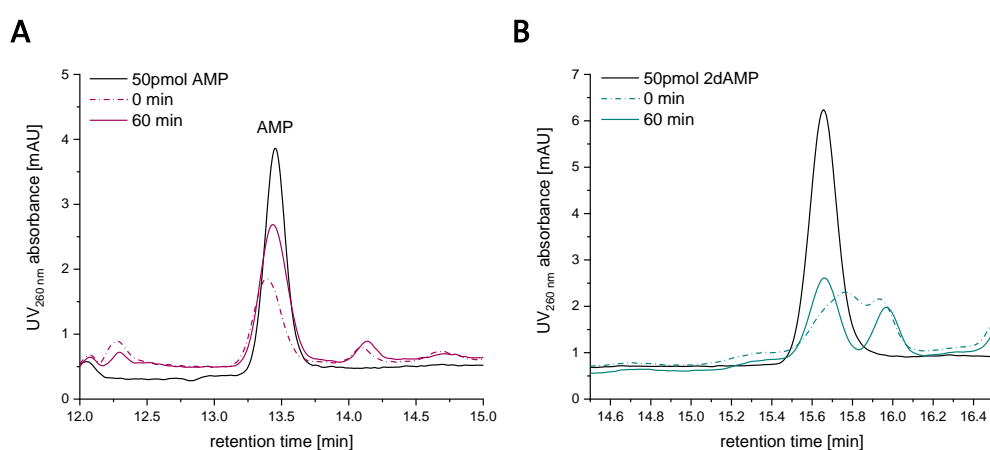


Figure 3.14: NUDT9trC RIL shows no significant pyrophosphatase activity against ADPR or 2'-deoxy-ADPR. (A) Less than 50 pmol AMP were produced within 1 h out of 180 μg ADPR. (B) Less than 50 pmol 2'-deoxy-AMP were produced within 1 h out of 187 μg 2'-deoxy-ADPR.

3 ANALYSIS OF LIGAND-BINDING AND RESULTING CONFORMATIONAL CHANGES IN PYROPHOSPHATASE NUDT9

Using nDSF, the thermal stability of NUDT9trC RIL was analyzed. Comparable to wild type NUDT9 and NUDT9trC, 10 μM NUDT9trC RIL apo as well as in complex with increasing concentrations of ADPR or 2'-deoxy-ADPR (50-1000 μM) was unfolded while monitoring the intrinsic tryptophan fluorescence. Apo NUDT9trC RIL showed a melting profile with two peaks with maxima at 44.5 $^{\circ}\text{C}$ and 52.0 $^{\circ}\text{C}$ (Figure 3.15A). NUDT9trC RIL was stabilized by increasing ligand concentrations up to 56.9 $^{\circ}\text{C}$ for ADPR and 57.1 $^{\circ}\text{C}$ for 2'-deoxy-ADPR (Figure 3.15B).

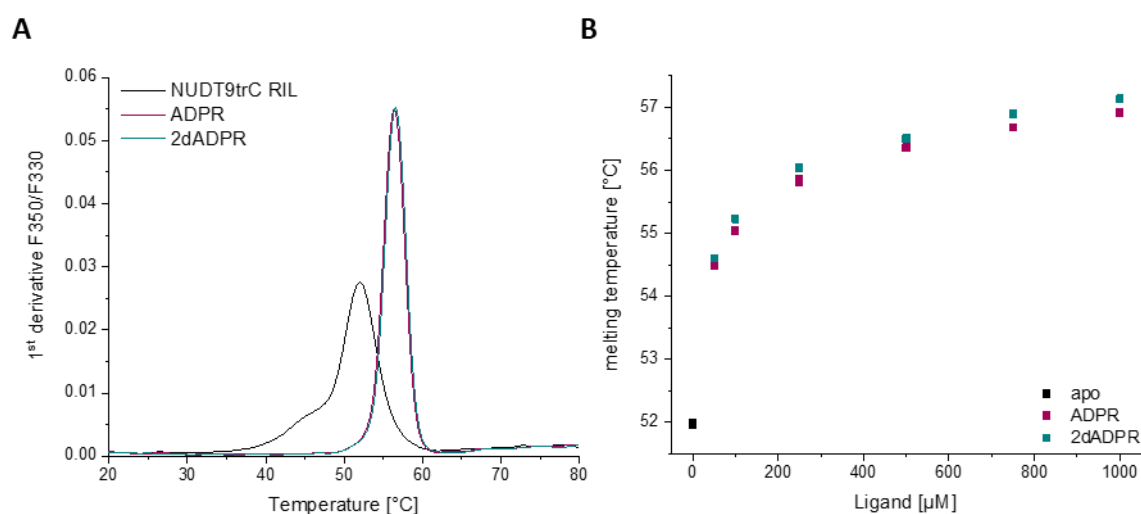


Figure 3.15: NUDT9trC RIL is thermally stabilized by binding of ADPR or 2'-deoxy-ADPR. (A) Apo NUDT9trC RIL (black line) unfolds at 44.5 $^{\circ}\text{C}$ and 52.0 $^{\circ}\text{C}$. NUDT9trC RIL bound to its ligands is more stable and unfolds at 56.4 $^{\circ}\text{C}$ with 500 μM ADPR (purple line) or at 56.5 $^{\circ}\text{C}$ with 500 μM 2'-deoxy-ADPR (cyan line). (B) NUDT9trC is stabilized by increasing ligand concentrations. There is no significant difference between ADPR (purple squares) and 2'-deoxy-ADPR (cyan squares).

Moreover, SAXS data was generated for NUDT9trC RIL. No differences were observed in comparison to NUDT9trC (Figure 3.11): The ligand-bound form of NUDT9trC RIL was again more compact than the apo form (Figure 3.16). Apo NUDT9trC RIL spanned a maximum particle dimension of 8.0 \AA which decreases to 7.3 \AA once ADPR or 2'-deoxy-ADPR were bound.

3 ANALYSIS OF LIGAND-BINDING AND RESULTING CONFORMATIONAL CHANGES IN PYROPHOSPHATASE NUDT9

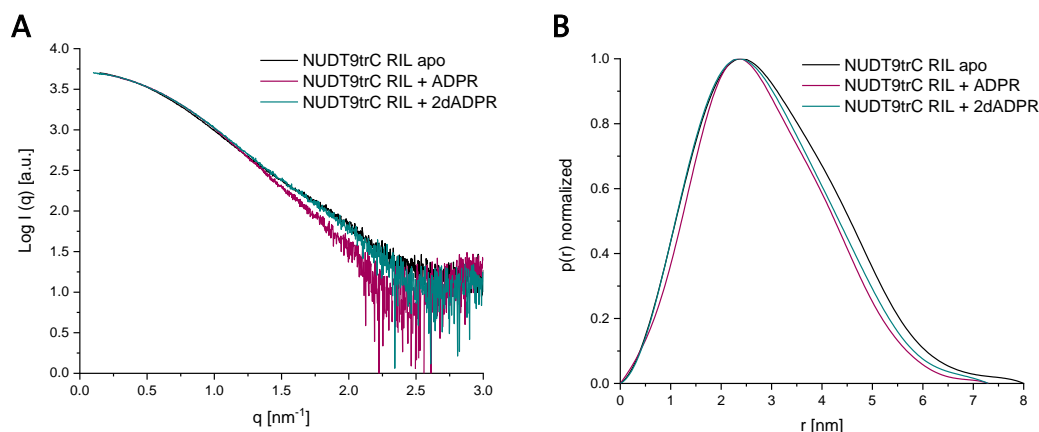


Figure 3.16: NUDT9trC RIL bound to ADPR or 2'-deoxy-ADPR is more compact than the apo NUDT9trC RIL revealed by SAXS. (A) Scattering plots observed for apo NUDT9trC RIL (black curve), NUDT9trC RIL bound to ADPR (purple curve) and bound to 2'-deoxy-ADPR (cyan curve). (B) The distance distribution function reveals a maximum particle dimension for apo NUDT9trC RIL of 8.0 Å (black) compared to 7.3 Å both for the ADPR (purple) and the 2'-deoxy-ADPR bound form (cyan).

3.2.5 ADPR and 2'-deoxy-ADPR bind to the identical site as determined by NMR

All NMR measurements as well as the NMR data analysis were performed by Trevor J. Rutherford at the Laboratory for Molecular Biology in Cambridge, UK. 2D TROSY NMR spectra were recorded to compare NUDT9trC RIL in complex with ADPR and 2'-deoxy-ADPR on an amino acid residue level. *E.coli* cells were grown in minimal media with ¹⁵NH₄Cl as exclusive nitrogen source. The protein was purified as described for NUDT9trC and NUDT9trC RIL. The size exclusion profile showed only monomeric ¹⁵N NUDT9trC RIL. NMR measurements were performed in Ca²⁺ buffer with 10 % D₂O to achieve water suppression.

3 ANALYSIS OF LIGAND-BINDING AND RESULTING CONFORMATIONAL CHANGES IN PYROPHOSPHATASE NUDT9

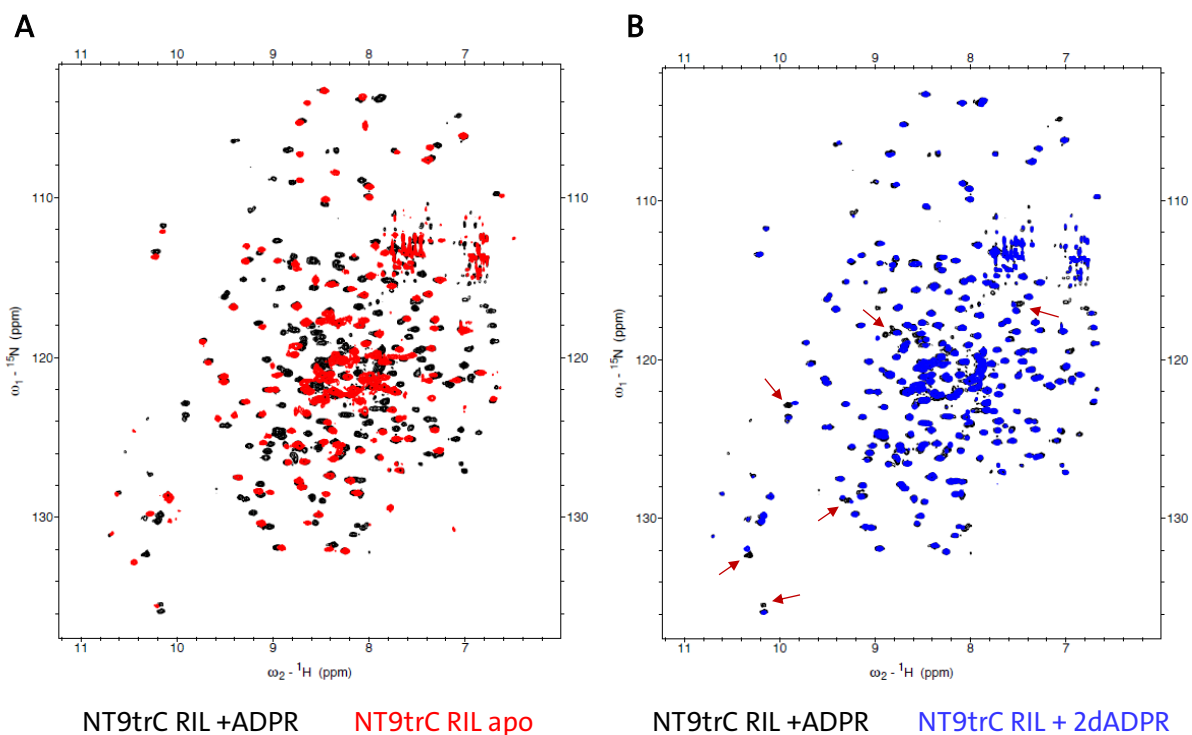


Figure 3.17: ^1H - ^{15}N -TROSY NMR spectra for apo NUDT9trC RIL and in complex with ADPR or 2'-deoxy-ADPR indicate large conformational changes for the complex but only minor differences for the ligands. (A) Comparison of apo NUDT9trC RIL (red) and the ADPR complex (black) indicates large conformational changes. (B) ADPR (black) and 2'-deoxy-ADPR (blue) bind to the same binding site as there appear only minor differences in the NMR spectra. NMR spectra were acquired at 293 K for 5 h using an 800 MHz spectrometer. Differences between the two ligand-bound spectra are indicated by red arrows.

All NMR spectra show distinct and well-dispersed signals, consistent with a well-ordered protein structure (Figure 3.17). Comparison of the apo NUDT9trC RIL to the ADPR-bound complex spectra indicate massive changes (Figure 3.17A). Many signals of the apo NUDT9trC RIL disappear or shift. The overall signal number increases for the ADPR-bound complex suggesting a coordination of the protein around the ligand. Those results confirm previous SAXS results indicating an ADPR stabilized complex of NUDT9. A control sample of the apo NUDT9 with slightly shifted pH confirmed the ADPR dependence and excluded environment-induced changes.

Comparison of ^1H - ^{15}N -TROSY NMR spectra for ADPR and 2'-deoxy-ADPR show mainly identical signals and indicate an identical binding site for the two ligands (Figure 3.17B).

3 ANALYSIS OF LIGAND-BINDING AND RESULTING CONFORMATIONAL CHANGES IN PYROPHOSPHATASE NUDT9

Only six signals shift significantly (indicated by arrows), which appears reasonable for the structural difference in the 2'-position of the first ribose of the two ligands.

Since the signals in the TROSY NMR spectra are highly dispersed, a $^2\text{D}, ^{13}\text{C}, ^{15}\text{N}$ labelled NUDT9trC RIL was produced to perform a sequence specific backbone resonance peak assignment (Figure 3.18). This allowed the identification of the residues that are involved in ligand binding and of the ones that show differences for ADPR compared to 2'-deoxy-ADPR.

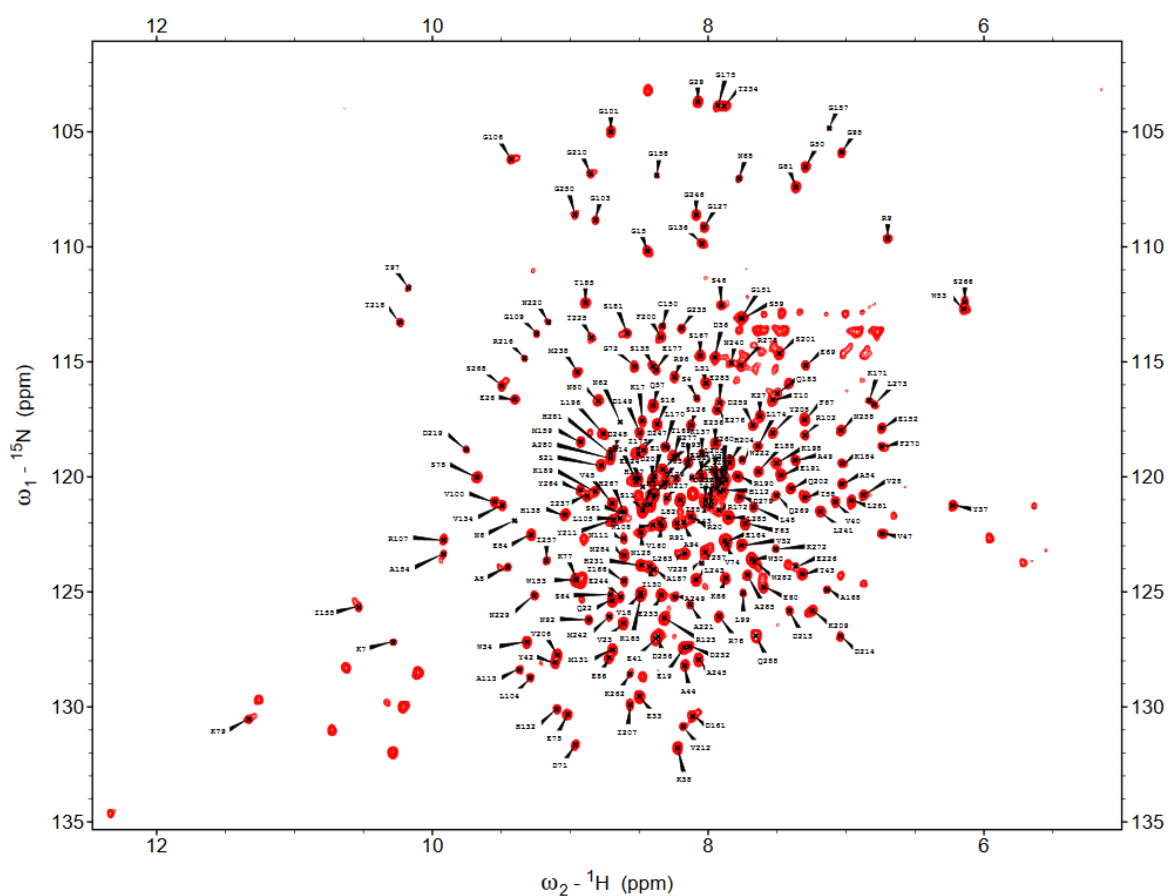


Figure 3.18: Backbone resonance assignment of ADPR bound NUDT9trC RIL covers 85 % of the signals.

Residues Leu161 (ω_1 128.734/ ω_2 9.289), Arg164 (ω_1 122.752/ ω_2 9.918) and Asp218 (ω_1 130.418/ ω_2 8.111) were identified (entire table see section 9.1) to be shifted in the ADPR compared to 2'-deoxy-ADPR complex. Leu161, Arg164 and Asp218 align the second part of the NUDT9 ligand binding pocket and most likely interact with the adenosine part of ADPR (Figure 3.19).

Residues Asp172, Asp271, Arg273 and Tyr321 were identified in the crystal structure of NUDT9 in complex with ribose 5-phosphate and Mg^{2+} (57) to interact with the ribose (Figure 3.19). Those residues were assigned and show no shift in the 2'-deoxy-ADPR NMR spectra.

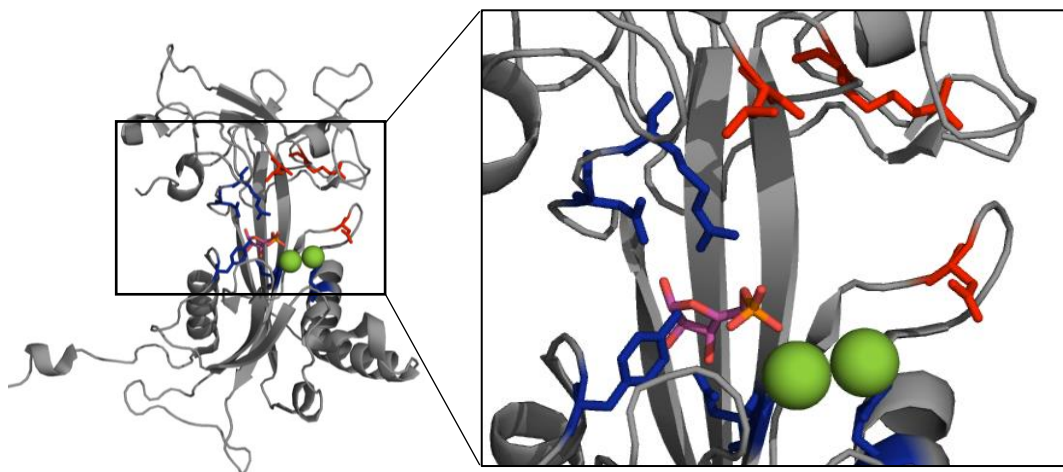


Figure 3.19: Ligand binding pocket of NUDT9 with residues interacting with the ligands identified by crystallography and NMR. Residues interacting with ribose 5-phosphate and Mg^{2+} were identified in the crystal structure (pdb: 1QVJ, sticks representation in blue). Residues interacting with the adenosine were identified by NMR (sticks representation in red).

3.2.6 Development of a FRET probe for ADPR based on NUDT9

The high substrate specificity for ADPR and 2'-deoxy-ADPR and the substantial conformational changes occurring upon ligand binding qualify NUDT9 RIL as potential intramolecular FRET probe. Two approaches were pursued: a genetically encoded FRET sensor with NUDT9 fused to fluorescent proteins and NUDT9 fused to Alexa Fluor dyes by maleimide click chemistry (Figure 3.20).

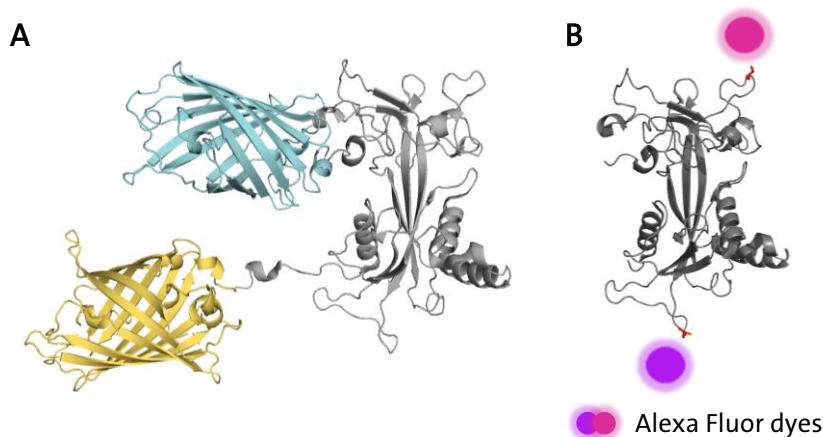


Figure 3.20: Illustration of potential NUDT9 based FRET sensors for ADPR. (A) Genetically encoded FRET sensor with fluorescent proteins fused to the termini of NUDT9. (B) Alexa Fluor dyes coupled to NUDT9 by click chemistry.

3.2.6.1 ADPR FRET sensor: NUDT9 fused to fluorescent proteins

For the approach of a genetically encoded FRET sensor, the termini of NUDT9 were tagged with a pair of fluorescent proteins. Various candidates were screened for their proposed FRET distance r_0 using the FPbase FRET calculator (130). The FRET pairs mTFP1-mVenus and CFP-YFP were chosen. mTFP1-mVenus qualified due to its excellent donor properties and a commercially available kit with circular permutations of both donor and acceptor, that allows the testing of variations in dipole orientation. The disadvantage is its large r_0 value of 60.0 Å. CFP-YFP qualified with an advantageously shorter r_0 value of 47.5 Å. However, it features poorer donor properties and no commercially available modification kits suitable for bacterial expression.

Full-length NUDT9 RIL (amino acid 59-350) and NUDT9trC RIL (amino acids 59-339) served as starting proteins. To increase the distance between the fluorescent proteins, NUDT9trC was further shortened C-terminally to helix 7 (amino acid 59-336) and a rigid linker helix of two or five repetitions of the amino acid sequence (EAAAK)_n was introduced. An EAAAK amino acid sequence is supposed to form a rigid linker helix stabilized by salt bridges between glutamate and lysine (131).

The proteins were overexpressed in *E.coli* BL21 Gold cells, purified by Ni²⁺-IMAC and gel filtrated on a Superdex S200 10/300 column. The peak identity was assessed by SDS-PAGE (Figure 3.21).

3 ANALYSIS OF LIGAND-BINDING AND RESULTING CONFORMATIONAL CHANGES IN PYROPHOSPHATASE NUDT9

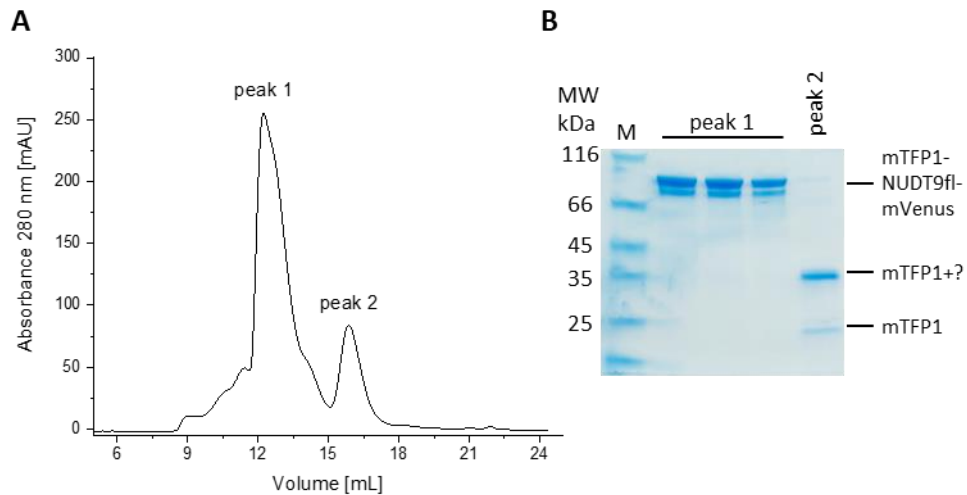


Figure 3.21: Purification of mTFP1-full length NUDT9 RIL-mVenus FRET sensor from *E.coli*. (A) SEC profile shows two peaks. (B) SDS-PAGE of the SEC fractions showed two indistinguishable bands for the first peak with the expected size of the FRET sensor. The second peak is most likely a breakdown product of the FRET sensor.

The size exclusion profile showed two peaks with elution volumes of 12.5 mL and 15.8 mL (Figure 3.21A). The SDS-PAGE revealed two indistinguishable bands for the first peak at the expected size of the mTFP1-full length NUDT9 RIL-mVenus FRET sensor of approx. 92 kDa. The protein identity of all three bands was confirmed by mass spectrometry. The second size exclusion peak showed a single band of approx. 35 kDa on the SDS-PAGE. A yellow solution suggested a fluorescent protein, but the single mTFP1 or mVenus only have a molecular mass of 24 kDa. Thus, a breakdown product of the FRET sensor protein was assumed.

25-50 nM of the FRET sensor proteins were used for fluorescent measurements on a Cary Eclipse spectral fluorimeter (Agilent, US). The apo FRET sensor protein as well as the complex with 50 μ M ADPR were excited at 462 nm and a fluorescence emission scan was acquired.

3 ANALYSIS OF LIGAND-BINDING AND RESULTING CONFORMATIONAL CHANGES IN PYROPHOSPHATASE NUDT9

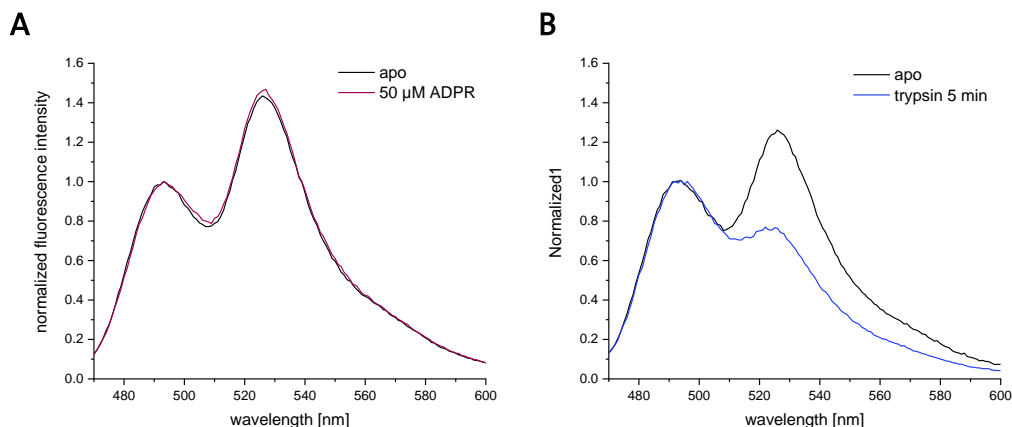


Figure 3.22: Fluorescent measurements of mTFP1-mVenus FRET proteins show FRET. (A) 50 nM mTFP1-full length NUDT9 RIL-mVenus showed FRET, but the signal was similar for the apo protein (black curve) and the complex with 50 μ M ADPR (purple curve). (B) The FRET signal of a mTFP1-NUDT9trC_{D336} RIL – (EAAAK)₂ – mVenus sensor decreased (blue curve) after incubation with trypsin for 5 min. FRET proteins were excited at 462 nm, the emission spectra were scanned from 470–600 nm. Slits were set to 5 nm.

FRET was observed for all FRET proteins tested, only the ratio of acceptor to donor varied. A negative control in which the FRET signal was abrogated was required to verify the system. The FRET signal was significantly decreased by incubation with trypsin (Figure 3.22B). Since the fluorescent proteins are very stable β -barrel proteins, it was assumed that mainly NUDT9 is digested by trypsin, which results in larger distances for the fluorescent proteins and subsequently in loss of FRET. The constructed FRET sensor proteins, their FRET ratios and the relative change upon ADPR addition are summarized in Table 3-4.

Table 3-4: Summary of calculated acceptor to donor ratios for apo FRET proteins, the ADPR-bound form and the relative change of the ratios.

mTFP-mVenus FRET sensor	Ratio A / D apo	Ratio A / D 50 μ M ADPR	Δ Ratio [%]
NUDT9fl	1.45	1.49	3.0
NUDT9trC _{W339}	1.140	1.15	1.0
NUDT9trC _{D336} (EAAAK) ₂	1.20	1.21	1.0
NUDT9trC _{D336} (EAAAK) ₅	1.06	1.08	2.2

A ratio >1 represents a strong acceptor signal indicating an effective FRET energy transfer. The strongest FRET signal was observed for the full length NUDT9 FRET fusion

3 ANALYSIS OF LIGAND-BINDING AND RESULTING CONFORMATIONAL CHANGES IN PYROPHOSPHATASE NUDT9

protein. An almost equal donor acceptor ratio was observed for the NUDT9trC_{D336} FRET fusion protein interspaced by five helix turns of the rigid linker. None of the tested fusion proteins showed a sufficient change in FRET after the addition of ADPR. The slight changes that were measured nonetheless, all showed a gain in FRET upon ADPR addition supporting the previous data of a more compact form of the ADPR-bound NUDT9 (Table 3-4).

To confirm the binding of ADPR to the fusion protein, ITC measurements were performed for the mTFP1-NUDT9trC_{W339}-mVenus and the mTFP1-NUDT9trC_{D336} (EAAAK)₅-mVenus variants (Figure 3.23).

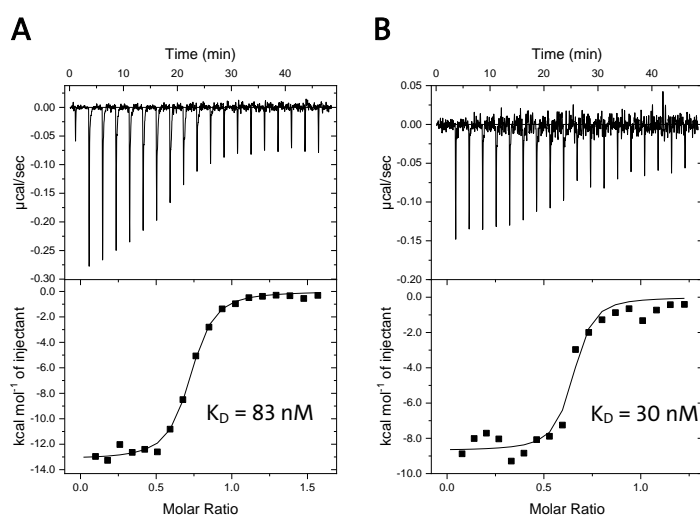


Figure 3.23: ITC measurements of mTFP1-mVenus fusion proteins of NUDT9trC_{W339} and NUDT9trC_{D336} (EAAAK)₅ confirm a nanomolar binding affinity. (A) Binding of ADPR to mTFP1-NUDT9trC_{W339}-mVenus shows a K_D of 83 nM. (B) Binding of ADPR to mTFP1-NUDT9trC_{D336} (EAAAK)₅-mVenus shows a K_D of 30 nM. Measurements were performed at 20 °C and data were fitted using a single binding site model.

For both fusion proteins tested, the nanomolar binding affinity for ADPR was confirmed (Figure 3.23). Thus, the coupling of NUDT9 to large fluorescent proteins does not seem to affect its binding affinity towards ADPR.

Further, mTFP1-NUDT9trC_{W339}-mVenus and mTFP1-NUDT9trC_{D336} (EAAAK)₅-mVenus were subjected to SAXS analysis to confirm substantial conformational changes of the ADPR complex (Figure 3.24).

3 ANALYSIS OF LIGAND-BINDING AND RESULTING CONFORMATIONAL CHANGES IN PYROPHOSPHATASE NUDT9

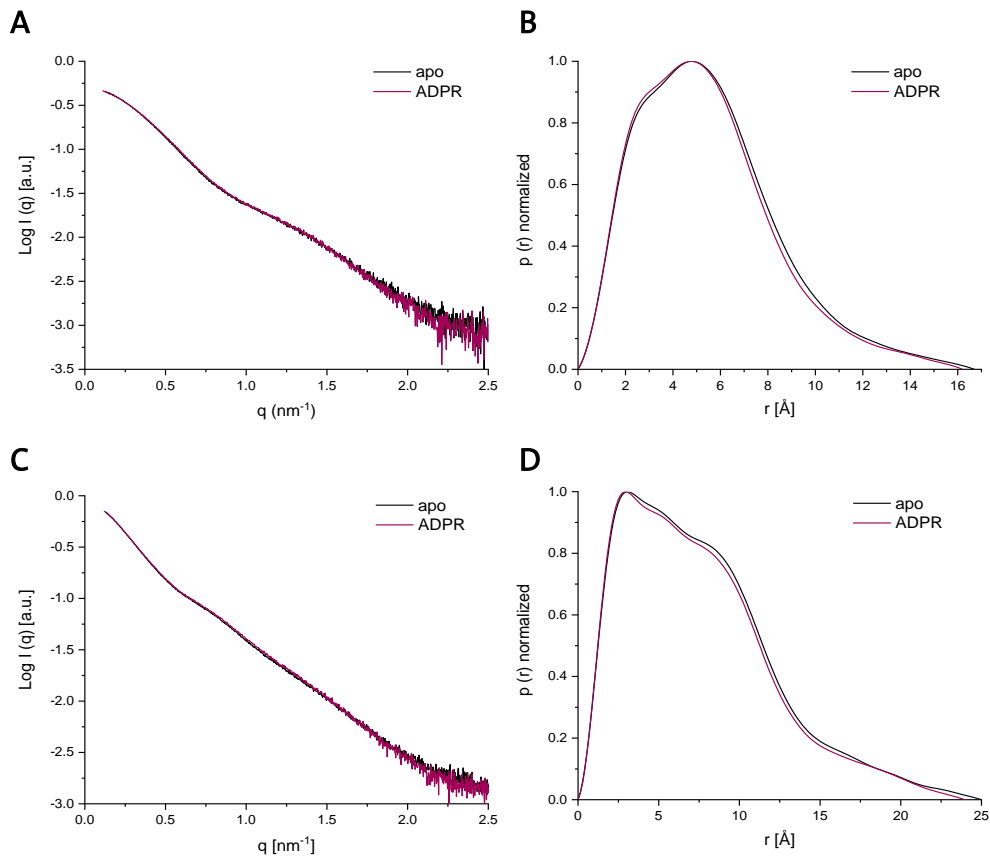


Figure 3.24: Genetically encoded mTFP1-mVenus NUDT9 FRET fusion proteins undergo subtle conformational changes upon ADPR binding. (A+B) Results for mTFP1-NUDT9trC_{W339}-mVenus. (A) Scattering plot shows no obvious differences once ADPR binds. (B) The maximum particle dimension for mTFP1-NUDT9trC_{W339}-mVenus is larger for the apo (black curve) form than for the ADPR bound form (purple curve). (C+D) Results for mTFP1-NUDT9trC_{D336} (EAAAK)₅-mVenus. (C) Scattering plot shows no obvious differences once ADPR binds. (D) The maximum particle dimension for mTFP1-NUDT9trC_{D336} (EAAAK)₅-mVenus is larger for the apo (black curve) form than for the ADPR bound form (purple curve).

Both, mTFP1-NUDT9trC_{W339}-mVenus and mTFP1-NUDT9trC_{D336} (EAAAK)₅-mVenus showed a reduced maximum particle dimension once ADPR was bound. The maximum particle dimension of mTFP1-NUDT9trC_{W339}-mVenus decreased from 16.7 \AA to 16.2 \AA (Figure 3.24B). The maximum particle dimension of mTFP1-NUDT9trC_{D336} (EAAAK)₅-mVenus decreased from 25.0 \AA to 24.0 \AA (Figure 3.24D).

Since the distance of 60.0 \AA appeared to be too large to detect changes in FRET upon ADPR binding, circularly permuted (cp) variants of mTFP1 and mVenus were tested. Those variants ought to modify the dipole orientation of the fluorophores and allow the detection of a change in the FRET signal. Cp variants of both, the donor mTFP1 and the

**3 ANALYSIS OF LIGAND-BINDING AND RESULTING CONFORMATIONAL CHANGES IN
PYROPHOSPHATASE NUDT9**

acceptor mVenus were cloned, purified, and tested for the full length NUDT9, NUDT9trC_{W339} and for NUDT9trC_{D336} (EAAAK)₅ variants (Table 3-5). Changes in the gelfiltration elution volume for the FRET sensor peak (ranging from 12.0 mL to 13.1 mL) indicated variations in the overall shape of the different cp variants.

Table 3-5: Summary of calculated acceptor to donor ratios for apo FRET proteins, the ADPR bound form and the relative change of the ratios for several cp variants of the mTFP1 and mVenus FRET pair.

mTFP1-mVenus FRET sensor	Ratio A / D apo	Ratio A / D 50 μ M ADPR	Δ Ratio [%]
wt-NUDT9fl-cp157	1.64	1.63	0.4
wt-NUDT9fl-cp173	1.69	1.64	2.9
wt-NUDT9fl-cp195	1.49	1.47	0.9
wt-NUDT9fl-cp229	1.30	1.31	0.2
cp105-NUDT9fl-wt	1.63	1.63	0.5
cp159-NUDT9fl-wt	1.03	1.07	4.0
cp195-NUDT9fl-wt	1.21	1.22	0.2
cp227-NUDT9fl-wt	1.33	1.32	0.8
wt-NUDT9trC _{W339} -cp157	1.75	1.77	1.4
wt-NUDT9trC _{W339} -cp173	2.12	2.08	2.0
wt-NUDT9trC _{W339} -cp195	1.69	1.68	1.0
wt-NUDT9trC _{W339} -cp229	1.56	1.57	0.5
cp105-NUDT9trC _{W339} -wt	1.48	1.47	0.7
cp159-NUDT9trC _{W339} -wt	1.29	1.27	1.9
cp195-NUDT9trC _{W339} -wt	1.34	1.32	2.0
cp227-NUDT9trC _{W339} -wt	1.39	1.37	0.9
wt-NUDT9trC _{D336} (EAAAK) ₅ -cp157	n.d.	n.d.	n.d.
wt-NUDT9trC _{D336} (EAAAK) ₅ -cp173	0.67	0.67	0.6
wt-NUDT9trC _{D336} (EAAAK) ₅ -cp195	1.33	1.32	0.9
wt-NUDT9trC _{D336} (EAAAK) ₅ -cp229	1.28	1.29	0.8

3 ANALYSIS OF LIGAND-BINDING AND RESULTING CONFORMATIONAL CHANGES IN PYROPHOSPHATASE NUDT9

None of the new FRET sensors showed a sufficient change in the ratio upon ADPR binding. The biggest gain in FRET was observed for mTFP1cp₁₅₉-full length NT9fl-mVenus wt with a change of 4.0 %. Only mTFP1wt-NUDT9trC_{D336} (EAAAK)₅-mVenus cp₁₇₃ showed an acceptor to donor ratio <1 suggesting a less effective energy transfer. This at least implies reasonable effects of the cp variants of the fluorescent proteins. In contrast to the original mTFP1-mVenus FRET sensor variants (Table 3-4), some of the cp variants also show decreasing acceptor signal upon ADPR binding (Table 3-5). Nevertheless, none the tested FRET pairs reach a sufficient ratio change of about 10 %.

The CFP-YFP pair occupies a smaller FRET distance r_0 of 47.5 nm compared to mTFP1-mVenus and was also tested for an ADPR sensor based on NUDT9. Three different variants were cloned, purified, and tested analogous to the mTFP1-mVenus constructs (Table 3-6).

Table 3-6: Summary of calculated acceptor to donor ratios for apo FRET proteins, the ADPR bound form and the relative change of the ratios for several cp variants of the CFP-YFP FRET pair.

CFP-YFP FRET sensor	Ratio A / D apo	Ratio A / D 250 μ M ADPR	Δ Ratio [%]
NUDT9fl	0.82	0.80	1.4
NUDT9trC _{E341}	1.76	1.78	0.9
NUDT9trC _{D336} (EAAAK) ₂	0.84	0.84	0.3

None of the three tested CFP-NUDT9-YFP FRET sensors showed a significant change in the ratio upon ADPR binding (Table 3-6). CFP-full length NUDT9-YFP and CFP-NUDT9trC_{D336} (EAAAK)₂-YFP indicated ineffective FRET (acceptor to donor ratio <1) in contrast to the CFP-NUDT9trC_{E341}-YFP variant that shows very strong FRET.

3.2.6.2 ADPR FRET sensor: NUDT9 coupled to Alexa Fluor dyes

The coupling of chemical fluorophores to side chains is an alternative to coupling fluorescent proteins to the termini of NUDT9. Cysteine coupling via maleimide click chemistry is widely used and highly specific. The thiol moiety in cysteines reacts with the maleimide by forming a stable thioether bond between the side chain and the fluorophore (Figure 3.25).

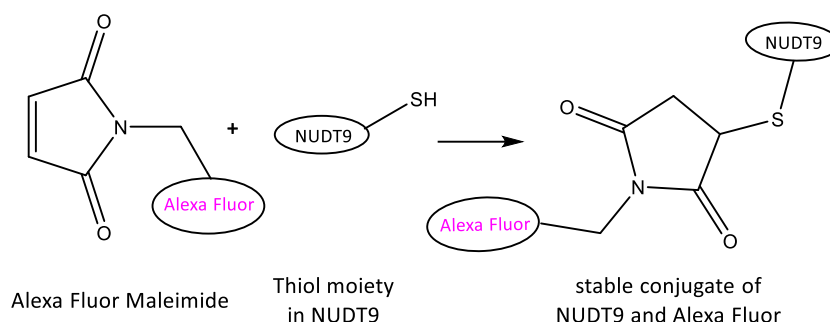


Figure 3.25: Conjugation reaction of a cysteine residue in NUDT9 to Alexa Fluor Maleimide gives an Alexa Fluor coupled NUDT9 FRET probe.

NUDT9trC possesses only one cysteine (position 207) which is located near the proposed ligand binding pocket (Figure 3.26A). To allow site specific labelling with Alexa Fluor dyes, this cysteine was mutated to serine. Prior to further investigations, it was important to estimate the impact of the Cys207 on the binding of ADPR. The NUDT9trC RIL C207S mutant was purified and the binding affinity for ADPR was examined by ITC (Figure 3.26B).

3 ANALYSIS OF LIGAND-BINDING AND RESULTING CONFORMATIONAL CHANGES IN PYROPHOSPHATASE NUDT9

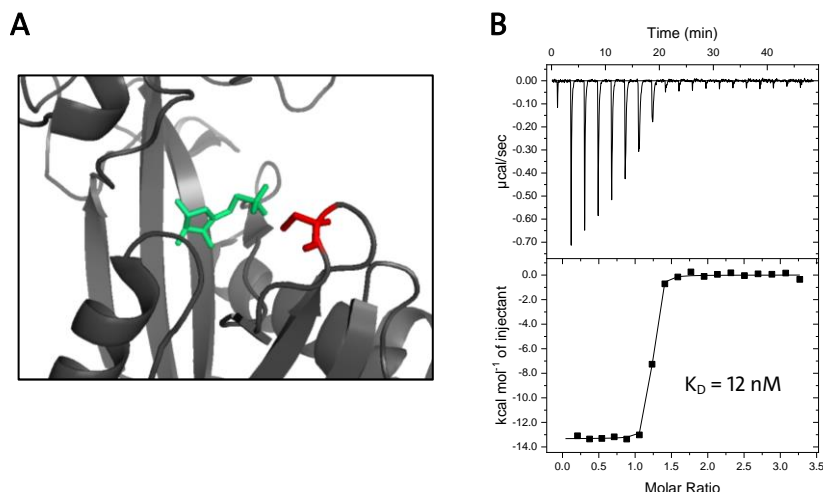


Figure 3.26: Cys207 in NUDT9 does not affect the binding affinity of ADPR. (A) Cartoon representation of the binding pocket of NUDT9 (pdb: 1QVJ) with ribose 5-phosphate (green) and the Cys207 (red). (B) The binding affinity of the NUDT9trC RIL C207S mutant is 12 nM. ITC measurements were performed at 20 °C and data were fitted using a single binding site model.

The binding affinity of 12 nM for ADPR to NUDT9trC RIL C207S (Figure 3.26) is comparable to those determined for NUDT9trC RIL (Table 3-3) and wild type NUDT9 (Table 3-2). This suggested that the Cys207 does not participate in ADPR binding.

Following this clarification, all serine residues in NUDT9 were evaluated for their surface accessibility and their proposed distances to each other in the crystal structure. Four serine residues were chosen to be mutated to cysteines for site-specific fluorophore labelling: Ser78 and Ser118 in the cap of NUDT9, Ser182 and Ser243 in the core of NUDT9. All selected residues are located in loop regions, but Ser243 is at the end of helix four (Figure 3.28A). Three combinations were formed: (1) Cys78 to Cys243 separated by 51 nm, (2) Cys78 to Cys182 separated by 58 nm, and (3) Cys118 to Cys182 separated by 67 nm (Table 3-7).

Table 3-7: Proposed distances between mutated cysteine pairs chosen for Alexa Fluor labelling in NUDT9trC. Distances were calculated in the NUDT9 crystal structure (pdb: 1Q33) using the measurement wizard in Pymol.

Positions for labelling	Proposed distance [\AA]
S78C – S243C	51
S78C – S182C	58
S118C – S182C	67

3 ANALYSIS OF LIGAND-BINDING AND RESULTING CONFORMATIONAL CHANGES IN PYROPHOSPHATASE NUDT9

Alexa Fluor dyes were selected as fluorescent dyes for a NUDT9 FRET sensor, because they are bright, photostable and insensitive to pH changes (132).

NUDT9trC RIL was purified by Ni²⁺-IMAC and gel filtration as described before. 50 μM purified protein was mixed with five-fold excess of each Alexa Fluor dye (ten-fold excess of Alexa Fluor dyes in total) and incubated over night at 4 °C or for 2 h at room temperature. Unbound dye was consumed by the addition of 2 mM β-mercaptoethanol and removed using a PD-10 column. Absorbance spectra of the elution fractions were measured, and the amount of labelled protein was estimated. The labelling efficiency was almost 100 % and unaffected by labelling at 4 °C overnight or at room temperature for 2 h. However, the ratio between the two bound fluorophores differed slightly within individual experiments. Incubation with excess of one or the other Alexa Fluor dye could not solve this problem. The first PD-10 elution fraction contained the labelled protein and was further gelfiltered (Figure 3.27).

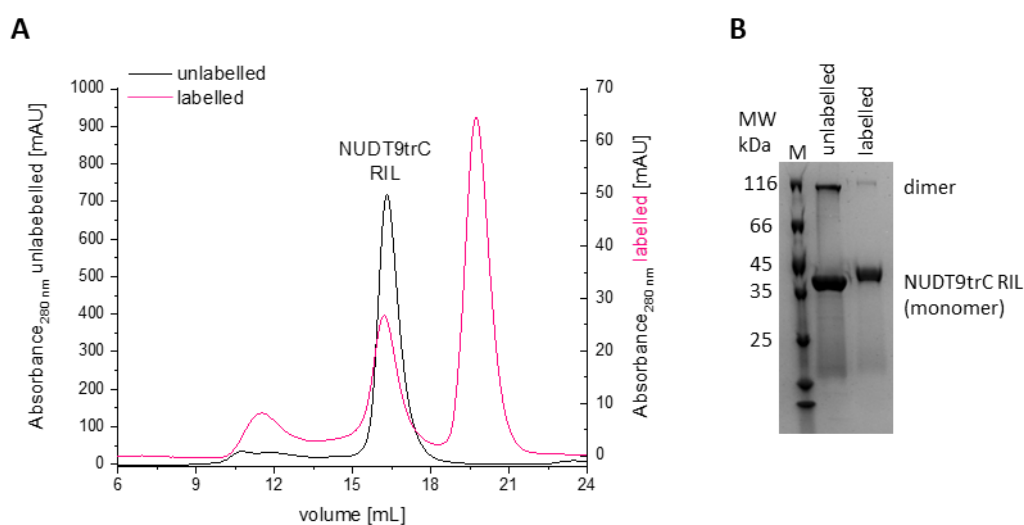


Figure 3.27: Purification and comparison of unlabelled and Alexa Fluor labelled NUDT9trC RIL. (A) Gelfiltration elution profile of unlabelled (black line) and Alexa Fluor labelled (pink line) NUDT9trC RIL confirms labelling of monomeric NUDT9trC RIL. An additional large peak of free Alexa Fluor dyes is present in the labelled chromatogram. (B) Successful labelling is confirmed by a band with higher molecular mass in the SDS-PAGE.

Native NUDT9trC RIL elutes at 16.3 mL, whereas Alexa Fluor labelled NUDT9trC RIL eluted slightly earlier at 16.2 mL (Figure 3.27A). An additional peak at 19.7 mL revealed a colored solution but no visible protein on the SDS-PAGE and indicates residual unbound dye that

3 ANALYSIS OF LIGAND-BINDING AND RESULTING CONFORMATIONAL CHANGES IN PYROPHOSPHATASE NUDT9

could not be removed by PD-10 purification. Successful labelling was confirmed by SDS-PAGE, the labelled protein showed a slightly larger band compared to the unlabeled NUDT9trC RIL (Figure 3.27B).

All mutated cysteines were coupled to the FRET pair Alexa Fluor 555 and Alexa Fluor 594 with a FRET distance r_0 of 47 nm. To span a broader range of distances, Cys118 and Cys182 (predicted distance of 67 nm) were also coupled to the FRET pair Alexa Fluor 488 and Alexa Fluor 546 (r_0 64 nm) or Alexa Fluor 488 and Alexa Fluor 594 (r_0 60 nm).

Fluorescence measurements were carried out with 500 nM protein and 250 μ M ADPR (Figure 3.28, Table 3-9). The donors were not excited at their maxima but at lower wavelengths, because the excitation spectra of all Alexa Fluor donor and acceptor combinations overlap to a certain extend (Table 3-8).

Table 3-8: Spectral properties of the used Alexa Fluor dye combinations. Theoretical values were obtained from the fpbase FRET calculator (<https://www.fpbase.org/fret/>). The last row indicates the experimentally determined emission maxima used for ratio calculations.

Alexa Fluor donor / acceptor	R_0 [Å]	Max. spectral overlap [%]	Excitation donor [nm]	Excitation donor [%]	Excitation acceptor [%]	FRET emission _{exp} donor / acceptor [nm]
488 + 546	64	31.4	470	37.2	4	519 / 573
488 + 594	60	20.5	470	37.2	2.8	519 / 612
555 + 594	47	60.0	519	50.5	14.3	564 / 612

3 ANALYSIS OF LIGAND-BINDING AND RESULTING CONFORMATIONAL CHANGES IN PYROPHOSPHATASE NUDT9

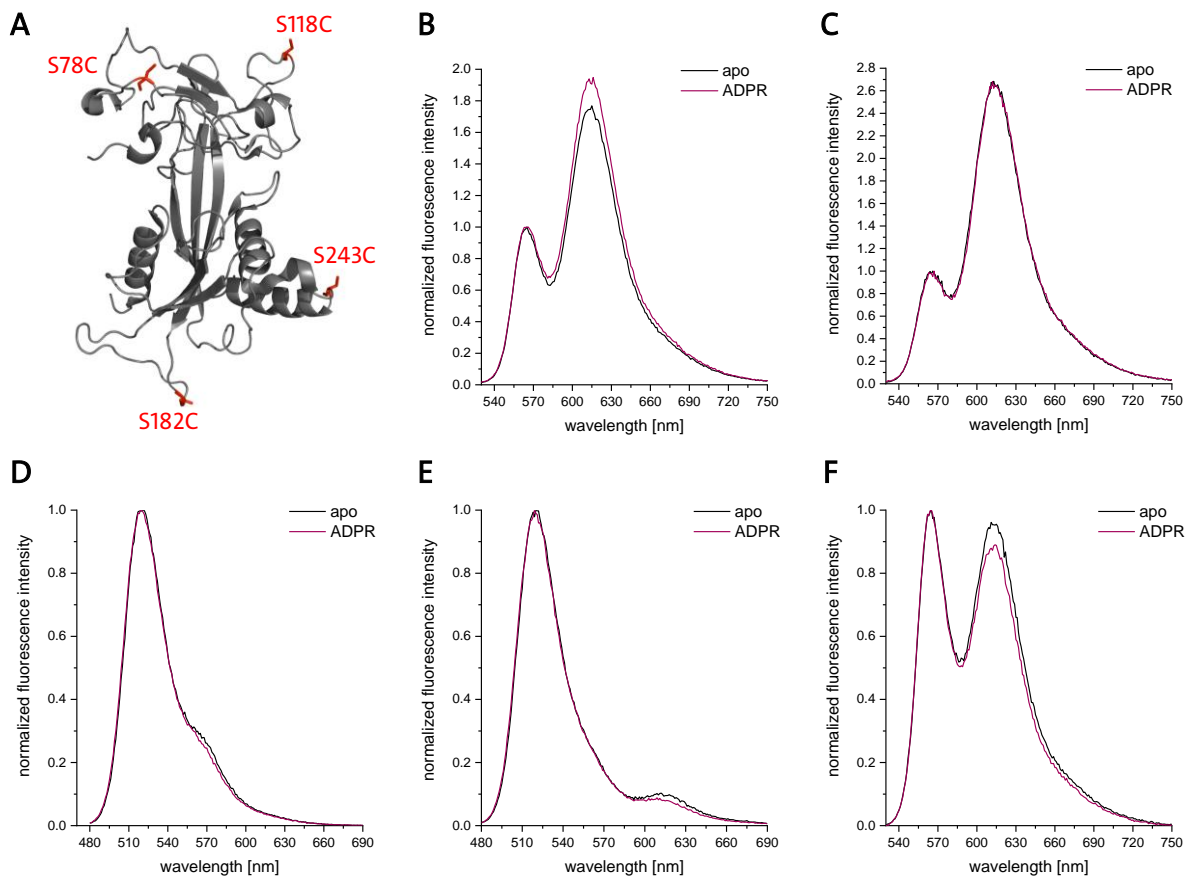


Figure 3.28: Normalized fluorescence spectra for all Alexa Fluor labelled NUDT9trC variations. (A) Crystal structure of NUDT9trC with highlighted serine residues chosen for mutation to cysteine. (B) Cys78 and Cys182 labelled with Alexa Fluor 555 and 594 (r_0 47 nm) show high FRET and changes upon ADPR binding. (C) Cys78 and Cys243 labelled with Alexa Fluor 555 and 594 (r_0 47 nm) show high FRET but no changes upon ADPR binding. (D) Cys118 and Cys182 labelled with Alexa Fluor 488 and 546 (r_0 64 nm) show no FRET but slight changes upon ADPR binding. (E) Cys118 and Cys182 labelled with Alexa Fluor 488 and 594 (r_0 60 nm) show no FRET but slight changes upon ADPR binding. (F) Cys118 and Cys182 labelled with Alexa Fluor 555 and 594 (r_0 47 nm) show FRET and changes upon ADPR binding. Spectra of single measurements performed at 20 °C are shown.

All three NUDT9trC variants labelled with Alexa Fluor 555 and Alexa Fluor 594 showed high FRET (Figure 3.28B/C/F). In contrast, the Cys118 to Cys182 NUDT9 variant labelled to longer distance FRET pairs, Alexa Fluor 488 to Alexa Fluor 546 or 594, show no FRET (Figure 3.28D/E); their small acceptor peaks arise most likely due to the leaky excitation. The changes detected upon ADPR binding exhibit high variations for all sensors (Table 3-9), but a promising candidate is the Cys78 to Cys182 NUDT9trC labelled with Alexa Fluor 555 and Alexa Fluor 594 with a ratio change of 11.9 ± 4.0 %, this sensor shows strong FRET. Despite the high standard deviation of the values, the candidate Cys118 to Cys182

3 ANALYSIS OF LIGAND-BINDING AND RESULTING CONFORMATIONAL CHANGES IN PYROPHOSPHATASE NUDT9

labelled with Alexa Fluor 555 and Alexa Fluor 594 is also promising, because it shows an even acceptor to donor ratio.

Table 3-9: Summary of FRET results for Alexa Fluor labelled NUDT9trC. Acceptor to donor ratios for the apo protein and the ADPR complex are compared and the relative change is calculated. Average values and standard deviation derive from one to three independent experiments.

Cysteine pair	Alexa Fluor pair	Ratio A / D apo	Ratio A / D 250 μ M ADPR	Δ Ratio [%]
C78 + C182	555 + 594	2.15 \pm 0.53	2.42 \pm 0.68	11.9 \pm 4.0
C78 + C243	555 + 594	2.62 \pm 0.09	2.71 \pm 0.01	3.4 \pm 2.9
C118 + C182	488 + 546	0.25	0.22	14.4
	488 + 594	0.13 \pm 0.04	0.12 \pm 0.05	9.6 \pm 9.9
	555 + 594	0.90 \pm 0.09	0.85 \pm 0.10	5.7 \pm 3.9

In conclusion, a FRET sensor of Alexa Fluor-labelled NUDT9trC seems feasible, but further optimizations are necessary to clearly detected FRET changes upon ADPR binding.

3.3 Discussion

3.3.1 2'-deoxy-ADPR is a novel ligand of the ADPR pyrophosphatase NUDT9

Among all NUDIX enzymes, NUDT9 shows an exceptional substrate specificity. Its activity towards more than fifty endogenous substrates was tested, encompassing various nucleotides and their derivatives but also common metabolic precursors and products. In remarkable contrast to other NUDIX enzymes, only ADPR was converted by NUDT9, no activity was measured towards all the other substrates (55). In this thesis, the ADPR derivative 2'-deoxy-ADPR was identified as novel substrate for NUDT9 and the binding of the two ligands was characterized (section 3.2.2).

Previous studies report comparable v_{\max} values around 11 μ mol min⁻¹ mg⁻¹ (26, 68) but highly different K_M values for the ADPR hydrolysis ranging from 180 μ M to 0.7 μ M (3, 53–55). This might be explained by imprecise detection of inorganic phosphate after additional AMP degradation by alkaline phosphatase and imprecise calculation models.

Here, the nucleotides were directly detected, and similar K_M values were obtained for ADPR and 2'-deoxy-ADPR hydrolysis ($3.0 \pm 0.4 \mu\text{M}$ vs. $0.8 \pm 0.3 \mu\text{M}$). The calculated v_{max} for the ADPR hydrolysis of $42.3 \pm 1.5 \mu\text{mol min}^{-1} \text{mg}^{-1}$ is faster than the previously reported values. ADPR is preferred by NUDT9 as it is hydrolyzed twice as fast as 2'-deoxy-ADPR (Table 3-1).

The binding affinities of the two substrates were determined by ITC. Using Mg^{2+} as co-factor, the substrate hydrolysis by the wild type NUDT9 was too fast to detect binding. Since Mn^{2+} also facilitates NUDT9 activity (70), it was assumed that the ligands could bind to NUDT9 in the presence of other divalent metal ions but were not (entirely) converted. Indeed, the binding affinities for ADPR and 2'-deoxy-ADPR to wild type NUDT9 could be determined using Ca^{2+} . High-affinity binding was measured for both substrates (Figure 3.3). Neither the co-factor nor the E230I and I231L mutations in the NUDIX box affected the binding affinity as the K_D values were indistinguishable (Table 3-2, Table 3-3).

Comparable to Zn^{2+} , Cu^{2+} and Co^{2+} (70), no enzyme activity was measured using Ca^{2+} as co-factor (Figure 3.5). Less than 50 pmol AMP were generated out of 180 nmol ADPR within 5 min incubation at 37 °C. In *E.coli* ADPRase Mg^{2+} ions position and prime a water molecule and thereby facilitate the cleavage of the phosphodiester bond of ADPR (133). A similar mechanism was described for *E.coli* ADPR pyrophosphatase (53). Due to the different hydrodynamic radii of Ca^{2+} and Mg^{2+} (134, 135), an inaccurate positioning of involved side chains or facilitating water molecules might prevent the substrate hydrolysis by NUDT9 but does not affect the binding affinity.

3.3.2 ADPR and 2'-deoxy-ADPR bind to the identical binding site in NUDT9

Besides the higher turnover rate for ADPR (Table 3-1), slight differences were detected for ADPR and 2'-deoxy-ADPR binding to NUDT9. However, all K_D values (Table 3-2, Table 3-3) are similar and both substrates stabilize NUDT9 (Figure 3.7, Figure 3.10, Figure 3.15). Using BEST-TROSY NMR spectroscopy, remarkably similar spectra were acquired for NUDT9 in complex with ADPR and 2'-deoxy-ADPR (Figure 3.17B). Only six signals shift substantially, which was somehow expected due to the only difference in the 2'-position

of the two ligands. The shifting residues were assigned to Lys161, Arg164, and Asp218 which presumably interact with the primary ribose and the adenine of ADPR.

According to the crystal structure of NUDT9 in complex with ribose 5-phosphate and Mg^{2+} (pdb: 1QVJ), Asp172, Asp271, Arg273 and Tyr321 interact with ribose 5-phosphate (57). None of those residues shift in the 2'-deoxy-ADPR compared to ADPR spectrum (Figure 3.17B, Figure 3.18), indicating a similar positioning of the terminal ribose in the binding pocket.

The Glu230 was suggested as catalytic base that coordinates two Mg^{2+} ions in NUDT9 (57). Comparing the binding enthalpies of wild type NUDT9 to ADPR and 2'-deoxy-ADPR, the difference of approx. 1 kcal suggests an additional hydrogen bond for 2'-deoxy-ADPR (Table 3-2). Since this difference is not observed for the E260I F261L mutant (Table 3-3), those residues might contribute to a hydrogen bond in the wild type NUDT9.

According to the NUDT9 crystal structure, the Cys207 is located in a loop proximate to the designated binding pocket. This residue (assigned to ω_1 113.443/ ω_2 8.331, Figure 3.18) shows no differences in the ADPR/NUDT9- compared to 2'-deoxy-ADPR/NUDT9 complex (Figure 3.17B). Cys207 does not contribute to the ligand binding affinity; the ADPR binding affinity of the NUDT9trC RIL C207S mutant was measured and remained unchanged (Figure 3.26).

3.3.3 The NUDT9 E230I F231L mutant can bind but not hydrolyze ADPR and 2'-deoxy-ADPR

When Perraud *et al.* discovered the TRPM2 channel in 2001, they claimed a weak pyrophosphatase activity of its NUDT9H domain (3). NUDT9 and NUDT9H share 39 % sequence identity (3), but four crucial amino acids in the active site of the NUDIX boxes differ from each other, which ought to be responsible for the pyrophosphatase activity. To address this, mutants with substitutions of the NUDIX boxes of NUDT9 and TRPM2 were analyzed. The E230I F231L mutation in NUDT9 greatly reduced its hydrolysis activity (70), and the substitution of two residues in the NUDT9H-NUDIX box of the TRPM2 channel by the respective NUDT9 residues prevented the ADPR-dependent channel activation (3, 78). However, it was never independently shown, that the substitution mutants still bind ADPR. In this thesis, it was shown that the NUDT9 E230I F231L mutant

**3 ANALYSIS OF LIGAND-BINDING AND RESULTING CONFORMATIONAL CHANGES IN
PYROPHOSPHATASE NUDT9**

still binds but does not hydrolyze ADPR. Further, the binding affinities of wild type NUDT9 and the E230I F231L mutant are indistinguishable (Table 3-2, Table 3-3).

During evolution, the pyrophosphatase activity of the NUDT9H domain in TRPM2 was lost. The TRPM2 channel of sea anemone *Nemastostella vectensis* (*nvTRPM2*) has been found to be the evolutionary ancestor of all contemporary TRPM2 channels (88). *nvNUDT9H* and *hsNUDT9* comprise 49 % sequence identity; the NUDIX box of *nvNUDT9H* resembles more the *hsNUDT9* NUDIX box than those of *hsNUDT9H* (Figure 3.29, adapted from (127)). Co-expression of *nvTRPM2* that lacks its NUDT9H domain and *nvNUDT9H* or *hsNUDT9* confirmed the intact catalytic activity of *nvNUDT9H* (136). The catalytic activity of the *nvNUDT9H* domain prevents TRPM2 channel activation after H₂O₂ stimulation by accumulated ADPR concentrations (136).

```

hsNUDT9  SGKHILQFVAIKRKDCGEWAIPGGMVDPGEKISATLKREFGEEALNSLQ
hsTRPM2  SIKKMLEVLVVKLPLSEHWALPGGSREPGEMLPRKLKRILRQEHWPSF-
nvTRPM2  GGKKVLEFVAIQKDNQWAIPGGMVEPGQLVTQALKAEFGEEAMAKLN
      . * :*:.:..: .**:** *:*: : ** : :* ..

hsNUDT9  KTSAEKREIEEKLHLKLFSDHLVIYKGYVDDPRNTDNAWMETEAVNYHD
hsTRPM2  -----ENLLKCG-MEVYKGYMDDPRNTDNAWIETVAVSVHF
nvTRPM2  VSGEEKERIAKQIERLFQQGQ-EIYKGYVDDPRNTDNAWMETVAVNFHD
      . :. :*.**:*~*****:** ** . *

```

Figure 3.29: Multiple sequence alignment of *hsNUDT9*, the NUDT9H domain of *hsTRPM2* and *nvTRPM2* shows high sequence similarities but also important differences in the NUDIX box. The NUDIX box is shown in red with the active site in bold letters. Symbols (*,;,.) indicate the degree of conservation of individual residues. Adapted from (127).

3.3.4 NUDT9 undergoes substantial conformational changes upon substrate binding

In previous reports, the structure of NUDT9 was subdivided in two domains: a C-terminal core domain possessing the ADPR pyrophosphatase activity and a proteolytically labile N-terminal cap domain that enhances the ligand binding affinity of the core domain (70, 137). Two peaks in the thermal unfolding profile of the apo NUDT9 measured by nDSF (Figure 3.7A) indicate independent and sequential unfolding of the cap and the core domain of apo NUDT9. Ligand-binding induces conformational changes (Figure 3.17A) that result in a more compact (Figure 3.9) and thermally stabilized NUDT9 (Figure 3.7). Similarly, a more compact ligand-bound form with large movements of a single loop has

been described for *E.coli* ADPRase (133). A cycling between open and closed conformation that preserves substrate specificity was proposed (133).

Theoretical SAXS curves were calculated from the crystal structures of NUDT9. Interestingly, the calculated apo structure and the structure of NUDT9 in complex with ribose 5-phosphate and Mg^{2+} were identical (Figure 3.9). Further, the experimental SAXS data of NUDT9 in complex with ADPR matched the crystal structure-based curves indicating the more closed conformation of NUDT9 in the crystals (Figure 3.9B). This might explain the steric hindrances due to tight crystal packing that prevented ADPR soaking into NUDT9 crystals which was described before (57).

According to the NUDT9 crystal structures, the 15 C-terminal amino acids (Arg336 to Leu350) form a mainly unordered tail that sticks out of the protein (57). To judge the impact of the tail on the observed conformational changes, a C-terminally truncated NUDT9 version was created. SAXS measurements confirmed a reduced maximum particle dimension of the truncated NUDT9 in complex with its ligands compared to the apo protein (Figure 3.8, Figure 3.11). The sequential thermal unfolding of cap and core of the apo protein was less prominent for this construct but still present (Figure 3.7, Figure 3.10).

However, the function of the C-terminal tail remains unclear. One of the two cysteine residues in NUDT9 is localized in the tail which might be involved in intermolecular disulfide bridge formation. Although the monomer appears to be the predominant form, dimeric and even oligomeric NUDT9 were observed (this study, (57)). Using a reducing agent, the monomer is more prominent (this study, (57)). Even in the C-terminally truncated NUDT9 version, the dimer was still observed. This suggests a role of the C-terminal tail in oligomerization, but additional features likely contribute to it.

A regulatory function of the C-terminal tail is also feasible. In the NUDT9 crystal structure, the tail of the symmetry mate sits in the substrate binding pocket and thus might hamper ADPR binding (Figure 3.30). However, the crystallization of the C-terminally truncated NUDT9 in complex with ADPR was not successful (Figure 3.12).

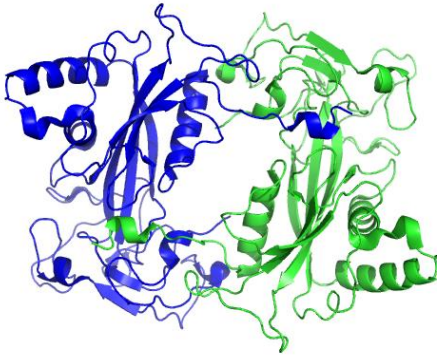


Figure 3.30: The terminal tail occupies the binding pocket of the symmetry mate in the crystal structure of NUDT9 (pdb: 1Q33).

3.3.5 NUDT9 can be developed into an ADPR FRET sensor

Using fluorescence energy transfer (FRET), the conformational changes in NUDT9 occurring upon ADPR binding could potentially be exploited to visualize ADPR in its signaling processes. Intramolecular FRET sensors detect subtle internal rearrangements of individual tertiary structure elements to change the relative distance and orientation of two fluorophores. The detected FRET changes are typically rather small compared to intermolecular FRET sensors where the two fluorophores are fused to different molecules and which depend on interactions of multiple domains (138). Prominent examples of second messenger FRET sensors are the cAMP sensor (reviewed in (139)) and the Ca^{2+} sensor based on Calmodulin and the M13 peptide (reviewed in (138)). During FRET sensor development, it is most important to achieve a change in distance r as large as possible and centered around R_0 as closely as possible (see section 6.2.11).

3.3.5.1 Genetically encoded FRET sensor

The coupling to fluorescent proteins that serve as donor and acceptor molecules is the most common principle of FRET sensors. The high stability of the fluorescent proteins and the potential to dispatch the sensor to individual cellular compartments in living cells are the most advantageous features of this FRET sensor class.

Originated from GFP, fluorescent proteins that span the whole spectrum of visible light were engineered (140). One of the first invented combinations is the CFP-YFP FRET pair. Although this FRET pair is well-established, it comprises several disadvantages like the

poor quantum yield of CFP or the pH sensitivity of YFP. mTFP1 originated from CFP and comprises excellent brightness and photostability (141). Similarly, mVenus originated from EYFP and comprises good pH stability due to its faster maturation (142). These two FRET pairs were chosen to develop a NUDT9-FRET sensor for ADPR (results section 3.2.6.1). All the designed sensors showed FRET, but none of them reported a FRET change upon ADPR binding (Table 3-4, Table 3-5, Table 3-6). Reducing the flexibility of the C terminus of NUDT9 did not improve the sensor.

Linker sequences can increase the distance between the fluorophores. Commonly used are various repeats of the peptide sequence GGSGGS which form flexible linkers (143). Alternatively, various repeats of the EAAAK peptide sequence form α -helices stabilized by salt bridges (131, 144). Since NUDT9 already exhibits high flexibility, a rigid linker was introduced but as many as five helix turns were insufficient to detect ADPR-dependent conformational changes.

Circularly permuted GFP, where entire β -sheets of the N- and C-terminus were interchanged and newly connected by short spacers, maintained its fluorescence but altered its orientation with respect to a fusion partner (145). This showed that changing the dipole-dipole orientations of the fluorescent proteins, can also result in changes in r_0 and therefore modulate the FRET efficiency. By this, the brightness and the dynamic range improved substantially for FRET sensors for Ras homolog family member A (RhoA) and the extracellular signal-regulated protein kinase (ERK) (146). Several circularly permuted variants of mTFP1 and mVenus were tested but none of them reported FRET changes upon ADPR-binding to NUDT9 (Table 3-6).

A large conformational flexibility of the relatively large fluorescent proteins rather than the FRET distance was assumed to prevent the detection of conformational changes in NUDT9.

3.3.5.2 Alexa Fluor labelled NUDT9

As an alternative to a genetically encoded sensor, a chemically labelled sensor was applied. Among all side chain modifications, cysteine labelling via maleimide click chemistry is the most prominent technique.

Four cysteine residues were introduced in positions that are on the surface of the NUDT9 protein. It was assumed that each cysteine pair was labelled with stoichiometric efficiency. However, next to the surface accessibility of the cysteines, several more factors need to be considered for the choice of labelling positions. First, labelling in loop regions is critical, as their flexibility might negatively contribute to the detection of the desired conformational changes upon ligand binding. Residues for labelling should rather be located at the beginning or end of secondary structure elements. As NUDT9 contains numerous loop regions, three out of the four chosen labelling positions are in loops (Figure 3.28).

Second, as tryptophan residues quench the fluorescence of Alexa Fluor dyes (147), a close proximity of the labelling position to them should be avoided. None of the chosen positions for labelling directly neighbors a tryptophan residue. But due to the flexibility of the loop regions it could not be excluded that the introduced cysteines at the positions 78, 118 or 182 could structurally be close to one of the nine tryptophans in NUDT9 or that their proximity alters within the conformational change upon substrate binding.

Third, neighboring glutamate or aspartate residues reduce the labelling efficiency of cysteine residues. The negative charges of these residues, especially glutamate, increase the pK_a of the thiol group in neighboring cysteines and by this impede the labelling kinetics of the maleimide click reaction (148). Only the introduced cysteine at position 182 directly neighbors an aspartate residue. Taken together, out of the four chosen labelling positions, only the cysteine introduced at position 243 fulfils all the criteria.

Considering these restrictions and not only serine but also alanine and glycine residues for mutation, only three additional amino acids appear suitable for cysteine introduction: Ser68, Ala101, and Ala106 – all of them are in the cap of NUDT9. However, the distances to the introduced Cys243 are even smaller than the tested combination with Cys118 (Table 3-7), which showed strong FRET without changes upon ADPR binding (Figure 3.28C).

Another option to design an ADPR FRET sensor would be the combination of a fused fluorescent protein to a termini of NUDT9 and a single introduced Alexa Fluor dye similar to the Caspase-3 FRET sensor (149). The chemical coupling of a single residue would erase

potential differences in coupling of two different dyes to two cysteines. The distance of the termini to a chemical dye coupled to position 243 or position 106 span approx. 50 nm. The combinations of mTFP1 and Alexa Fluor 488 or ECFP and Alexa Fluor 555 show FRET distances r_0 in this range of 58 nm and 54 nm, respectively.

In order to investigate ADPR in signaling processes, a chemically labelled FRET sensor has to be introduced into cells. Invasive techniques like microinjection or electroporation are feasible. Electroporation is used for in-cell NMR (150, 151), but the bioPORTER[®] protein delivery reagent was shown to be twice as effective as electroporation (152). The lipid mixture forms a protective vesicle that covers the proteins and allows the fusion with cell membranes and thus the immediate delivery into cells (153). Successful uptake by suspension (Jurkat T cells) and adherent cells (HeLa cells) was shown for the Caspase-3 FRET sensor (149).

Especially in cells, corrections are required for proper use of FRET measurements to characterize molecular interactions. Important to consider are corrections regarding spectral cross talk, the fact that each of the measured fluorescence intensities consists of both FRET and non-FRET components and the individual fluorophore concentrations (154).

In summary, a general proof of the principle of a FRET sensor for ADPR was achieved, which is a starting point for further development.

4 Calmodulin binding to and regulation of TRPM2

4.1 Abstract

The TRPM2 channel is a key player in various biochemical processes and its regulation by its ligands ADPR and 2'-deoxy-ADPR as well as Ca²⁺ and especially Calmodulin is very complex and still not fully understood. In this thesis, two novel Calmodulin binding motifs in TRPM2 were identified. The first one is located at the end of the TRP-helix two in vicinity to the transmembrane section of the channel. It binds apo Calmodulin as well as Ca²⁺-Calmodulin in a so far unrevealed binding mode. The second one is located in the NUDT9H domain, which is indispensable for TRPM2 activation. Using isolated NUDT9H and Ca²⁺-Calmodulin, a complex formation of partially unfolded proteins occurred at temperatures >35 °C and resulted in a thermal stabilization of the NUDT9H domain. Patch clamp experiments of mutated full-length TRPM2 demonstrated an impact of this novel Calmodulin binding site in NUDT9H on the temperature-dependent activation by ADPR and a comprehensive effect on the activation by the superagonist 2'-deoxy-ADPR.

4.2 Results

The detection of Calmodulin binding sites using bioinformatic tools is demanding because no specific consensus sequence exists. Only general features are defined: Calmodulin binding sites possess hydrophobic anchor residues which are flanked by positively charged residues. The anchor residues are interspaced by 10, 14 or 16 residues, typical patterns are e.g. 1-10 or 1-8-14 spacings. Using this information, the Calmodulin target protein search tool (<http://calcium.uhnres.utoronto.ca/ctdb/ctdb/sequence.html>) supports the detection of Calmodulin binding sites in proteins.

4.2.1 Identification and characterization of two novel Calmodulin binding sites in addition to the established IQ-like motif in MHR1/2

Tong *et al.* had found a Calmodulin binding site in the MHR1/2 domain of TRPM2 that is indispensable for TRPM2 gating by ADPR (108). In addition to this IQ-like motif (Figure 4.1, blue, Ile406-Leu416), two new potential Calmodulin binding motifs were identified

in TRPM2 in this thesis. The first one is located close to the TRPM2 transmembrane section at the end of the exposed TRP-helix two (Figure 4.1, purple, Leu1090-Ala1103). The second one is located in a loop region in the C-terminal NUDT9H domain (Figure 4.1, orange, Trp1355-Ile1368).

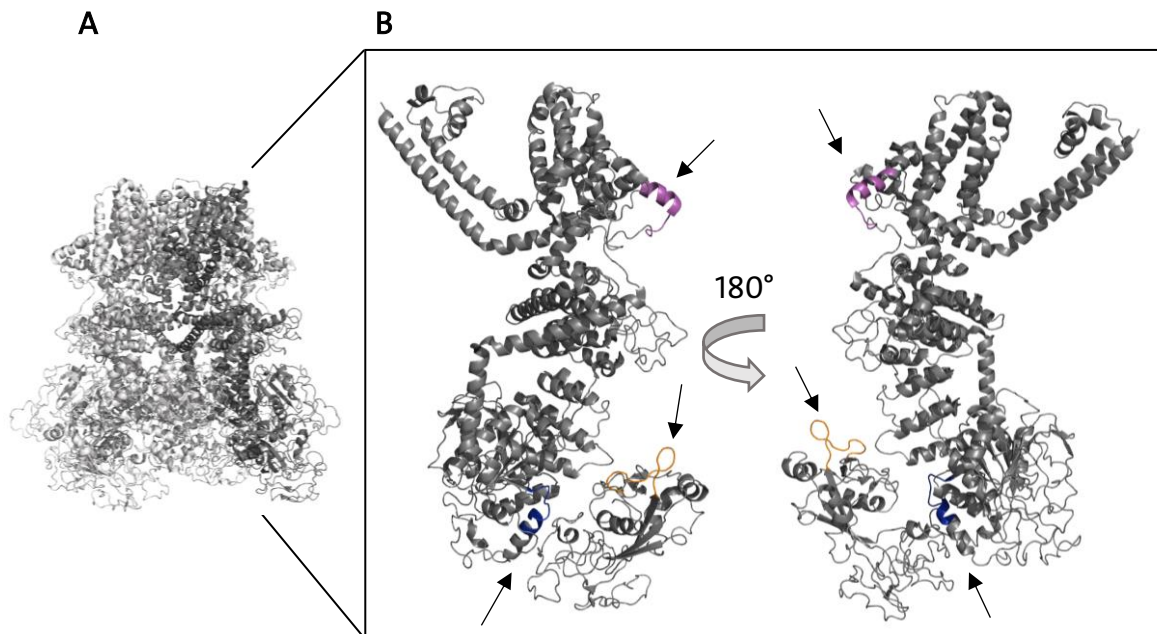


Figure 4.1: Identification of potential Calmodulin binding sites in TRPM2. (A) Crystal structure of human TRPM2 in the apo state (pdb: 6MIX). The four monomers are colored in blue, pink, yellow and green. (B) Zoom of one subunit of TRPM2 with highlighted potential Calmodulin binding sites (indicated by arrows). The known IQ-like motif in the MHR1/2 domain (blue) is located at the interface to the NUDT9H domain. A new potential Calmodulin binding site is in the NUDT9H domain (orange). A third potential Calmodulin binding site (pink) is located close to the transmembrane region of TRPM2.

Peptides of the Calmodulin binding motifs were synthesized (GL Biochem, Shanghai, China); all peptide names were derived from the first and last amino acid and the total number of peptide amino acids (Table 4-1).

4 CALMODULIN BINDING TO AND REGULATION OF TRPM2

Table 4-1: List of peptides of Calmodulin binding motifs in TRPM2 used for binding assays. Potential anchor residues mutated to alanine are underlined.

hTRPM2	Synthesized peptide	name
Ile406 – Leu416	RIVEWTKKIQDIVRRRQLLTVFREGK	RK26
	RIVEWTKKAQDIVRRRQ <u>ALT</u> VAREGK	mRK26
Leu1090 – Ala1103	LSHLQLFIKR <u>V</u> LKTPAKRHKQLK	LK24
	LSHLQLFIKR <u>V</u> LKTPAK	LK18
	LSHA <u>Q</u> LFIKRA <u>V</u> A <u>K</u> TPAK	mLK18
	LSHLQLFIKR <u>V</u> LKTPAKRHKQLKNKLEK	LK29
Trp1355 – Ile1368	VTHWRRNEDGAICRKS <u>I</u> KKMLEVEL	VL24
	VTH <u>A</u> RRNEDGAICRKS <u>A</u> KKMLEVEL	mVL24

First, the binding affinity of the IQ-like motif (peptide RK26, RIVEWTKKIQDIVRRRQLLTVFREGK) to Ca²⁺-Calmodulin was determined (Figure 4.2).

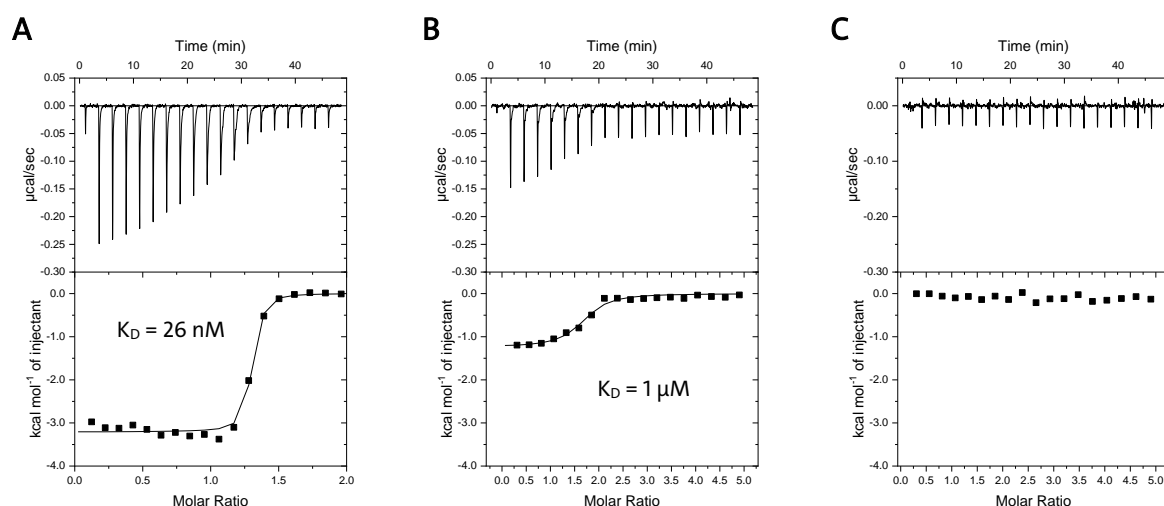


Figure 4.2: The RK26 peptide binds Ca²⁺-Calmodulin with nanomolar affinity but not apo Calmodulin. (A) 500 μM RK26 was titrated into 20 μM Ca²⁺-Calmodulin in the presence of 5 mM Ca²⁺ and showed an exothermic ITC binding pattern. (B) The mutated RK26 peptide (anchor residues with 1-10-14 are mutated to alanine) binds Ca²⁺-Calmodulin with greatly reduced affinity. (C) Apo Calmodulin (20 μM) does not bind RK26 (500 μM). ITC measurements were performed at 20 °C and data were fitted using a single binding site model.

The RK26 peptide showed a characteristic exothermic ITC pattern (Figure 4.2A) and the binding affinity for the IQ-like Calmodulin binding motif in TRPM2 to Ca²⁺-Calmodulin was determined to 27 ± 5 nM (n = 4 measurements). Mutation of the hydrophobic anchor

4 CALMODULIN BINDING TO AND REGULATION OF TRPM2

residues with 1-10-14 spacing (corresponding to Ile406, Leu415 and Phe418 in TRPM2, Table 4-1) reduced the binding affinity more than 50-fold to $1.5 \pm 0.8 \mu\text{M}$ ($n = 2$ measurements) (Figure 4.2B). No binding was measured to apo Calmodulin (Figure 4.2C). The first novel potential Calmodulin binding motif identified in this thesis (Figure 4.1) is represented by the peptide LK24 (LSHLQLFIKRVVLKTPAKRHKQLK) and showed a completely different binding pattern (Figure 4.3). Additional peptides with C-terminally shifted domain borders were also investigated: the shortened LK18 (LSHLQLFIKRVVLKTPAK) and the longer LK29 (LSHLQLFIKRVVLKTPAKRHKQLKNKLEK).

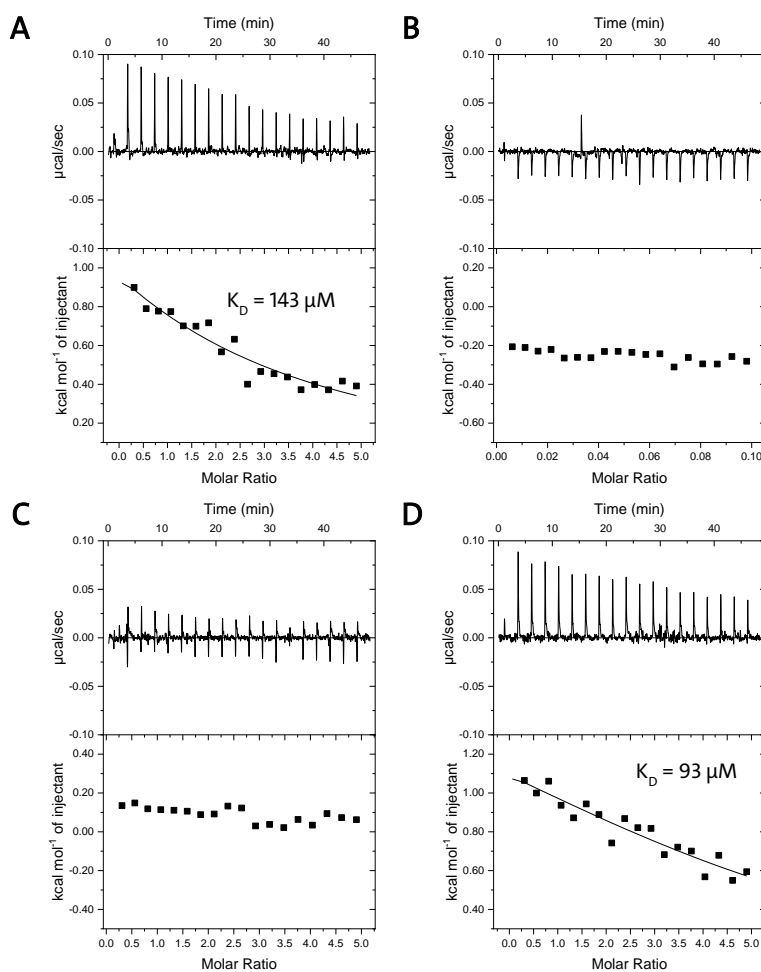


Figure 4.3: The LK24 peptide and the longer LK29 bind apo Calmodulin but the shorter LK18 does not. (A) 500 μM LK24 titrated in 20 μM apo Calmodulin show endothermic binding with a K_D of 143 μM . (B) Titration of 500 μM LK24 into buffer show typical heat of dilution. (C) 500 μM LK18 titrated in 20 μM apo Calmodulin show no binding. (D) 500 μM LK29 titrated in 20 μM apo Calmodulin show endothermic binding with a K_D of 93 μM . All measurements were performed at 20 $^{\circ}\text{C}$ and data were fitted using a one site binding model.

4 CALMODULIN BINDING TO AND REGULATION OF TRPM2

Titration of LK24 into apo Calmodulin revealed endothermic ITC signals and the K_D was calculated to 143 μM (Figure 4.3A). The control titration of LK24 peptide into buffer showed no signal except the typical heat of dilution (Figure 4.3B). The shorter peptide LK18 does not bind to apo Calmodulin but the longer LK29 binds with a slightly increased affinity of 93 μM (Figure 4.3C+D).

Next, the binding to Ca^{2+} -Calmodulin was analyzed. The standard set up titration of 500 μM LK18 peptide to 20 μM Calmodulin revealed a biphasic binding pattern (Figure 4.4A). The first injections showed endothermic signals that reversed to exothermic after several more injections. This unconventional ITC binding pattern indicates that multiple binding events take place, but a fitting failed. The mutation of the hydrophobic anchor residues with 1-8-10 spacing (Leu1090, Val1097 and Leu1099 in TRPM2; peptide mLK18) preserves the endothermic binding but not the exothermic; the ITC curve resembles the Ca^{2+} -free measurements and a K_D of 6 μM was calculated (Figure 4.4B).

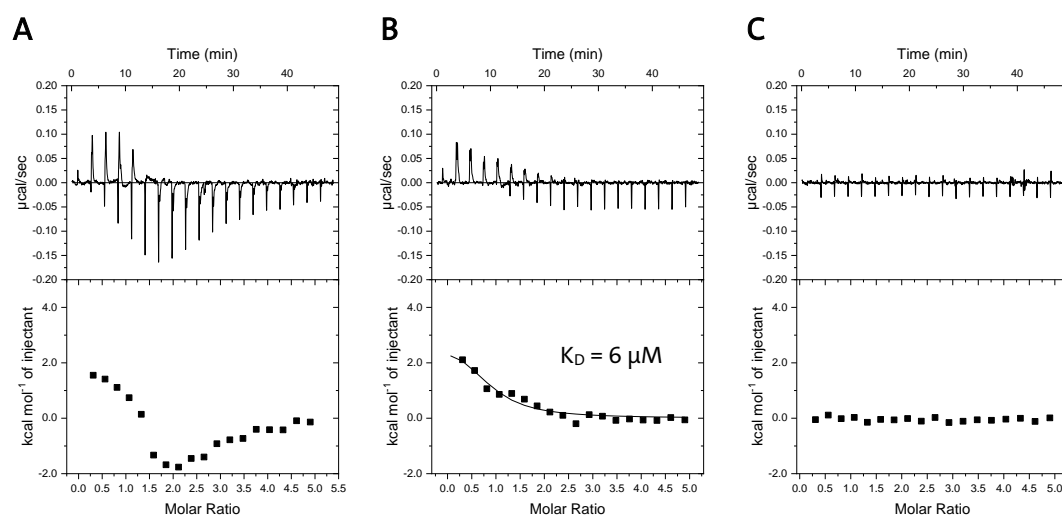


Figure 4.4: LK18 binds Ca^{2+} -Calmodulin and shows a biphasic binding pattern. (A) 500 μM LK18 were titrated to 20 μM Ca^{2+} -Calmodulin starting with an endothermic binding that is reversed to exothermic after several injections. (B) Titration of 500 μM mutated LK18 (anchor residues with 1-8-10 spacing were mutated to alanine) to 20 μM Ca^{2+} -Calmodulin reveal only endothermic binding with a K_D of 6 μM . (C) Titration of 500 μM mLK18 in buffer show no binding. All measurements were performed at 20 $^{\circ}\text{C}$ and data were fitted using a one site binding model.

Comparable to LK18, titration of LK24 or LK29 to Ca^{2+} -Calmodulin revealed unconventional ITC binding patterns (Figure 4.5). Fitting of the binding curve for LK24 or

4 CALMODULIN BINDING TO AND REGULATION OF TRPM2

LK29 binding to Ca^{2+} -Calmodulin failed (Figure 4.5A/D). The comparison of the LK24 and LK29 show less evident exothermic signals for the longer peptide (Figure 4.5A/D).

To resolve this unconventional binding pattern, the experimental setup was inverted and Ca^{2+} -Calmodulin was titrated into LK24. Several binding events were measured again, the curve fitting was not successful (Figure 4.5C).

Taken together, the novel potential Calmodulin binding site located in proximity to the transmembrane section of TRPM2 binds apo Calmodulin as well as Ca^{2+} -Calmodulin but the binding mode could not be deciphered.

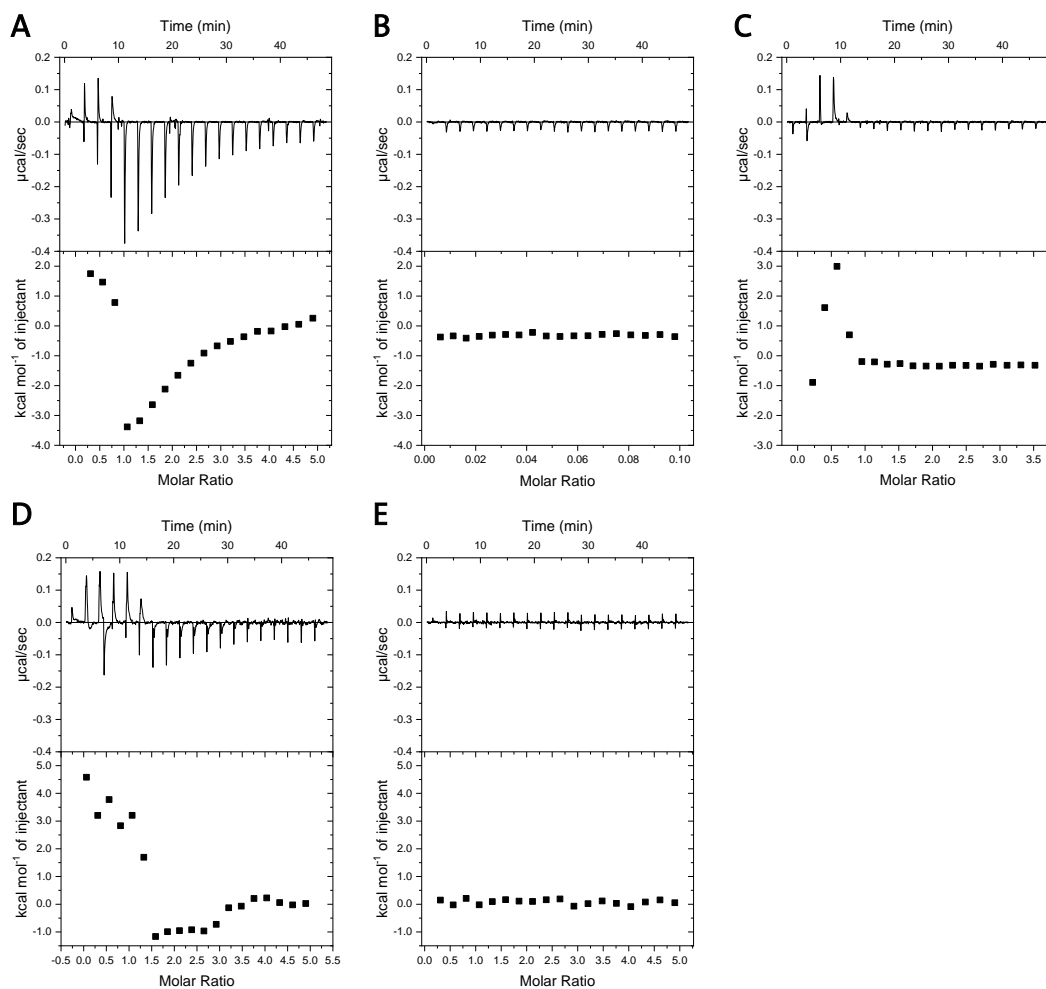


Figure 4.5: Binding of LK24 and LK29 to Ca^{2+} -Calmodulin indicates several binding events as measured by ITC. (A) Titration of 500 μM LK24 to 20 μM Ca^{2+} -Calmodulin reveals a biphasic binding pattern. (B) Titration of 500 μM LK24 in buffer showed only heat of dilution. (C) Titration of 359 μM Ca^{2+} -Calmodulin to 20 μM LK24 reveals a binding curve with up to three binding events. (D) Titration of 500 μM LK29 to 20 μM Ca^{2+} -Calmodulin reveals a triphasic binding pattern. (E) Titration of 500 μM LK29 in buffer showed only heat of dilution. All measurements were performed at 20 $^{\circ}\text{C}$.

4 CALMODULIN BINDING TO AND REGULATION OF TRPM2

The second novel potential Calmodulin binding site in TRPM2 is located in the NUDT9H domain of TRPM2. The peptide VL24 (VTHWRRNEDGAICRKSIIKKMLEVL) comprises the binding sequence ranging from Trp1355 to Ile1368. ITC measurements revealed a characteristic exothermic binding pattern for Ca²⁺-Calmodulin (Figure 4.6A), a K_D of 110 ± 18 nM (n = 3 measurements) was calculated. Using the mutated VL24 peptide (mVL24), the anchor residues Trp1355 and Ile1368 were identified as this peptide showed no binding to Ca²⁺-Calmodulin (Figure 4.6B). In the absence of Ca²⁺, VL24 did not bind apo Calmodulin (Figure 4.6C).

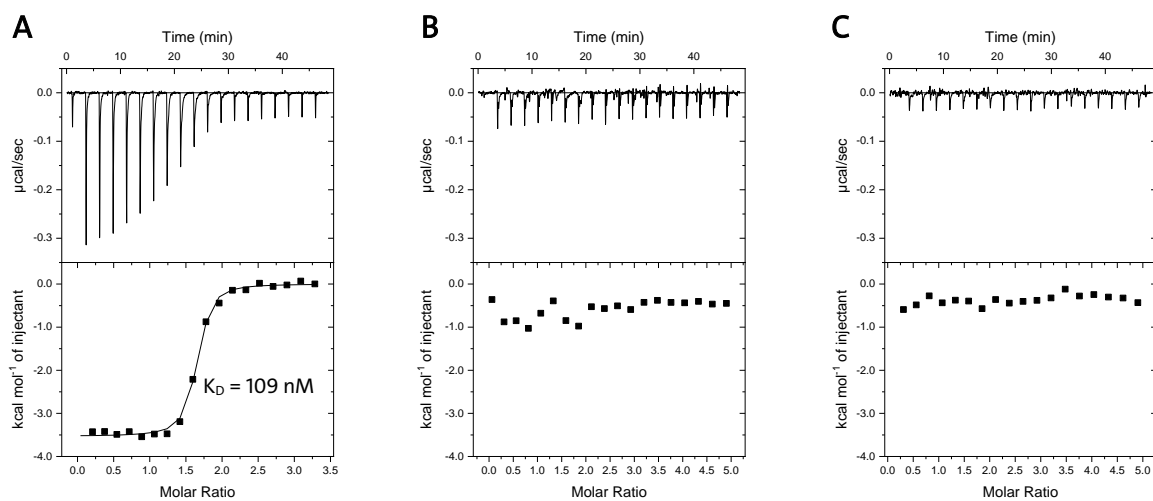


Figure 4.6: The VL24 peptide binds Ca²⁺-Calmodulin with nanomolar affinity but it does not bind apo Calmodulin. (A) 500 μM VL24 were titrated into 20 μM Ca²⁺-Calmodulin in the presence of 5 mM Ca²⁺ and showed an exothermic ITC binding pattern. (B) The titration of 500 μM mVL24 into 20 μM Ca²⁺-Calmodulin showed no binding and thus identified Trp1355 and Ile1368 as anchor residues. (C) 500 μM VL24 were titrated into 20 μM apo Calmodulin and showed no binding. ITC measurements were performed at 20 °C and data were fitted using a single binding site model.

In addition to the binding assays, the peptide Ca²⁺-Calmodulin complexes were purified by size exclusion chromatography (Figure 4.7). An additional peak in the chromatogram was only observed for the VL24/Ca²⁺-Calmodulin complex (Figure 4.7A) because the VL24 peptide is the only peptide containing a tryptophan residue. The SDS-PAGE of the main peak showed a band for Ca²⁺-Calmodulin and the respective peptide, no peptide band was visible for the Ca²⁺-Calmodulin control sample (Figure 4.7B).

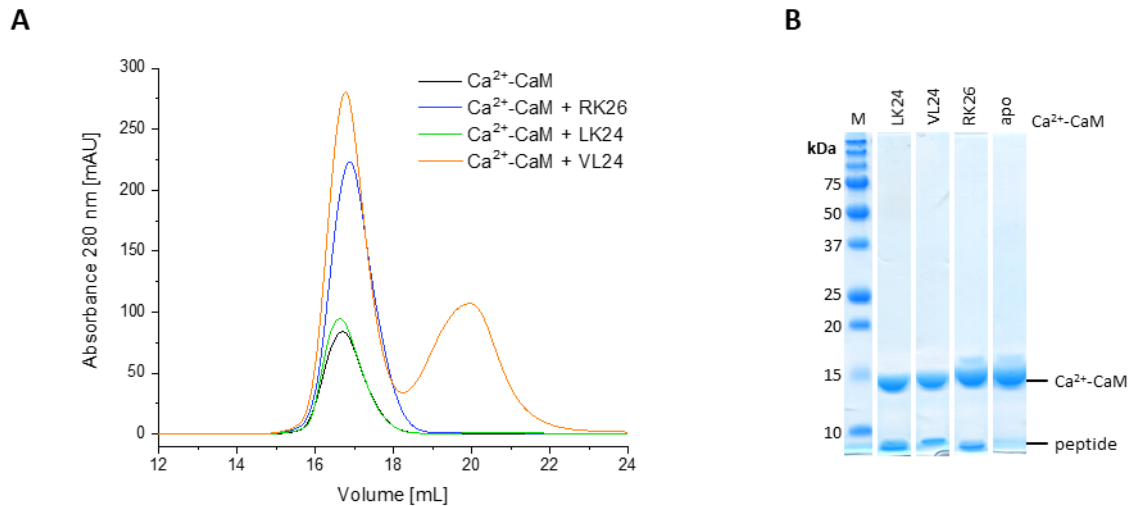


Figure 4.7: Purification of peptide Ca²⁺-Calmodulin complex by size exclusion chromatography. (A) Chromatography profiles of Ca²⁺-Calmodulin alone (black) and in complex with peptides RK26 (blue), LK24 (green) or VL24 (orange). (B) SDS-PAGE of the corresponding elution fraction shows bands for Ca²⁺-Calmodulin and the respective peptide.

The complex of Ca²⁺-Calmodulin and the respective peptides were subjected to extensive crystallization trials but no protein crystals were obtained.

4.2.2 Novel Calmodulin binding motif in NUDT9H contributes to temperature sensitivity of TRPM2

Since the NUDT9H domain is indispensable for TRPM2 activation, the novel potential Ca²⁺-Calmodulin binding site identified in this domain was investigated in detail. Using biophysical techniques, the interaction of the isolated NUDT9H domain and Ca²⁺-Calmodulin was studied. Further, the impact of the novel Calmodulin binding site in the TRPM2 channel was investigated using electrophysiological experiments.

4.2.2.1 BEST-TROSY NMR spectra confirm interaction of VL24 and Ca²⁺-Calmodulin

The NMR experiments were performed by Trevor J. Rutherford at the Laboratory of Molecular Biology in Cambridge, UK. BEST-TROSY-NMR spectra were acquired to assess the interaction of Ca²⁺-Calmodulin and the VL24 peptide on an amino acid level. The apo ¹⁵N-Calmodulin spectra compared to the complex with excess of the VL24 peptide

spectra showed massive changes with large perturbations and shifts or loss of signals (Figure 4.8) and thus confirmed the interaction of Ca^{2+} -Calmodulin and the VL24 peptide.

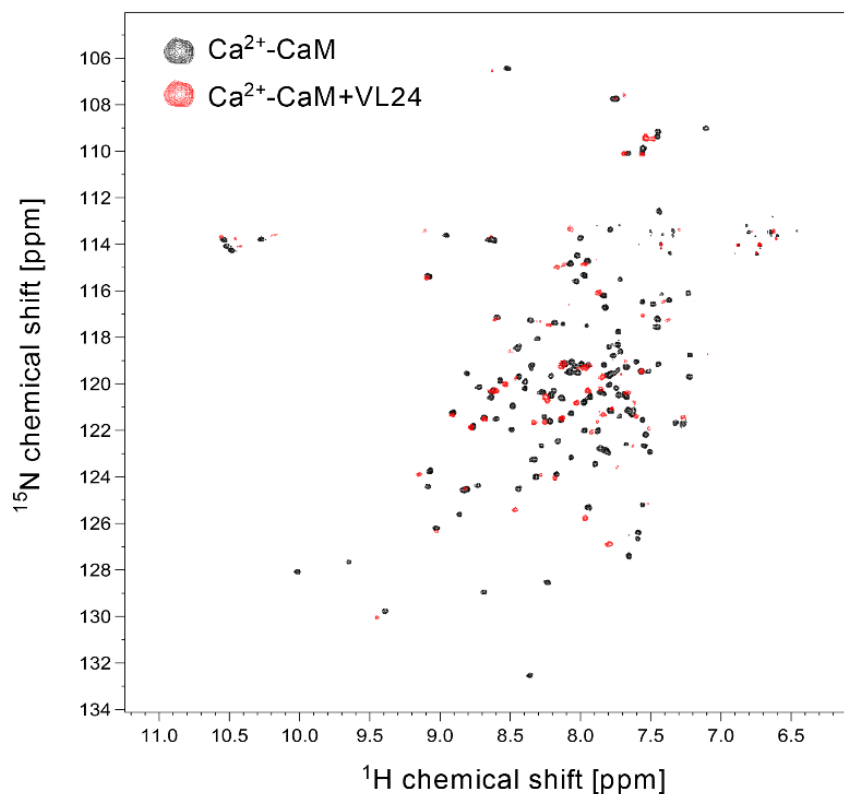


Figure 4.8: BEST-TROSY NMR spectra of apo Ca^{2+} -Calmodulin and in complex with the VL24 peptide. Substantial shifts of signals, large perturbations or loss of signals confirm different conformations of apo Ca^{2+} -Calmodulin (black) and in complex with the VL24 peptide (red). Spectra were acquired at 298 K.

4.2.2.2 The partially unfolded NUDT9H domain binds Ca^{2+} -Calmodulin

The NUDT9H domain (hTRPM2 residues Asp₁₂₃₆-Trp₁₅₀₃) was expressed in *E. coli* Rosetta 2 (DE3) cells as a GST-fusion protein with an internal His₆ tag followed by a TEV protease cleavage site. After Ni²⁺-IMAC purification, the tags were cleaved by TEV protease and the tags as well as the TEV protease were removed by a second round of Ni²⁺-IMAC. The isolated NUDT9H domain was subjected to size exclusion chromatography and the purity was assessed by SDS-PAGE (Figure 4.9). NUDT9H eluted as a single peak at 15.8 mL from a Superdex S200 10/300 GL column (Figure 4.9A). Consistent with the predicted mass of 31.0 kDa for the isolated NUDT9H domain, the SDS-PAGE of the respective

elution fractions showed a single band at approx. 30 kDa (Figure 4.9B). Mass spectrometry analysis confirmed the protein identity.

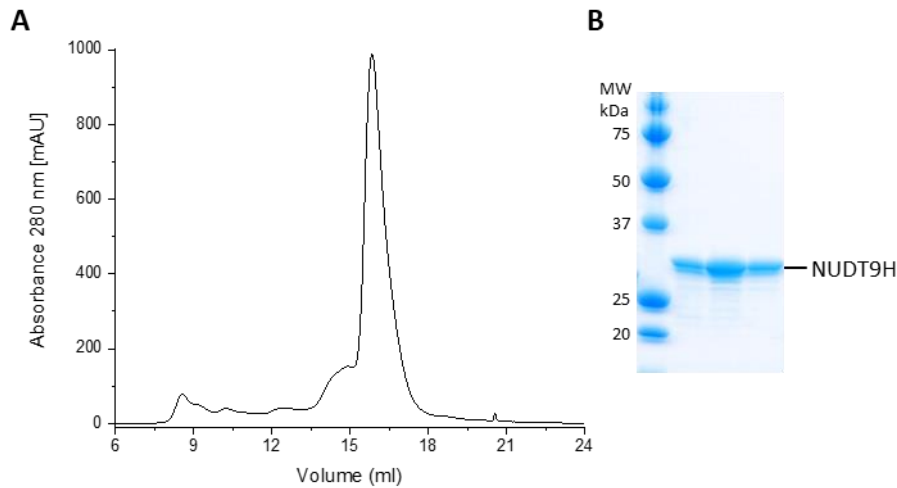


Figure 4.9: Purification of the NUDT9H domain of TRPM2. (A) The size exclusion chromatogram showed a single peak of monomeric NUDT9H. (B) The SDS-PAGE of the respective size exclusion fractions showed a single band at approx. 30 kDa.

Poor protein expression and a highly instable isolated NUDT9H domain were previously reported (11, 12). Consequently, after the successful purification of NUDT9H, the correct folding was analyzed by CD spectroscopy. The far-UV spectra indicated a regular secondary structure of the protein with predominantly α -helical folding (Figure 4.10) and therefore indicated properly folded protein.

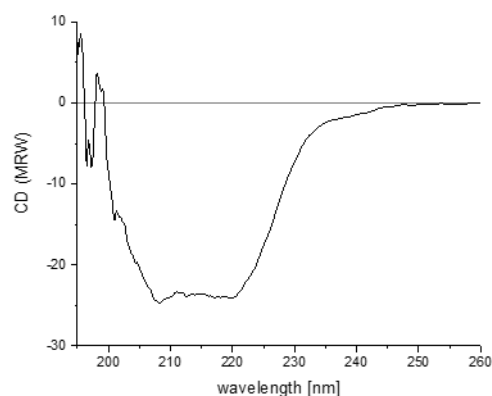


Figure 4.10: CD spectra of the isolated NUDT9H domain indicated correct protein folding. Minima at 222 nm and 208 nm indicate mainly α -helical secondary structure elements.

The potential interaction of NUDT9H and Ca²⁺-Calmodulin was addressed using various biophysical techniques. First, the proteins were incubated in a 1:1 ratio and then subjected to size exclusion chromatography. Chromatograms acquired on a Superdex S200 10/300 GL column of the single proteins and the complex were compared (Figure 4.11).

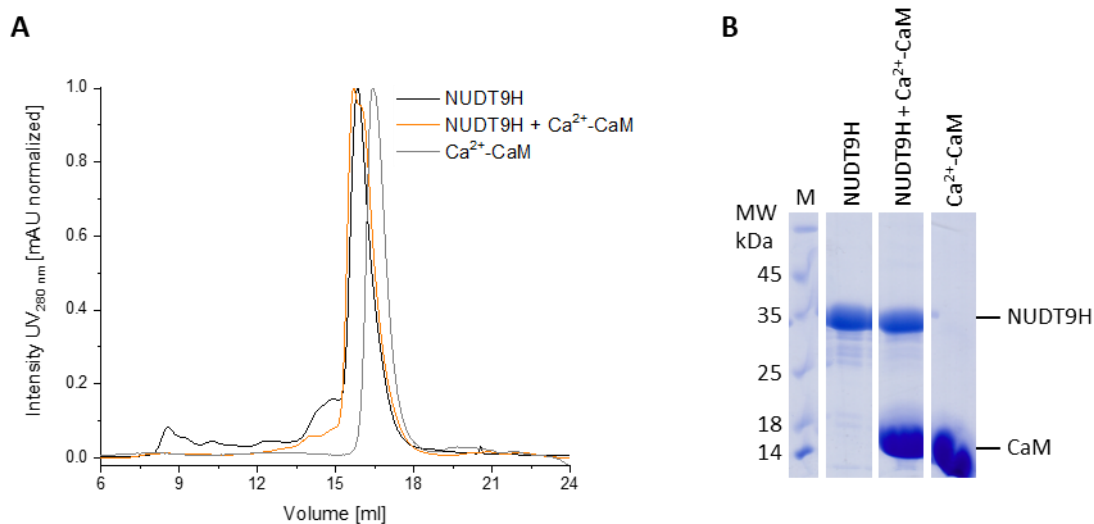


Figure 4.11: Size exclusion chromatography of the Ca²⁺-Calmodulin/NUDT9H complex. (A) The peak of the Ca²⁺-Calmodulin/NUDT9H complex (orange) is slightly larger compared to the single NUDT9H peak (black) and the Ca²⁺-Calmodulin peak (grey). (B) The SDS-PAGE of the main elution fractions shows two bands for the complex and single bands for the NUDT9H and Ca²⁺-Calmodulin samples.

The Ca²⁺-Calmodulin/NUDT9H complex eluted at 15.7 mL compared to the single NUDT9H at 15.8 mL; Ca²⁺-Calmodulin eluted at 16.4 mL (Figure 4.11A). Although the shift for the complex is very small, no peak shoulder indicating free Ca²⁺-Calmodulin appeared. The SDS-PAGE of the respective elution fractions showed massive bands of the single proteins in the complex (Figure 4.9B). However, the separation capacity of the used Superdex S200 10/300 GL column was insufficient to comprehensively separate the individual proteins and thus to prove the formation of a Ca²⁺-Calmodulin/NUDT9H complex.

Extensive crystallization trials of the potential Ca²⁺-Calmodulin/NUDT9H complex were set up, but no crystal structure of the complex was obtained. Several well-diffracting crystals were obtained using the complex set-up. However, none of them contained

NUDT9H, they all contained dimeric domain-swapped Calmodulin as shown by successful molecular replacement with apo Calmodulin from pdb: 1QX5 (155).

NUDT9H contains several buried as well as solvent exposed tryptophans, but Calmodulin does not contain any. This allowed the analysis of the tryptophans in NUDT9H in the presence and absence of Ca^{2+} -Calmodulin by differential scanning fluorimetry (nDSF) (Figure 4.12). This technique monitors the intrinsic tryptophan fluorescence while a protein unfolds in an applied thermal gradient. The fluorescence intensity at 330 nm reflects tryptophan residues in a hydrophobic environment (buried in the protein) whereas the fluorescence intensity at 350 nm reflects solvent exposed tryptophans on the protein surface.

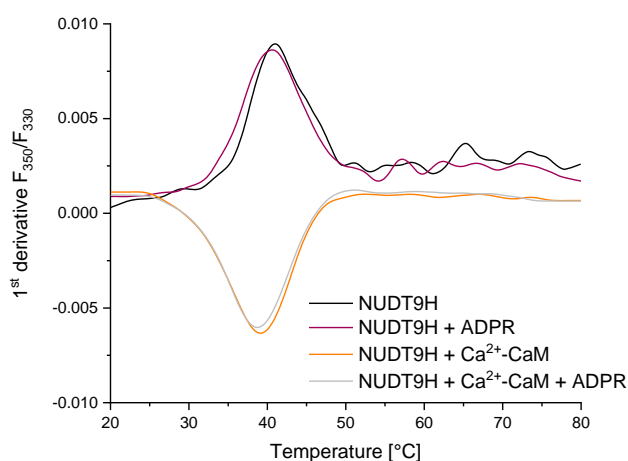


Figure 4.12: Ca^{2+} -Calmodulin binds partially unfolded NUDT9H as shown by nDSF. Apo NUDT9H (black) and NUDT9H in complex with ADPR (purple) shows an increase in F_{350}/F_{330} ratio during thermal unfolding because buried tryptophan residues become exposed. But the Ca^{2+} -Calmodulin/NUDT9H complex (orange; +ADPR in grey) shows decreased F_{350}/F_{330} ratio, probably because previously exposed tryptophan residues were buried.

Apo NUDT9H showed characteristic nDSF profiles with initially buried tryptophan residues that became solvent exposed upon thermal unfolding (Figure 4.12). This was reversed in the presence of Ca^{2+} -Calmodulin: The fluorescence intensity at 330 nm increased indicating more tryptophan residues in a hydrophobic environment (Figure 4.12). Interestingly, the complex of NUDT9H and Ca^{2+} -Calmodulin was formed at

elevated temperatures when the proteins unfold partly. The ligand ADPR had no impact (Figure 4.12).

Since NUDT9H contains twelve tryptophan residues, a control experiment using the VL24 peptide was performed (Figure 4.13). The tryptophan residue in the peptide (Trp1355 in TRPM2) was identified as one of the anchor residues for the Ca^{2+} -Calmodulin binding (Figure 4.6B). The peptide alone showed a fluorescence maximum at 350 nm implying the single tryptophan residue being solvent exposed. In contrast, the fluorescence maximum was observed at 330 nm in the presence of Ca^{2+} -Calmodulin indicating that the residue was covered by Ca^{2+} -Calmodulin (Figure 4.13). This supported the nDSF observations and proved the impact of the Trp1355 in the NUDT9H domain for Ca^{2+} -Calmodulin binding.

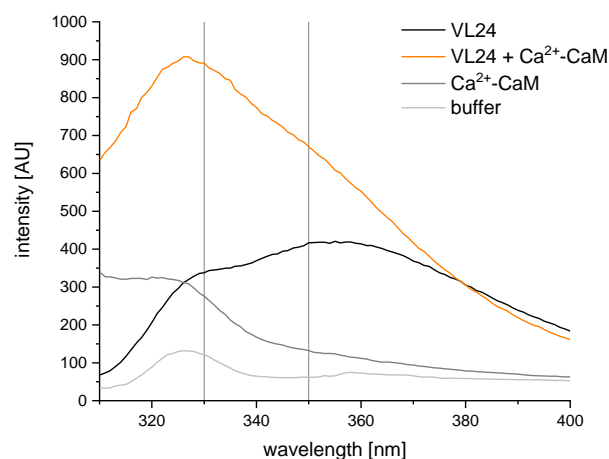


Figure 4.13: The tryptophan residue in the VL24 peptide is shielded in the complex with Ca^{2+} -Calmodulin. The tryptophan residue in the peptide VL24 is solvent exposed (black) but is buried by Ca^{2+} -Calmodulin (orange). Ca^{2+} -Calmodulin (dark grey) and the buffer (light grey) show a small peak at 325 nm.

Thermo-dynamic light scattering was performed to investigate a thermo-stabilizing effect of Ca^{2+} -Calmodulin on NUDT9H. In an applied thermal gradient, the hydrodynamic radius of a particle is measured which increases once particles aggregate. NUDT9H aggregated at 42 °C but the complex of NUDT9H and Ca^{2+} -Calmodulin was stabilized to 47 °C. Ca^{2+} -Calmodulin alone did not form aggregates up to 60 °C (Figure 4.14).

4 CALMODULIN BINDING TO AND REGULATION OF TRPM2

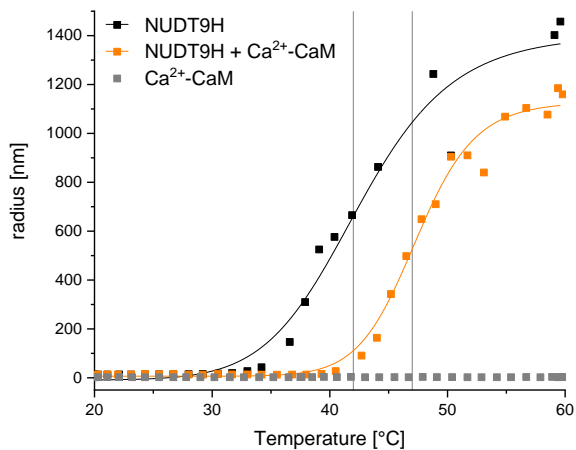


Figure 4.14: Ca²⁺-Calmodulin stabilizes NUDT9H at elevated temperatures. The NUDT9H domain alone aggregates at 42 °C (black) but is stabilized to 47 °C in the presence of Ca²⁺-Calmodulin (orange). Ca²⁺-Calmodulin alone does not aggregate up to 60 °C (grey).

To determine the binding affinity of NUDT9H and Ca²⁺-Calmodulin, ITC measurements were performed. Measurements at room temperature failed, no binding was detected. But taken previous nDSF and DLS results into consideration, ITC was performed at 35 °C and a binding affinity of Ca²⁺-Calmodulin to NUDT9H of 470 nM was determined (Figure 4.15).

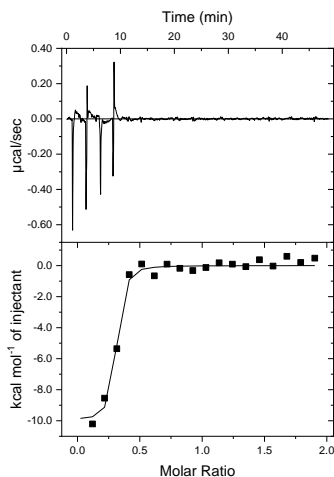


Figure 4.15: Ca²⁺-Calmodulin binds NUDT9H at 35 °C with nanomolar affinity as determined by ITC. 600 µM Ca²⁺-Calmodulin was titrated into 24 µM NUDT9H.

In summary, the partially unfolded NUDT9H domain and Ca²⁺-Calmodulin bind at temperatures >35 °C with nanomolar affinity, which leads to a thermal stabilization of NUDT9H.

4.2.2.3 Calmodulin binding to the NUDT9H domain affects the temperature-dependent activation of the TRPM2 channel

Next, the impact of the novel Calmodulin binding site on the activation of the full-length TRPM2 channel by ADPR and 2'-deoxy-ADPR was investigated. A channel mutant with the mutated anchor residues Trp1355A and Ile1368A was generated. Using the pIRES2-EGFP vector, TRPM2 wild type and the mutant were transiently expressed in HEK293 cells.

A comparable expression of the two TRPM2 variants in plasma membrane were checked by a surface biotinylation assay with subsequent western blot analysis (Figure 4.16).

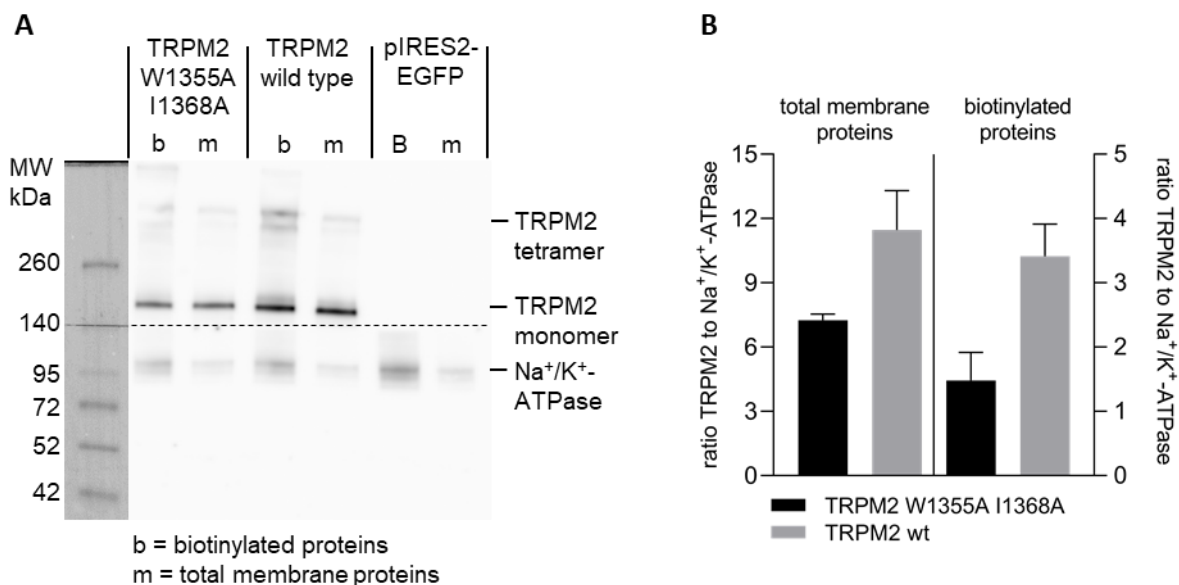


Figure 4.16: Comparison of the surface expression of TRPM2 wild type and the W1355A/I1368A mutant. (A) Detection of TRPM2 and Na⁺/K⁺-ATPase in total and biotinylated membrane proteins from HEK293 cell membranes after 48 h expression. (B) Densitometric analysis of TRPM2 (monomer and tetramer) to Na⁺/K⁺-ATPase ratio in total and biotinylated membrane proteins reveals a reduced expression of the TRPM2 W1355A I1368A mutant. Data from three independent experiments are represented as mean ± SEM.

The mutation of the hydrophobic residues Trp1355 and Ile1368 does not prevent the translocation of the TRPM2 channel to the plasma membrane (Figure 4.16). However,

densitometric analysis of the western blots revealed a reduced number of mutated TRPM2 channels (Figure 4.16B). Since the ratio of wild type and mutated TRPM2 in the total and the biotinylated membrane proteins are comparable, a general lower expression level for the mutant rather than retained channels in intracellular membranes was assumed.

Transfected HEK293 cells were identified by the additionally expressed EGFP and subsequently used for whole cell patch clamp measurements. Saturating concentrations of 100 μ M ADPR or 2'-deoxy-ADPR in the pipette solution activated the channel; a free Ca^{2+} -concentration of 200 nM was used. Currents of the wild type or mutated TRPM2 channel recorded at room temperature were compared to those recorded at 37 °C bath solution (Figure 4.17).

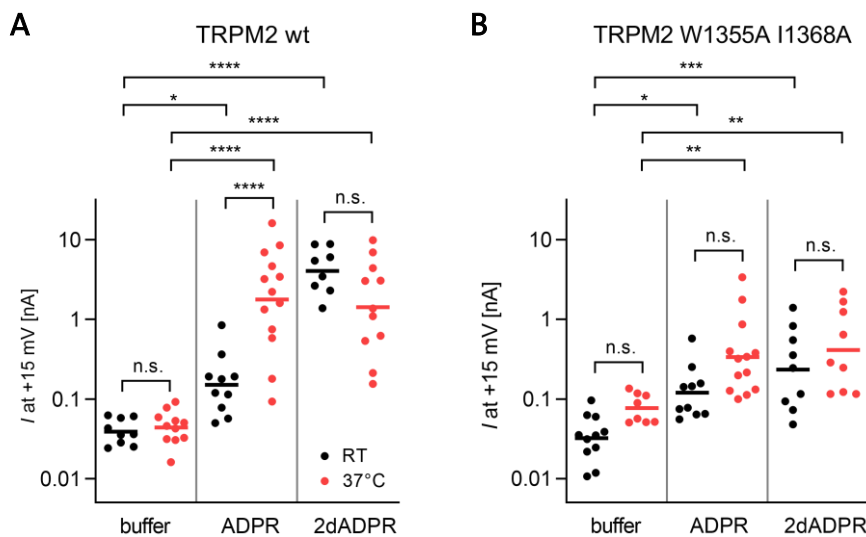


Figure 4.17: Calmodulin binding to the NUDT9H domain in TRPM2 influences its temperature-dependent activation by ADPR and 2'-deoxy-ADPR. (A) Activation of wild type TRPM2 measured at room temperature (RT, black) and 37 °C (red). Currents evoked by 100 μ M ADPR are significantly higher at 37 °C in the wild type TRPM2 channel. Currents evoked by 100 μ M 2'-deoxy-ADPR show no temperature-dependent effect. (B) Activation of TRPM2 W1355A I1368A measured at room temperature (black) and 37 °C (red). The channel was activated by the agonists (compared to the buffer control) but the temperature-dependent effect observed in the wild type channel disappeared. Data points reveal whole cell currents at +15 mV from individual cells (n = 8-13). The mean of the log-transformed data is indicated by the bar. One-way ANOVA and Bonferroni correction were used for statistical analyses of the log-transformed data. (*p < 0.05, **p < 0.01, ***p < 0.001, ****p < 0.0001).

The temperature difference alone had no effect on the activation of the TRPM2 channel variants (Figure 4.17, buffer controls). Currents evoked by ADPR were significantly

increased from 150 pA to 2.2 nA (median values) in the wild type TRPM2 channel at 37 °C (Figure 4.17A); this effect was abolished in the W1355A I1368A channel mutant (Figure 4.17B). As previously shown (176), currents elicited by 2'-deoxy-ADPR in the wild type TRPM2 were increased compared to ADPR currents (4.5 nA compared to 150 pA for ADPR, median values). Interestingly, the raised temperature had no additional effect on the activation by 2'-deoxy-ADPR (Figure 3.1A). However, currents elicited by 2'-deoxy-ADPR at room temperature and at 37 °C were both decreased in the W1355A I1368A channel mutant and showed comparable values to the ADPR elicited currents (Figure 4.17B). Taken together, Calmodulin binding to the NUDT9H domain in TRPM2 affects the temperature-dependent activation by ADPR and further indicates a comprehensive effect on the activation by 2'-deoxy-ADPR.

4.3 Discussion

4.3.1 High affinity binding of the known IQ-like binding site to Calmodulin

Various members of the TRP channel superfamily are regulated by Calmodulin. In 2005, Tong *et al.* discovered direct interaction of Calmodulin and TRPM2; they demonstrated strong binding to the N-terminus and weak binding to the C-terminus of TRPM2. Deletion of a N-terminal IQ-like motif greatly reduced the ADPR-dependent channel activation. They suggested a crucial positive feedback mechanism by binding of Calmodulin to the N-terminus in TRPM2 after the channel was partially activated by ADPR and Ca²⁺ (108). Using the peptide RK26, that includes the IQ-like binding motif, high-affinity binding of Ca²⁺-Calmodulin was confirmed (Figure 4.2). Mutation of the potential anchor residues Ile406, Leu415 and Phe419 to alanine reduced the affinity more than 50-fold to 1.5 μM but also suggested Val410 as additional anchor residue (Figure 4.2). The involvement of four anchor residues with 1-5-10-14 spacing reflects the observed tight binding.

This IQ-like motif is strictly conserved in mammalian TRPM2 channels and predominantly conserved in *dr*TRPM2. Interestingly, the binding site is located in the inner cavity of the bottom layer (Figure 4.18A) and almost inaccessible in all published TRPM2 structures as it is partially buried inside the MHR1/2 domain and is located at the

interface to the cap of the NUDT9H domain from the same monomer (85–87, 95). Interestingly, the section from Asp1165 to Gly1235 (70 amino acids) that connects the NUDT9H domain and the Rib helix is missing in all published structures. This missing stretch might face the IQ-like motif in the N-terminus. Substantial tertiary and quaternary conformational rearrangements transit the closed to the open state (97), which also decreases the distance between Asp1135 and Gly1235 from 36 nm to 28 nm (Figure 4.18B+C). Closer inspection of the amino acid sequence of the missing stretch revealed other possible Calmodulin binding sites (Figure 4.18D), which might allow a Calmodulin-dependent interaction of the IQ-like motif and the missing stretch.

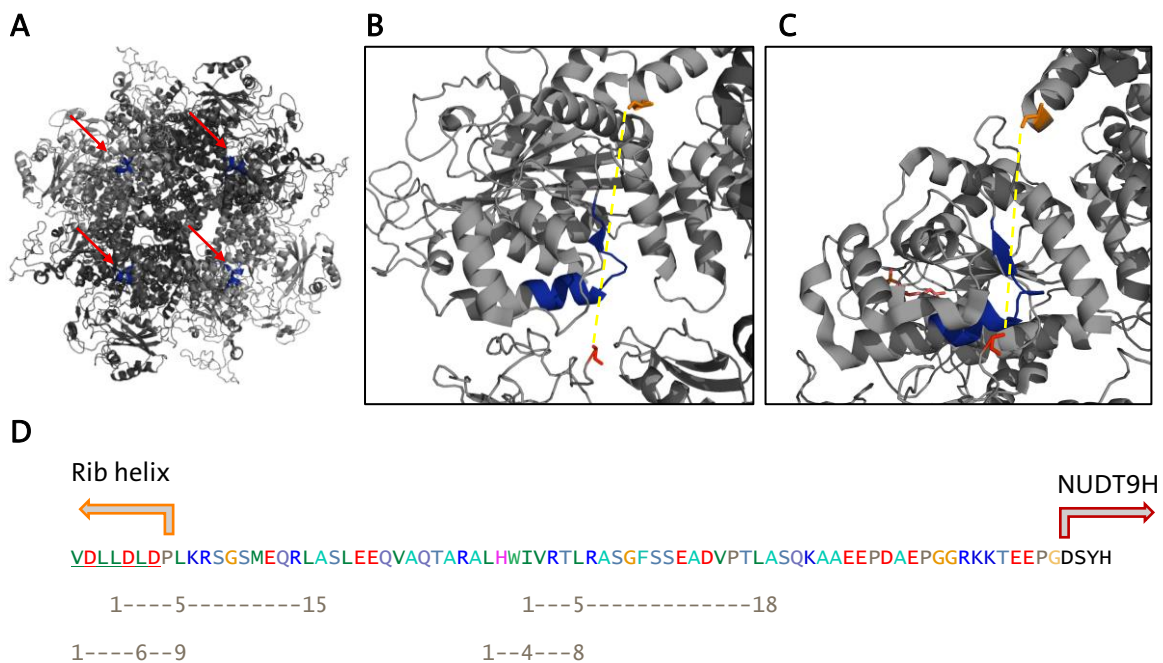


Figure 4.18: Localization of the IQ-like motif in TRPM2. (A) Bottom view on TRPM2 (pdb: 6PUO) with the IQ-like Calmodulin binding site (blue) highlighted in each monomer. (B+C) Missing stretch of 70 amino acids from Asp1165 (orange, sticks representation) at the end of the Rib helix to Gly1235 (red, sticks representation) at the beginning of the NUDT9H domain might face the IQ-like motif in the N-terminus. (B) Distance between Asp1165 and Gly1235 in apo TRPM2 (pdb: 6PUO) spans 36 nm (indicated by yellow dashed line). (C) Massive conformational rearrangements in TRPM2 upon ADPR binding (pdb: 6PUS) decrease the distance between Asp1165 and Gly1235 to 28 nm (indicated by yellow dashed line). (D) Amino acid sequence of the stretch connecting the Rib helix and the NUDT9H domain. Potential Calmodulin binding sites are indicated (grey numbers) by their spacing of large hydrophobic residues.

Nevertheless, the structure of *dr*TRPM2 in complex with ADPR and Ca^{2+} (pdb: 6DRJ) represents the only veritable open conformation so far as it is the only one with a

sufficient large pore diameter to permeate Ca^{2+} ions (87). Conceivably not all conformations of TRPM2 were captured so far.

Taken together, it remains unknown how Calmodulin binds to the N-terminal IQ-like motif in the physiological context and if it binds to all conformations of TRPM2.

4.3.2 A novel Calmodulin binding site in the TRP domain of TRPM2 might be involved in Ca^{2+} -dependent channel regulation

As Tong *et al.* (108) already indicated, two more Calmodulin binding sites were discovered in the C-terminus of TRPM2. The localization of a second novel potential Calmodulin binding site starts at the end of the conserved TRP helix two and proceeds to the following loop. The TRP helices are of great importance as they undergo large movements in the channel gating process of TRPM2 and thereby conduct signals from the cytosolic domains to the pore (97). Further, the TRP helix one is located right below a Ca^{2+} binding site at the cytosolic end of the transmembrane helices three and four (85, 89). Mutation of the Ca^{2+} coordinating residues in *nvTRPM2* severely affected the channel activity due to a loss in Ca^{2+} sensitivity (89). Although parts of the novel potential Calmodulin binding site are likely located in the membrane, a regulatory role is feasible and would be in line with the observed Ca^{2+} -dependent as well as Ca^{2+} -independent binding of Calmodulin to the synthesized peptides (Figure 4.3 to Figure 4.5).

Among mammalian TRPM2 channels, the potential Calmodulin binding site is conserved but the amino acid sequence differs in *drTRPM2* and *nvTRPM2*. *nvTRPM2* is more Ca^{2+} permeable than *hsTRPM2* due to a larger pore diameter and a more negative pore surface (89). During evolution, a more complex Ca^{2+} -dependent channel regulation (in and near the pore as well as otherwise in the channel) might have been developed, which includes the additional potential Calmodulin binding site in mammalian TRPM2.

Comparing the structures of TRPM2, the TRP loop is not resolved in most of them. This might be due to the general flexibility of the loop or might hint to a potential stabilization by Calmodulin as it was shown for other TRP channels. In apo TRPC4, Calmodulin binding to a highly flexible loop in the rib helix decreased the overall flexibility of the channel and by this stabilized the closed state (156). The tetrameric

TRPC4 can bind up to four Calmodulin molecules, which also suggests a regulatory role of Calmodulin-binding (156). A Calmodulin-dependent channel stabilization as well as regulation was also described for TRPV5: Calmodulin binds to the very end of the C-terminus and stabilizes it (157). Calmodulin binds to a predicted binding site in TRPV5 (158) but also interacts with an additional binding site (157). Due to the different Ca^{2+} affinities of the N- and C-lobe of Calmodulin (C-lobe has a 6-fold higher Ca^{2+} binding affinity) (159), the C-lobe is constantly bound to the C-terminus of TRPV5, but the N-lobe only binds at high Ca^{2+} concentrations and thereby inactivates the channel (157). The unconventional binding pattern observed for the synthesized peptides from TRPM2 (Figure 4.3 to Figure 4.5) might reflect a mechanism that is similar to Calmodulin binding to TRPV5.

Nevertheless, to clarify the presence and relevance of this novel Calmodulin binding site in TRPM2, mutational as well as electrophysiological analyses in the context of full-length TRPM2 are indispensable.

4.3.3 Novel Calmodulin-binding motif in its NUDT9H domain contributes to temperature sensitivity of TRPM2

The second novel Calmodulin binding site is located in the P-loop region in the NUDT9H domain of TRPM2. In the context of the full-length TRPM2 channel, this loop is partially in the interface to the MHR1/2 domain of a neighboring subunit but still accessible from the outside of the channel. Interestingly, intersubunit interactions between the Calmodulin binding site and the Ca^{2+} binding EF-loop (D267-D278) in the MHR1/2 domain (107) occur in the closed conformation of TRPM2 (Figure 4.19A). In the ADPR/ Ca^{2+} -bound state, the interaction is disrupted as conformational rearrangements in the MHR1/2 domain move the EF-loop to the N-terminal ADPR binding site (Figure 4.19B). Due to the location in the ADPR bound state, the EF-loop might not only bind Ca^{2+} but also interact with ADPR and thus explain the synergy between the two agonists.

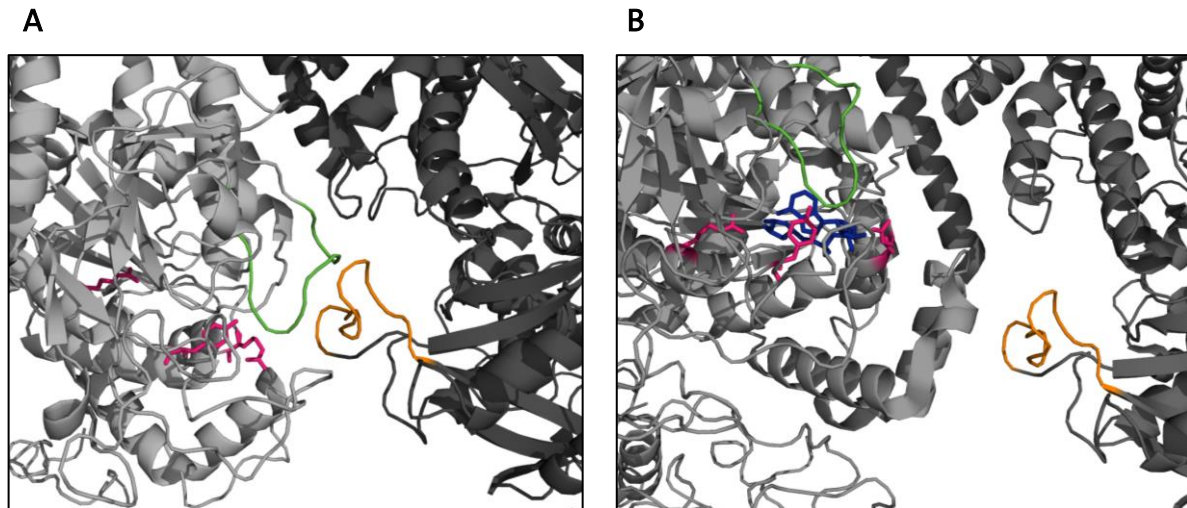


Figure 4.19: Calmodulin binding site in NUDT9H interacts with the EF-loop of the neighboring MHR1/2 in the closed TRPM2 conformation. (A) Interspatial interaction occurs between the Calmodulin binding site in NUDT9H and the EF-loop of MHR1/2 in the closed *hsTRPM2* (pdb: 6PUO). (B) Conformational changes in MHR1/2 occurring upon ADPR binding translocate the EF-loop to the ADPR binding site (pdb: 6PUS). Individual TRPM2 subunits are colored in light and dark grey. EF-hand loop is colored in green, the Calmodulin binding site in NUDT9H is colored in orange. ADPR is shown in sticks representation (blue) and important ADPR-interacting residues Y295, R302 and R358 (85) are shown in pink stick representation.

Ca^{2+} -dependent ion channel regulation can be achieved directly by Ca^{2+} binding and indirectly via Ca^{2+} -Calmodulin. Direct regulation via Ca^{2+} -binding close to the pore (85, 95) was supported as all Ca^{2+} -bound TRPM2 structures show densities for Ca^{2+} in the pore region (89, 101). However, no Ca^{2+} -bound structure of *hsTRPM2* without ADPR was determined so far, leaving the possibility for an indirect Ca^{2+} -regulation via Calmodulin as implied by the interaction of the EF-loop in the N-terminus and the Calmodulin binding site within the NUDT9H domain observed in the closed *hsTRPM2* conformation. Yet, it can only be speculated if Calmodulin provides Ca^{2+} or receives it from the EF-loop. Interestingly, the binding of 2'-deoxy-ADPR is less Ca^{2+} -dependent (116) and there is no temperature-dependent effect on the activation (Figure 4.17A) indicating a more stringent fine-regulation of ADPR-dependent TRPM2 activation. This might be necessary due to the increased ADPR levels upon oxidative stress (4, 160); no distinct physiological pathway has been associated to 2'-deoxy-ADPR so far. Otherwise, a ligand-related preference for the two binding sites would also be conceivable. This option could be addressed by the mutational strategy used by Luo and coworkers, who evaluated the

Ca²⁺-dependent ADPR-evoked TRPM2 currents of various amino acid mutations in the EF-loop in MHR1/2 (107). Comparable experiments with 2'-deoxy-ADPR might explain the different Ca²⁺-dependency of the two ligands and help to answer the question, whether a distinction is made between ADPR and 2'-deoxy-ADPR based on the two ligand binding sites.

While the N-terminal EF-loop moves substantially, no obvious rearrangements occur in the Calmodulin binding site within the NUDT9H domain when the overall channel conformation changes. Together with the observed stabilization of the isolated NUDT9H domain (Figure 4.12, Figure 4.14), this would indicate a Calmodulin-binding dependent stabilization of the open TRPM2 conformation when Calmodulin wraps around the P-loop.

In the structures of *dr*TRPM2, the NUDT9H domain shows less interspatial interactions to the MHR1/2 domain (86, 87). The Calmodulin binding site in the *dr*NUDT9H domain is not conserved, the invertebrate channel contains even a partial P-loop deletion. This might also explain the temperature insensitivity of *dr*TRPM2 (161).

Using isolated NUDT9H and Calmodulin, the proteins interact at elevated temperatures when NUDT9H is partially unfolded which, preceded to the thermal stabilization of NUDT9H by Ca²⁺-Calmodulin (section 4.2.2.2). Binding of Calmodulin to NUDT9H sensitizes the temperature-dependent TRPM2 activation by ADPR (Figure 4.17). TRPM2 can be activated at ~41 °C (111, 114) but the temperature threshold for activation is lowered to physiological (body) temperature in the presence of H₂O₂ (84, 114). Met215 is critically involved in temperature-sensitization by H₂O₂, direct oxidation by H₂O₂ was suggested (114). Interestingly, Met215 is located in the vicinity of the N-terminal ADPR binding site as well as the EF-loop (85) and therefore might also be affected by the Calmodulin-dependent interaction.

Taken together, Calmodulin binding to the (partially unfolded) NUDT9H domain contributes to activation of *hs*TRPM2 by temperature but further structural and functional studies are necessary to clarify the role of the individual contributors for channel regulation.

5 Perspective

The complete development of an ADPR FRET sensor including its evaluation in a cellular context is highly desirable to visualize ADPR signaling processes in living cells. In the context of TRPM2, H₂O₂ stimulation of *hs*TRPM2 expressing cells could provide further insight into the ADPR-TRPM2 signaling pathway. Furthermore, engineering the FRET sensor with regard to a specificity for ADPR and 2'-deoxy-ADPR is desirable in order to identify the cellular pathway of the TRPM2 superagonist.

The new findings about NUDT9 might not only contribute to the understanding of the pyrophosphatase but also to the NUDT9H domain in TRPM2, especially in the context of its development during evolution. Since the NUDT9H domain in *nv*TRPM2 hydrolyses ADPR, the ADPR availability for the N-terminal binding site is restricted and thereby the channel activity is controlled (127, 136). Comparable to NUDT9, a regulatory discrimination in *nv*TRPM2 based on the availability of the co-factor is also conceivable: ADPR can bind but is not hydrolyzed when Mg²⁺ is replaced by Ca²⁺ as co-factor. Ca²⁺ sparks occurring when Ca²⁺ ions enter the pore might transiently allow ADPR binding to *nv*NUDT9H and thereby permit a primordial channel regulation. To elucidate this hypothesis, patch clamp experiments of *nv*TRPM2 using Mg²⁺ free buffers could be performed.

The temperature-dependence of *hs*TRPM2 has developed in the course of evolution facilitated by the insertion of a P-loop in the NUDT9H domain that allows temperature-sensitization by Calmodulin binding. As the structure-function relationship is distinctly different in *nv*TRPM2, *dr*TRPM2 and *hs*TRPM2, the analysis of channel chimeras at elevated temperatures could help to understand channel regulation by the different stimuli.

To gain more insights in the Calmodulin-dependent regulation of TRPM2, structures of TRPM2 in complex with Calmodulin are highly favorable if not inevitable. They might clarify uncertainties about Calmodulin binding sites as well as domain associations and interactions and finally the channel regulation by Ca²⁺ and temperature.

6 Material and Methods

6.1 Material

6.1.1 Chemicals

Unless otherwise stated, all reagents and chemicals were purchased from Sarstedt, Carl Roth, Sigma-Aldrich or Thermo Fisher Scientific. 2'-deoxy-ADPR was purchased from Biolog Life Science Institute (Bremen, Germany). $^{15}\text{N-NH}_4\text{Cl}$ was purchased from Silantes (Munich, Germany). $^2\text{H},^{13}\text{C}$ -glucose was purchased from Eurisotop (Saint-Aubin, France).

Table 6-1: Chemicals.

Compound	CAS-No.	GHS hazard	hazard statements	precautionary statements
2'-deoxy-ADPR	111864-49-4	-	-	-
2-Mercaptoethanol	60-24-2	GHS06, GHS09	H302, H411, H315, H335, H311, H319	P280, P312, P302+350, P261, P273, P301+312, P305+351+338
5-D-glucose	50-99-7	-	-	-
$^2\text{H},^{13}\text{C}$ -D-glucose	201417-01-8	-	-	-
Acetic acid, 96 %	64-19-7	GHS02, GHS05	H226, H314	P280, P305+351+338, P310 P210, P280, P304+340+312,
Acetone	67-64-1	GHS02, GHS07	H225, H319, H336	P305+351+338, P337+313, P403+235
Acrylamide 37 %	79-06-1	GHS06, GHS08	H301, H312, H315, H317, H319, H332, H340, H350, H361f, H372	P201, P280, P301+310, P305+351+338, P308+313
Adenosine diphosphoribose salt	5'-sodium 68414-18-6	GHS07	H315-H319-H335	P261-P305 + P351 + P338
Agar-Agar	9002-18-0	-	-	-

6 MATERIAL AND METHODS

Compound	CAS-No.	GHS hazard	hazard statements	precautionary statements
Agarose	9012-36-6	-	-	- P260, P264, P270, P272, P280, P301+312,
Alexa Fluor™ 488 C ₅ Maleimide	500004-82-0	GHS05	H302, H314, H317	P301+330+331, P303+361+353, P304+340, P305+351+338, P501 P303+361+353, P305+351+338,
Alexa Fluor™ 546 C ₅ Maleimide	none	GHS05, GHS07	H302, H314, H317	P304+340, P301+312, P272, P261 P303+P361+P353, P305+P351+P338,
Alexa Fluor™ 555 C ₂ Maleimide	none	GHS05, GHS06, GHS07	H302, H314, H317	P304+P340, P301+P312, P272, P261 P303+361+353, P305+351+338,
Alexa Fluor™ 594 C ₅ Maleimide	none	GHS05, GHS06, GHS07	H302, H314, H317	P304+340, P301+312, P272, P261 P301+312+330, P305+351+338
Ammonium chloride NH ₄ Cl	12125-02-9	GHS07	H302, H319	P264, P270, P280, P301+312,
Ammonium ¹⁵ N NH ₄ Cl	39466-62-1	GHS07	H302, H319	P305+351+338, P337+313 P280, P261,
Ampicillin	69-52-3	GHS08	H317, H334	P302+352, P342+311 P280,
APS	7727-54-0	GHS03, GHS07, GHS08	H272, H302, H315, H317, H319, H334, H335	P305+351+338, P302+352, P304+341, P342+311

6 MATERIAL AND METHODS

Compound	CAS-No.	GHS hazard	hazard statements	precautionary statements
β-Mercaptoethanol	60-24-2	GHS05, GHS06, GHS08, GHS09	H301+H331-H310- H315-H317-H318- H373-H410	P260, P262, P273, P280, P301+310+330, P302+352+310, P305+351+338+310, P391, P403+233
Boric acid (H ₃ BO ₃)	10043-35-3	GHS08	H360FD	P201, P308+313
Bromphenol blue	115-39-9	-	-	-
CaCl ₂	10043-52-4	GHS07	H319	P305+351+338
CoCl ₂	7791-13-1	GHS07, GHS08, GHS09	H302, H317, H334, H341, H350i, H360F, H410	P273, P280, P301+312, P302+352, P304+340+312, P308+313
CuCl ₂	10125-13-0	GHS05, GHS07, GHS09	H302 + H312 - H315 - H318 - H410	P264, P273, P280, P301+312, P302+352+312, P305+351+338
CuSO ₄	7758-98-7	GHS07, GHS09	H302, H315, H319, H410	P264, P270, P273, P301+312, P302+352, P305+351+338
D ₂ O	7789-20-0	-	-	-
Di-Sodium phosphate	hydrogen 7558-79-4	-	-	-
Di-Potassium phosphate	hydrogen 16788-57-1	-	-	-
Dimethylformamid	68-12-2	GHS02, GHS07, GHS08	H226- H312+H332- H319-H360D P	P201-P210-P261- P280-P308+P313- P370+P378
DNase I	-	-	-	-
DTT	578517	GHS07	H302, H315, H319, H335	P302+352, P305+351+338
EDTA	60-00-4	GHS07	H319	P305+351+338
EGTA	67-42-5	-	-	-
Ethanol	64-17-5	GHS02	H225	P210

6 MATERIAL AND METHODS

Compound	CAS-No.	GHS hazard	hazard statements	precautionary statements
EZ-Link™ Sulfo-NHS-LC-Biotin- und Markierungs-Kits	-	-	-	-
FeCl ₃	7705-08-0	GHS05, GHS07	H290, H302, H315, H318	P234, P264, P280, P301+312, P302+352, P305+351+338
Fetal bovine serum	-	-	-	-
Glycerol	56-81-5	-	-	-
HCl, 36 %	7647-01-0	GHS05, GHS07	H290 - H314 - H335	P280 - P303 + P361 + P353 - P305 + P351 + P338 + P310
HEPES	7365-45-9	-	-	-
Imidazole	288-32-4	GHS05, GHS06, GHS08	H301, H314, H361	P260, P281, P303+361+353, P301+330+331, P305+351+338, P308+313
IPTG	367-93-1	-	-	-
Isopropanol	67-63-0	GHS02, GHS07	H225, H319, H336	P210, P233, P305+351+338
JetPEI	-	-	-	-
Kanamycin sulfate	25-389-04-0	GHS08	H360	P201-P308+P313
KCl	7447-40-7	-	-	-
KOH	1310-58-3	GHS05, GHS07	H290-H302-H314	P260-P280-P301 + P312 + P330-P303 + P361 + P353-P304 + P340 + P310-P305 + P351 + P338
LB-medium Lennox	-	-	-	-
Lysozyme (<i>Gallus gallus</i>)	12650-88-3	-	-	-
MnCl ₂	7773-01-5	GHS02, GHS06	H301, H318, H373, H411	P273, P280, P301+310+330, P305+351+338+310, P314

6 MATERIAL AND METHODS

Compound	CAS-No.	GHS hazard	hazard statements	precautionary statements
				P210-P280-
Methanol	67-56-1	GHS02, GHS06, GHS08	H225- H301+H311+H331- H370	P302+352+312- P304+340+312- P370+378- P403+235
MgCl ₂	7786-30-3	-	-	-
MgSO ₄	7487-88-9	-	-	-
Milk powder	68514-61-4	-	-	-
MOPS (3-(N-Morpholino)propanesulfonic acid-4-Morpholinepropanesulfonic acid)	1132-61-2	-	-	-
NaCl	7647-14-5	-	-	-
Na di-hydrogenphosphate dihydrate	13472-35-0	-	-	-
NaOH	1310-73-2	GHS05	H290-H314	P260-P280-P303 + P361 + P353-P304 + P340 + P310-P305 + P351 + P338
N-methyl-D-glucamine (NMDG)	6284-40-8	-	-	-
Penicillin-Streptomycin	-	GHS07	H315, H317, H334, H335	P280, P261, P264, P284, P271, P302+P352, P333+P313, P304+P340, P342+P311, P312, P403+P233, P501
Pierce™ NeutrAvidin™ beads	-	-	-	-
Polyethylenimine	9002-98-6	GHS05, GHS07	H302-H317-H319- H411	P273-P280-P305 + P351 + P338
Potassium acetate	127-08-2	-	-	-
Potassium Carbonate	584-08-7	GHS07	H315, H319, H335	P302+P352, P305+351+338
Potassium di-hydrogen phosphate	7778-77-0	-	-	-

6 MATERIAL AND METHODS

Compound	CAS-No.	GHS hazard	hazard statements	precautionary statements
Roti-Gel Stain	-	-	-	-
Rubidium chloride RbCl	7791-11-9	-	-	-
SDS	151-21-3	GHS02, GHS06	H228, H302, H311, H315, H319, H335	P210, P261, P280, P312, P305+351+338
TEMED	1185-53-1	GHS07	H315, H319, H335	P261, P305+351+338
Tris hydrochloride	1185-53-1	-	-	-
Tryptone/Peptone	8952-4	-	-	-
Trypsin	9002-07-7	GHS07, GHS08	H315, H319-334- 335	P261, P280, P284, P304+P340, P337+P313, P342+P311
Yeast Extract YNB (Y-1251)	8013-01-2	-	-	-
Yeast Nitrogen Base without Amino Acids and Ammonium Sulfate	-	-	-	-
ZnCl ₂	7646-85-7	GHS05, GHS07, GHS09	H302, H314, H410	P260, P273, P280, P301 + P330 + P331, P303 + P361 + P353, P305 + P351 + P338
ZnSO ₄ heptahydrate	7446-20-0	GHS05, GHS07, GHS09	H302, H318, H410	P273, P280, P305+351+338, P501

6.1.2 Buffers and solutions

All buffers and solutions were prepared using de-ionized water from a Milli-Q ultrapure lab water system (Merck Millipore, Germany) and filtered through a 0.22 µM filter prior to use. The pH was measured and adjusted using a peqMeter 1.14 (peqlab via VWR, UK).

6 MATERIAL AND METHODS

Table 6-2: Composition of buffers and solutions.

Description	Composition
RF-1 buffer	100 mM RbCl, 50 mM MnCl ₂ , 30 mM K-Acetate, 10 mM CaCl ₂ , 10 % glycerol, pH 5.8 (adjusted using acidic acid)
RF-2 buffer	10 mM MOPS, 10 mM RbCl, 75 mM CaCl ₂ , 15 % glycerol, pH 6.8 (adjusted using acidic acid)
Trace elements A	50 g/L EDTA (pH 7.5), 8.3 g/L FeCl ₃ * 6 H ₂ O, 0.84 g/L ZnCl ₂ , 0.13 g/L CuCl ₂ * 2 H ₂ O, 0.10 g/L CoCl ₂ * 6 H ₂ O, 0.10 g/L H ₃ BO ₃
Trace elements B	24 g/L CuSO ₄ * H ₂ O, 30 g/L MnCl ₂ * 4 H ₂ O, 2.7 g/L ZnSO ₄ * 7 H ₂ O, 2.7 g/L CoCl ₂ * 6 H ₂ O
HPLC buffer	50 mM KH ₂ PO ₄ , 2 mM MgCl ₂ or CaCl ₂ , pH 7.2
Bath solution (Patch clamp)	140 mM N-methyl-D-glucamine (NMDG), 5 mM KCl, 3.3 mM MgCl ₂ , 1 mM CaCl ₂ , 5 mM D-glucose, 10 mM HEPES, adjusted to pH 7.4 with HCl
Intracellular solution (Patch clamp)	120 mM KCl, 8 mM NaCl, 1 mM MgCl ₂ , 10 mM EGTA, 5.6 mM CaCl ₂ , 10 mM HEPES, adjusted to pH 7.2 with KOH
TAE buffer	0.17 M TrisHCl, 1 mM EDTA, pH 8, 20 mM acetic acid
1x Laemmli buffer (SDS PAGE)	190 mM glycine, 24.8 mM Tris-HCl, 0.1% (w/v) SDS
Stacking buffer (SDS PAGE)	0.5 M Tris-HCl pH 6.8, 0.4% (w/v) SDS
Separating buffer (SDS PAGE)	1.5 M Tris-HCl pH 8.8, 0.4% (w/v) SDS
5x sample buffer (SDS PAGE)	50 mM Tris-HCl pH 6.8, 10% (w/v) SDS, 50% (v/v) glycerol, 125 mM DTT, 0.1% (w/v) Bromophenol blue
FRET buffer	20 mM HEPES (pH 7.5), 150 mM NaCl, 5 mM MgCl ₂
Blotting buffer	3 g/L Tris, 14.4 g/L glycine, 20 % (v/v) methanol, 0.05 % SDS
TBS buffer	50 mM Tris (pH 7.5), 150 mM NaCl

6.1.3 Culture media

All culture media that were utilized during the study are shown in Table 6-3 alongside their composition. The media were sterilized prior to use.

6 MATERIAL AND METHODS

Table 6-3: Composition of Culture Media.

Description	Composition
Terrific broth (TB) media	24 g/L yeast extract, 12 g/L tryptone, 4 mL/L glycerol, 0.017 M KH ₂ PO ₄ , 0.072 M K ₂ HPO ₄
M9 minimal media (for ¹⁵ N isotope labeling)	6 g/L Na ₂ HPO ₄ , 3 g/L KH ₂ PO ₄ , 0.5 g/L NaCl, 0.5 g/L ¹⁵ N NH ₄ Cl, 4 g/L D-glucose, 1 mM MgSO ₄ , 300 mM CaCl ₂ , 1 mL/L Trace elements A, 0.1 mL/L Trace elements B
10x M9 minimal media in D ₂ O (for ² H, ¹³ C, ¹⁵ N isotope labeling)	5.4 g/90 mL Na ₂ HPO ₄ , 2.7 g/90 mL KH ₂ PO ₄ , 0.45 g/90 mL NaCl

6.1.4 Plasmid Vectors

Table 6-4 shows all plasmid vectors with their inserts that were used in this study.

Table 6-4: Plasmid Vectors.

Insert	Vector backbone	Source
NUDT9H	pET42a(+)	My master thesis (Ralf Fliegert lab)
Calmodulin wt	pET15b(+)	Henning Tidow lab
TRPM2 wt	pIRES2-EGFP	Ralf Fliegert lab
TRPM2 W1355A I1368A	pIRES2-EGFP	This thesis
NUDT9 wt	pET51b(+)	Bachelor thesis by F. Möckl (Ralf Fliegert lab)
NUDT9 E230I F231L	pET51b(+)	This thesis
NUDT9trC _{W339}	pET51b(+)	This thesis
NUDT9trC _{W339} E230I F231L	pET51b(+)	This thesis
NUDT9trC _{W339} E230I F231L C207S	pET51b(+)	This thesis
NUDT9trC _{W339} E230I F231L C207S S78C S182C	pET51b(+)	This thesis
NUDT9trC _{W339} E230I F231L C207S S78C S243C	pET51b(+)	This thesis
NUDT9trC _{W339} E230I F231L C207S S118C S182C	pET51b(+)	This thesis

6 MATERIAL AND METHODS

Insert	Vector backbone	Source
mTFP1-NUDT9-mVenus (wt and cp-variants (Table 3-5))	pTriEX	This thesis based on EKAR2G_design1_mTFP_wt_Venus_wt (Addgene ID #39813) and the
mTFP1-NUDT9trC _{W339} -mVenus (wt and cp-variants (Table 3-5))	pTriEX	EKAR2G_design1_mTFP_cp_Venus_cp kit (Addgene ID#1000000021) (146)
mTFP1 _{wt} -NUDT9trC _{D336} -(EAAAK) ₂ -mVenus _{wt}	pTriEX	
mTFP1-NUDT9trC _{D336} -(EAAAK) ₅ -mVenus (wt and cp-variants (Table 3-5))	pTriEX	
YFP-NUDT9-CFP	pTriEX	This thesis based on pcDN3_Epac1
YFP-NUDT9trC _{D341} -CFP	pTriEX	camp from Viacheslav Nicolaev lab
YFP-NUDT9trC _{D336} -(EAAAK) ₂ -CFP	pTriEX	

6.1.5 Primers

All primers for the NUDT9 project (chapter 3) were purchased from Sigma Aldrich. The primers for the TRPM2 project (chapter 4) were purchased from MWG Eurofins. Primers design was carried out using the OligoAnalyzer tool by Integrated DNA technologies (<https://eu.idtdna.com/calc/analyzer>).

Table 6-5: Primers.

Primer	Additional feature	5'-Sequence
General NUDT9 constructs		
NT9_RIL_fw	NUDT9 NUDIX box mutation (E230I F231L)	GATCTCTGCTACATTAAAGCGTATTCTGGGTG AGGAGGCGTTGAACTCATTACAG
NT9_RIL_re		CTGTAATGAGTTCAACGCCTCCTCACCCAGAA TACGCTTTAATGTAGCAGAGAT
NT9trun+T EV_fw	NUDT9 C-terminal truncation	GGTTGCTGAGAAGCGTGATGCCCATGGGAA AACCTGTATTTTCAGGGCTCCGCTCATCACCA CCATCATCAC

6 MATERIAL AND METHODS

Primer	Additional feature	5'-Sequence
NT9trun+T EV_re	NUDT9trC _{W339}), TEV cleavage site insertion	GTGATGATGGTGGTGTGATGAGCGGAGCCCTG AAAATACAGTTTTTCCAATGGGCATCACGCT TCTCAGCAACC
Genetically encoded NUDT9 FRET sensors		
NT9_delBs pEI_fw	Deletion of BspEI cleavage site in NUDT9	GGGAACAAAATTATGCATCCGGTATCTGGAA AACATATTTTACAGTTCGTGGCG
NT9_delBs pEI_re		CGCCACGAACTGTAAAATATGTTTTCCAGATA CCGGATGCATAATTTTGTTC
NT9_BspEI _fw	Insertion of BspEI site at the N-terminus of NUDT9	aaaTCCGGAatggAAAATTCTCATAACAAGGCG CGTACC
NT9fl_NotI _re	Insertion of C-terminal NotI site into NUDT9 full length	TTTGCGGCCGCAAGAGCATGGCAATCAGCCT CC
NT9trC_No tl_re	Insertion of C-terminal NotI site into NUDT9trC _{W339}	tttCGCGGCCGCCCAATGGGCATCACGCTTCT CAG
NT9D336_E AAAK2_fw	Insertion of 2xEAAK linker between NUDT9trC _{D336} and mVenus	<u>CATTAAGTTGGTTGCTGAGAAGCGTGATgaag</u> ccgccccaagaagccgcccaaa <u>GCGGCCGCGA</u> <u>TGgtgagcaagg</u>
NT9D336_E AAAK2_re		<u>CCTTGCTACCATCGCGCCGCTTTGGCGGC</u> <u>GGCTTCTTTGGCGCGGCTTCATCACGCTTCT</u> <u>CAGCAACCAACTTAATG</u>
NT9D336_E AAAK+3_fw	Insertion of additional 3xEAAK linkers between NUDT9trC _{D336} - (EAAK) ₂ and mVenus	<u>ccaaagaagccgcccaaaGAGGCAGCAGCTAA</u> <u>GGAAGCAGCTGCTAAAGAGGCTGCAGCTAA</u> <u>Ggcgcccgatggtgagc</u>
NT9D336_E AAAK+3_re		<u>GCTCACCATCGCGCCGCTTAGCTGCAGCC</u> <u>TCTTTAGCAGCTGCTTCTTAGCTGCTGCCTCT</u> <u>TTGGCGCGGCTTCTTTGG</u>
NUDT9Eco Rlfor	Insertion of N-terminal EcoRI site in NUDT9	<u>aaagaattcgAAAATTCTCATAACAAGGCGC</u>
NUDT9Xba Irev	Insertion of C-terminal XbaI site in NUDT9 full length	<u>aaatctagaAAGAGCATGGCAATCAGC</u>
NUDT9shor tXbarev	Insertion of C-terminal XbaI site in NUDT9trC _{E341}	<u>aaatctagaCTCGGACCAATGGGCAT</u>

6 MATERIAL AND METHODS

Primer	Additional feature	5'-Sequence
YFP-ATG-Bam-f2	Removal of YFP-start codon and insertion of C-terminal BamHI site in YFP	<u>aaaggatccgtgagcaagggcgaggagctgttc</u>
CFP-NotI-KpnI-r	Insertion of C-terminal NotI and KpnI sites in CFP	<u>tttggtagccGCGGCCGCTTACTTGTACAGCTCG</u>
D336eaaak 2CFPf	C-terminal truncation of NUDT9 and introduction of 2xEAAK linkers	<u>GGTTGCTGAGAAGCGTGATgaagccgctgcaaaa</u> <u>gaagcagctgcaaaaGTGAGCAAGGGCGAGGAG</u> <u>CTG</u>
D336eaaak 2CFPr	between NUDT9 and CFP	<u>CAGCTCCTCGCCCTTGCTCACTTTCGCAGCTG</u> <u>CTTCTTTTGCAGCGGCTTCATCACGCTTCTCA</u> <u>GCAACC</u>
NUDT9 constructs for Alexa Fluor labeling		
NT9_C207S _fw	C207S mutation in NUDT9	<u>GCGCATCAAACGCAAAGACAGCGGCGAGTG</u> <u>GGCAATCCCAGG</u>
NT9_C207S _re		<u>CCTGGGATTGCCCACTCGCCGCTGTCTTTGCG</u> <u>TTTGATCGCC</u>
NT9_S78C fw	S78S mutation in NUDT9	<u>GGGTCCAAAGTAGAGCGCTGCCAGGTCCCCA</u> <u>ATGAGAAGG</u>
NT9_S78C re		<u>CCTTCTCATTGGGGACCTGGCAGCGCTCTACT</u> <u>TTGGACCC</u>
NT9_S118C _fw	S118C mutation in NUDT9	<u>CCCACAAATCTCTGAGTGCAATTTTCAGTCCTA</u> <u>AATTTAACG</u>
NT9_S118C _re		<u>CGTTAAATTTAGGACTGAAATTGCACTCAGAG</u> <u>ATTTGTGGG</u>
NT9_S182C _fw	S182C mutation in NUDT9	<u>CACTCGTTGGAAGCGCGATTGTTTCAGGGAAC</u> <u>AAAATTATGCATCCGG</u>
NT9_S182C _re		<u>CCGGATGCATAATTTTGTTCCTGAACAATCG</u> <u>CGCTTCCAACGAGTG</u>
NT9_S243C _fw	S243C mutation in NUDT9	<u>GAACTCATTACAGAAAACCTGCGCTGAGAAG</u> <u>CGCGAGATCGAGG</u>
NT9_S243C _re		<u>CCTCGATCTCGCGCTTCTCAGCGCAGGTTTTTC</u> <u>TGTAATGAGTTC</u>
TRPM2 primers		
TRPM2_W1 355A_fw	W1355A mutation in TRPM2	<u>CCCCATGGTCACGCGGGCGAGGCGGAA</u> <u>CGAGGATGGAGCC</u>

6 MATERIAL AND METHODS

Primer	Additional feature	5'-Sequence
TRPM2_W1 355A_re		GGCTCCATCCTCGTTCCGCCTCGCCCGC GTGACCATGGGG
TRPM2_I13 68A_fw	I1368A mutation in TRPM2	GGAGCCATCTGCAGGAAGAGCG CAAAGAAGATGCTGGAAGTGCTG
TRPM2_I13 68A_re		CAGCACTTCCAGCATCTT CTTTGCGCTCTTCTGCAGATGGCTCC

6.2 Methods

6.2.1 Maintenance and growth of bacteria

E.coli strains XL1blue or DH5 α were used for plasmid amplification and cultured in Lennox broth (LB) media (Carl Roth). *E.coli* strains Rosetta2 (DE3) or BL21 (DE3) Gold were used for protein expression and cultured in terrific broth (TB) media. M9 minimal media was used for NMR spectroscopy isotope labeling. For antibiotic selection, Kanamycin at a concentration of 25 μ g/mL or Ampicillin at a concentration of 100 μ g/mL was used.

6.2.2 Preparation and transformation of chemically competent *E.coli* cells

50 mL of *E.coli* cells were cultured in LB media at 37 °C until they reached an optical density of 0.6 (measured at 600 nm) and subsequently cooled down on ice for 15 min. Cells were pelleted at 1000 x g and 4 °C for 15 min and the pellet resuspended in 16.7 mL ice-cold RF-1 buffer and kept on ice for 15 min. Following centrifugation at 1000 x g and 4 °C for 15 min, the pellet was resuspended in 4 mL ice-cold RF-2 buffer and kept on ice for 15 min. Finally, the cells were aliquoted to 100 μ L, flash frozen in liquid nitrogen and stored at -80 °C until further use.

After the chemically competent *E.coli* cells were thawed on ice; 0.1-1 μ g plasmid DNA (maximum volume of 5 μ L) was added to 50 μ L cells and gently mixed by pipetting up and down. Cells were incubated on ice for 20 min and heat shocked at 42 °C for 45 seconds. Subsequently, cells were chilled on ice for 2 min, 1000 μ L of LB medium was added and the cells were recovered at 37 °C for 1 h (gentle shaking). The cells were centrifuged at 10.000 x g for 1 min, resuspended in 100 μ L LB media, plated out on agar plates supplemented by the appropriate antibiotics and cultured at 37 °C overnight.

6.2.3 Preparation and transformation of electrocompetent *E.coli* cells

1 L of *E.coli* cells were cultured in LB media at 37 °C until they reached an optical density of 0.4-0.6 (measured at 600 nm) and subsequently cooled down on ice for 20-60 min. The cells were pelleted at 4000 x g and 4 °C for 15 min. Cells were washed twice using 800 mL and 500 mL ice-cold water (deionized), and centrifuged at 4000 x g and 4 °C for 15 min after each washing step. The cell pellet was resuspended in 20 ml 10 % glycerol and transferred to a 50 mL tube and centrifuged for 15 min at 4 °C and 3800 x g. Finally, the cells were resuspended in 3 mL 10 % glycerol, aliquoted to 50 µL, flash-frozen in liquid nitrogen and stored at -80 °C until further use.

After the electrocompetent *E.coli* cells were thawed on ice; 0.1-1 µg plasmid DNA (maximum volume of 5 µL) was added to 50 µL cells and gently mixed by pipetting up and down. Cells were electro-shocked using a Bio-Rad MicroPulser (Bio-Rad, USA). 300 µL of LB media was added to the cells and they were recovered at 37 °C for 1 h (gentle shaking). 100-350 µL were plated out on agar plates supplemented by the appropriate antibiotics and cultured at 37 °C overnight.

6.2.4 Molecular Biology

6.2.4.1 Amplification PCR

DNA fragments of interest were amplified by polymerase chain reaction (PCR). A standard reaction mixture of 50 µL contained 10-100 ng template DNA, 200 nM of each forward and reverse primer, 200-400 nM of each nucleotide (NEB UK), 1x Pfu reaction buffer and 0.5-1 µL Pfu Turbo DNA polymerase (2.5 U/µL). A general 3-step PCR cycling protocol was as following: 2 min at 95 °C for initial denaturation and polymerase activation, 25 cycles of denaturation (30 seconds at 95 °C), primer annealing (30 seconds at T_m (primer) – 5 °C, usually at 55 °C), and elongation (72 °C for 1-10 min (1 min per 1 kb product size each)) and a final product amplification step at 72 °C for 10 min. A 2-step PCR protocol without a primer annealing step was used for introduction of longer inserts (like TEV cleavage site or linkers) because of the high melting temperature of the respective primers. PCR reactions were carried out using a thermocycler (Thermocycler peqSTAR2x gradient) and amplified products were separated on an agarose gel.

6.2.4.2 QuikChange site-directed mutagenesis PCR

Point mutations were introduced using QuikChange site-directed mutagenesis PCR. PCR reaction was set up as described before (section 6.2.4.1). PCR cycling protocol was run as following: 2 min at 95 °C for initial denaturation and polymerase activation, 20 cycles of denaturation (30 seconds at 95 °C), primer annealing (60 seconds at 55 °C), and elongation (72 °C for 5-10 min (1 min per 1 kb)) and a final product amplification step at 72 °C for 10 min. Afterwards, 1 µL restriction enzyme DpnI (Thermo Fisher, USA) was added to the PCR tube, carefully mixed, centrifuged down, and incubated for 15 min at 37 °C to digest the methylated template DNA. 5 µL of the solution were transformed in competent *E.coli* cells.

6.2.4.3 Restriction enzyme digest

Restriction enzymes were purchased from Thermo Fisher or New England Biolabs (NEB) and used with its recommended buffer.

For plasmid restriction, a reaction mixture of 1-5 µg plasmid, 2 µL restriction enzyme and 1x respective enzyme buffer (unless otherwise stated by the manufacturer) in a final volume of 50 µL were incubated for 1 h at 37 °C.

For PCR product restriction, PCR products were first purified using PCR product purification kit (Qiagen, UK) as described by the manufacturer's instructions; PCR products were eluted in 35 µL ddH₂O. Up to 35 µL of the purified PCR product, 1 µL of the restriction enzyme and 1x of the respective enzyme buffer (unless otherwise stated by the manufacturer) in a final reaction volume of 50 µL were mixed and incubated at 37 °C for 30 min.

Bands were separated on an Agarose gel, excised, and further purified from the gel using a gel extraction kit (Qiagen, UK).

6.2.4.4 DNA fragment ligation

A general ligation reaction contained 100-200 ng linearized vector DNA, the insert in a 1:1 molar ratio, 1x ligase buffer and 1 µL T4 DNA Ligase (Thermo Fisher, USA) in a final reaction volume of 20 µL. The ligation was carried out for minimum 20 min at 16 °C using a PCR thermocycler (Thermocycler peqSTAR2x gradient) or at room temperature overnight. 2-5 µL of the ligation reaction were transformed in competent *E.coli* cells.

6.2.4.5 Agarose gel electrophoresis

For 1% (w/w) agarose gels, the respective amount of agarose was dissolved in TAE buffer by heating the mixture in a microwave. Roti-GelStain (Carl Roth, Germany) was added (1:50.000) and the gel poured into a gel tray (Thermo Fisher, USA). Once the gel was set, it was entirely covered with TAE buffer. Samples were prepared by the addition of 5x DNA loading dye (Thermo Fisher Scientific, USA). 1 kb GeneRuler (Thermo Fisher, USA) served as a molecular size reference. Gels were run at 100 V for 30 min; DNA was visualized by UV illumination and documented using a Bio-Rad GelDoc 200 system (Bio-rad, United Kingdom).

6.2.5 Protein Expression and purification

E.coli strains Rosetta2 (DE3) or BL21 (DE3) Gold were transformed with the respective expression vector and cultured in terrific broth (TB) media for general protein expression or in M9 minimal media for NMR isotope labeling to an optical density of 0.8 (measured at 600 nm) at 37 °C. Suspension cultures were cooled to 20 °C, protein expression was induced using 0.1-1 mM isopropyl- β -D-1-thiogalactopyranoside (IPTG) and conducted overnight. Cells were harvested by centrifugation at 4000 x g for 15-25 min, resuspended in the respective lysis buffer and incubated at room temperature for 15 min for initial lysozyme digest. Cells were ultimately lysed on ice by pulsed sonication for 3x 1 min (50 % amplitude, 35 % power, Bandelin Sonopuls UW70/GM70, Germany), and cell debris was removed by centrifugation at 15.000 x g and 4 °C for 45 min. The protein of interest was purified from the cleared lysate.

Purified protein was concentrated using VivaSpin concentrators (Sigma Aldrich) with a 10 kDa molecular cut off.

The ultimate purification step was always a size exclusion chromatography (SEC) carried out on a ÄKTApure (GE Healthcare, USA) system at 4 °C using a Superdex 200 10/300 increase column (GE Healthcare, USA) equilibrated by 20 mM HEPES (pH 7.5), 150 mM NaCl unless otherwise stated. A flow rate of 0.5 mL/min was applied.

6.2.5.1 NUDT9 wt, genetically encoded FRET sensors, and NUDT9 for Alexa Fluor dye labeling

Wild type NUDT9 and NUDT9 mutants for Alexa dye labeling were expressed from a pET51b(+) vector with a C-terminal 10x histidine tag. Genetically encoded FRET sensors with a N-terminal 6x histidine tag sensors were expressed from a pTriEx vector.

Cell lysis buffer contained 20 mM HEPES (pH 7.5), 300 mM NaCl, 1 mM DTT, 400 µg lysozyme, 40 µg DNaseI, 1 mM MgSO₄ and 10 mM imidazole. The protein of interest was passed through a Ni²⁺-IMAC gravity column, beads were washed using 10 column volumes washing buffer (20 mM HEPES (pH 7.5), 300 mM NaCl, 20 mM imidazole) and proteins were eluted fraction-wise using washing buffer supplemented by 250 mM imidazole. Elution fractions were concentrated up to 10 mg/mL prior to size exclusion chromatography.

6.2.5.2 NUDT9trC, NUDT9trC RIL, ¹⁵N- or ²H,¹³C,¹⁵N-NUDT9trC RIL

The NUDT9 variants were expressed from a pET51b(+) vector. A TEV cleavage site was introduced prior to the C-terminal 10x histidine tag. Detailed expression of ²H,¹³C,¹⁵N-NUDT9trC RIL is described in section 6.2.15. Cells were lysed and purified by Ni²⁺-IMAC as described before (section 6.2.5.1). TEV protease cleavage was carried out during dialysis at 4 °C overnight, buffer conditions were 20 mM HEPES (pH 7.5), 150 mM NaCl, 1 mM DTT. 1 mg TEV protease was used to cleave 25 mg protein. A second Ni²⁺-IMAC removed the cleaved tag and the TEV protease. Flow through and washing fractions were concentrated up to 10 mg/mL prior to size exclusion chromatography.

6.2.5.3 NUDT9H

The TRPM2 NUDT9H domain was expressed from a pET42a(+) as a Glutathione S-transferase (GST) fusion protein to maintain the solubility of the NUDT9H domain which was critical in the past (80). A 6x histidine tag followed by a TEV cleavage site were located between GST and NUDT9H.

All purification steps were carried out in the cold room using cold buffers. Cell lysis buffer contained 50 mM NaH₂PO₄ (pH 8.0), 300 mM NaCl, 10 % glycerol, 40 µg DNaseI, 400 µg lysozyme, 1 mM MgCl₂, 1x protease inhibitor (Roche Complete without EDTA), 1 mM DTT and was supplemented by 10 mM imidazole prior to Ni²⁺-IMAC. The protein solution was

passed through a Ni²⁺-IMAC gravity column, beads were washed using 10 column volumes washing buffer (50 mM NaH₂PO₄ (pH 8.0), 300 mM NaCl, 10 % glycerol, 1 mM DTT, 20 mM imidazole) and proteins were eluted fraction-wise using washing buffer supplemented by 500 mM imidazole. TEV protease cleavage was carried out during dialysis at 4 °C overnight, buffer conditions were 20 mM Tris (pH 7.6), 150 mM NaCl, 1 mM DTT, 10 % glycerol. 1 mg TEV protease was used to cleave 25 mg protein. A second Ni²⁺-IMAC removed the cleaved GST-His₆-tag and the TEV protease. Flow through and washing fractions (dialysis buffer supplemented by 20 mM imidazole) were concentrated prior to size exclusion chromatography. Size exclusion buffer conditions were 20 mM Tris (pH 7.6), 150 mM NaCl, 10 % glycerol.

6.2.5.4 Calmodulin

Calmodulin was expressed from a pET15b(+) vector without any tag.

Cell lysis buffer contained 50 mM Tris (pH 7.4), 50 mM NaCl, 2 mM CaCl₂, 40 µg DNaseI, 400 µg lysozyme, 1 mM MgCl₂, 1x protease inhibitor (Roche Complete without EDTA) and 1 mM DTT. Calmodulin was purified by hydrophobic interaction chromatography (HIC) using a phenylsepharose 6 FF (high solubility) column (GE Healthcare, USA) carried out on an ÄKTastart (GE Healthcare, USA) at room temperature. A flow rate of 1 mL/min was applied. Subsequently sample loading, the column was washed by 10 column volumes of 50 mM Tris (pH 7.4), 50 mM NaCl, 2 mM CaCl₂. Calmodulin was eluted fraction-wise, elution buffer conditions were 50 mM Tris (pH 7.4), 50 mM NaCl, 10 mM EDTA. Elution fractions containing protein were pooled and dialyzed in 25 mM Tris (pH 7.4), 150 mM NaCl, 2 mM CaCl₂, 5 % glycerol overnight at 4 °C. The same buffer condition was used for ultimate size exclusion chromatography.

6.2.6 Sodium-dodecyl sulfate-polyacrylamide gel electrophoresis (SDS PAGE)

The size and purity of a protein sample was assessed by SDS PAGE. Sample buffer was added to the protein samples, the mixture was boiled at 95 °C for 5 min and centrifuged prior to loading on the SDS gel mounted in a Mini-Protean Cell electrophoresis system (Bio-Rad, USA). Gels were run in Laemmli buffer at 200-220 V and a maximum of 80 mA for 30-45 min. Proteins were stained using the Quick Coomassie Stain (Biotrend,

Germany) and the gel destained in water. A broad range molecular weight marker (Thermo Fisher Scientific, USA) was run next to the samples.

6.2.7 Isothermal titration calorimetry (ITC)

ITC measurements were performed on a MicroCal ITC-200 isothermal titration calorimeter (Malvern Panalytical, Malvern, UK) and thermodynamic parameters were analyzed using the MicroCal Origin™ program. The measurements were carried out at 20 °C unless otherwise stated. The general titration protocol comprised an initial injection of 0.5 µL followed by 18 regular 2 µL injections; the injections were interspaced by 150 s and stirring speed was set to 750 rpm. Titration curves were fitted using a one-site binding model unless otherwise stated. Uncertainties in K_D were reported as fitting errors obtained from three independent experiments. Baseline corrections were achieved by titrating the ligand into the corresponding ITC buffer. Prior to the measurements, the samples were extensively dialyzed to the corresponding ITC buffer and the ligands were dissolved in dialysis buffer.

All NUDT9 experiments (section 3.2) were carried out using 10-20 µM NUDT9 in the sample cell. ADPR and 2'-deoxy-ADPR concentrations were 150-200 µM; AMP, ADP and ribose 5-phosphate concentrations were 500 µM. Buffer conditions were 20 mM HEPES (pH 7.5), 150 mM NaCl, 5 mM CaCl₂ or MgCl₂.

Calmodulin-binding experiments to synthesized peptides (section 4.2.1) were carried out using 10 µM Calmodulin and 500 µL peptide. Buffer conditions were 20 mM HEPES (pH 7.5), 150 mM NaCl, 5 mM CaCl₂ or 20 mM HEPES (pH 7.5), 150 mM NaCl, 10 mM EDTA.

Calmodulin-binding to NUDT9H was measured at 35 °C, buffer conditions were 25 mM Tris (pH 7.2), 150 mM NaCl, 2 mM CaCl₂, 5 % glycerol. 600 µM Calmodulin was titrated into 24 µM NUDT9H.

6.2.8 ADPR and 2'-deoxy-ADPR hydrolysis analyzed by HPLC

ADPR and 2'-deoxy-ADPR were hydrolyzed by NudT9 to AMP or 2'-deoxy-AMP and ribose 5-phosphate. Therefore, 1-100 ng NudT9 was incubated with 100 µM ADPR or 2'-deoxy ADPR in a final reaction volume of 150 µl in HPLC buffer. Reactions were incubated at 37 °C for up to 1 h and stopped by the addition of 1 mM KF and freezing of the samples in

liquid nitrogen. Afterwards, the protein was removed by passing the sample through a Vivaspin 500 filter (MWCO 10 kDa, Sigma Aldrich). Methanol to a final concentration of 10 % v/v was added to the filtered samples which were then subjected to reversed-phase ion pair (RP-)HPLC analyses carried out on an Agilent 1260 infinity module (Agilent Technologies) as described previously (116). ChemStation software (Agilent Technologies) was used for data acquisition and analysis. The nucleotides were separated on a Multohyp BDS C18 column (particle size 5 μm , 250 x 4.6 mm, Chromatographie Service, Langerwehe, Germany) applying an increasing methanol gradient (0 min (15%), 3.5 min (15%), 11 min (31.25%), 15 min (31.25%), 25 min (50%), 27 min (50%), 29 min (15%) and 38 min (15%)). A Diode-Array detector (DAD, Agilent Technologies) was used for nucleotide detection at 260 nm, they were assigned and quantified using external standards.

Michaelis Menten (least squares fit) equation:

$$v_0 = \frac{c(v_{max})}{c + K_M} \quad (1)$$

The specific enzyme activity [kat/mg with kat = 1 mol [substrate]/s] was obtained from v_{max} converted from [nmol*min⁻¹* μg enzyme⁻¹] to [noml*s⁻¹* μg enzyme⁻¹] divided by the amount of NUDT9 used.

6.2.9 Differential scanning fluorimetry (nDSF)

Using a nanoDSF differential scanning fluorimeter (Prometheus, NanoTemper Technologies, Munich, Germany) the intrinsic tryptophan fluorescence signal was monitored as a measure of its unfolding state. In more detail, after excitation at 280 nm, the emission at 330 nm and 350 nm was measured while a linear heat ramp (1 °C/min) was applied. The melting point T_m was calculated from the transition point of the ratiometric measurement (F350 nm/F330 nm) plotted against the increasing temperature. For NUDT9 experiments (section 3.2), 10 μM protein alone or supplemented by 50-1000 μM ligand were used; buffer conditions were 20 mM HEPES (pH 7.5), 150 mM NaCl, 5 mM CaCl₂ or MgCl₂. For NUDT9H experiments (section 4.2.2), protein concentrations were 0.2 mg/mL NUDT9H and 1 mg/mL Calmodulin; buffer

conditions were 25 mM Tris (pH 7.4), 150 mM NaCl, 10 % glycerol supplemented by 2 mM CaCl₂ or 3 mM MgCl₂. ADPR was used at a final concentration of 1 mM.

6.2.10 Circular dichroism (CD) spectroscopy

(Far-UV) CD spectra were recorded from 260 to 195 nm using a Jasco J-815 spectropolarimeter (Easton, MD, USA) operated at 20 °C. Each spectrum composed of ten scans was acquired using a scan rate of 20 or 50 nm/min and carried out in quartz cuvettes with a path length of 1 mm (Quartz-Suprasil, Hellma Analytics, Germany). 3 μM NUdT9 and 100 μM of ADPR or 2'-deoxy-ADPR were used, buffer conditions were 20 mM HEPES (pH 7.2), 150 mM NaCl, 5 mM CaCl₂. NUdT9H was used in a concentration of 4 μM, buffer conditions were 25 mM sodium phosphate (pH 7.2), 10 mM MgCl₂, 15 mM NaCl.

6.2.11 Förster or fluorescence resonance energy transfer (FRET)

FRET is a technique that provides information about intra- as well as intermolecular distances in the nanomolar length scale (162, 163) and is therefore a powerful tool to visualize signaling molecules in living cells with high spatiotemporal resolution. FRET exhibited by a donor-acceptor pair is the non-radiative transfer of internal energy from an excited donor fluorophore to a neighboring lower-energy acceptor fluorophore, whereby the acceptor emits its characteristic fluorescence (164, 165). The spectral overlap of the donor's emission and the acceptor's excitation is prerequisite for FRET (Figure 6.1B). The energy transfer is highly distance- and orientation-dependent: FRET occurs when the inter-fluorophore distance (r) is within the 1–10 nm range and the dipoles of the fluorophores are in the correct orientation to each other (Figure 6.1A)

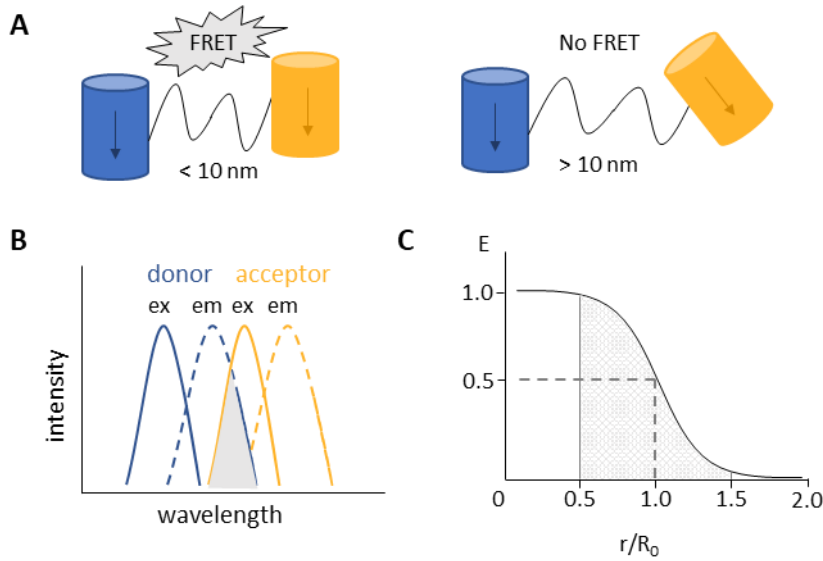


Figure 6.1: Basic principles for Förster resonance energy transfer (FRET). (A) A donor to acceptor distance below 10 nm and a parallel dipole orientation of the two fluorophores are required for FRET to occur. (B) The spectral overlap (grey) of the donor emission (blue, dashed line) and the acceptor excitation (yellow line) is prerequisite for FRET. (C) The Förster distance R_0 is the donor-acceptor separation distance (r) corresponding to 50 % energy transfer efficiency.

A mathematical description of the FRET efficiency (E) based on the inter-fluorophore distance and orientation factors of a FRET sensor is described by (165):

$$E = \frac{R_0^6}{R_0^6 + r^6} \quad (2)$$

With

$$R_0^6 = 0.021 * \eta^{-4} * \kappa^2 * \Phi_D \quad (3)$$

Förster distance R_0 is the donor-acceptor separation distance (r) corresponding to 50 % energy transfer efficiency (Figure 6.1C). The magnitude of the R_0 depends on the spectral properties of the donor and the acceptor including the donor's fluorescence quantum yield in the absence of acceptor (Φ_D), the refractive index of the solution (η), the inter-dipole orientation factor (κ^2), and the spectral overlap integral of the donor and acceptor (J). For a given FRET pair with a specific Förster distance, FRET mainly depends on the fluorophore distance and their dipole orientation; a random inter-fluorophore orientation is usually assumed with $\kappa^2 = 2/3$ (166). The real inter-dipole orientation factor is unknown but can adopt values between 0 (perpendicular dipoles) and 4 (aligned

dipoles) (166, 167). When using circularly permuted variants of fluorescent proteins, the dipole orientation of the FRET pair is specifically altered (145).

6.2.11.1 Genetically encoded FRET sensors

A mTFP1 – mVenus FRET sensor library was developed by Oliver Pertz' lab (146), using the pTriEx 4 vector (Novagen) that both allows pro- and eukaryotic expression. NUDT9 variants were introduced between mTFP1 and mVenus using BspEI (Kpn2I) and NotI sites. YFP-NUDT9-CFP sensors were generated in the pCDNA vector and the subcloned to pTriEX using BamHI and KpnI sites.

Rigid linkers were introduced by PCR using primers that contain the additional sequence (Table 6-5).

Protein expression and purification was carried out as described in section 6.2.5.1.

6.2.11.2 Alexa Fluor dye labeling

Alexa Fluor dyes (Thermo Fisher Scientific, USA) were dissolved to a concentration of 10 mM in ultrapure DMSO, single-use aliquots were stored at -20 °C until further use. Freshly purified NUDT9 (section 6.2.5.1) was diluted to 50 µM in 190 µL FRET buffer supplemented by 1 mM TCEP. Alexa Fluor dyes were premixed (5 µL of each dye), and dropwise added to the protein; a final concentration of 250 µM per dye was reached. The conjugation reaction was proceeded at 4 °C overnight or at room temperature for 2 h in the dark under continuous tube rolling. 2 mM β-Mercaptoethanol was added to consume unbound dye and 800 µL FRET buffer was added. Subsequent incubation for additional 30 min at room temperature, the labeled protein was purified using a PD-10 size exclusion column (GE Bioscience). For sample loading, the 1000 µL labeling solution were allowed to enter the column entirely before 1500 µL FRET buffer were added. 500 µL elution fractions were collected. Protein as well as dye concentrations were assessed by absorption measurement using the NanoDrop Proteins & Labels tool (NanoDrop Spektralphotometer, Thermo-Scientific, Germany), which considers the dye-specific absorption coefficients by default. The first elution fraction containing labeled protein was further gelfiltrated on a Superdex S200 10/300 GL column equilibrated by FRET buffer.

6.2.11.3 Fluorescence spectrometry of FRET sensors

Fluorescence measurements of FRET sensors were carried out on a Cary Eclipse Fluorescence Spectrometer (Agilent, Santa Clara, USA). The scanning speed was 600 nm/min, the slits were set to 5 nm, and PMT voltage was set to maximum of 800 Volts. Quartz cuvettes (Hellma analytics, Germany) with a sample volume of 2000 μ L were used; samples were continuously stirred. All measurements were performed in FRET buffer and at room temperature.

According to the fluorescence intensity and the acceptor to donor ratio, a protein concentration of 25 – 50 nM was used. After acquiring the apo spectrum, 50 to 500 μ M ADPR were added at a maximum ligand volume of 10 μ L. Upon donor excitation, emission scans were acquired capturing the donor as well as the acceptor emission maxima. Parameters used for all FRET pairs are summarized in Table 6-6.

Table 6-6: Parameters for the individual FRET pairs used for fluorescence measurements.

FRET pair	R_0 [Å]	Donor excitation [nm]	Emission scan [nm]	FRET maxima donor / acceptor [nm]
mTFP1 + mVenus	60	462	470 – 600	492 / 515
CFP + YFP	48	440	450 – 600	493 / 527
Alexa Fluor dyes				
488 + 564	64	470	480 – 700	519 / 573
488 + 594	60	470	480 – 700	519 / 612
555 + 594	47	519	530 – 750	564 / 612

The ratio and the changes were calculated according to the following equations:

$$R = \frac{Intensity_{acceptor}}{Intensity_{donor}} \quad (4)$$

With R for ratio.

$$\Delta R = R_{max} - R_{min} \quad (5)$$

and

$$R_{change} = \frac{\Delta R}{R_{min}} \quad (6)$$

6.2.12 Fluorescence measurement of VL24 peptide and Ca²⁺-Calmodulin

Intrinsic tryptophan fluorescence of the VL24 peptide (Table 4-1) was excited at 280 nm and fluorescence emission spectra were acquired from 310 - 400 nm. Slits were set to 10 nm and the PMT voltage was 700 V. 2 μ M VL24 and 4 μ M Calmodulin were used; buffer conditions were 25mM Tris (pH 7.2), 150mM NaCl, 2mM CaCl₂.

6.2.13 Protein crystallization and crystal structure determination

Single proteins, protein-protein or protein-peptide complexes were concentrated (Vivaspin concentrators, molecular cut off 10 kDa) to 5-30 mg/mL prior to crystallization. ADPR or 2'-deoxy-ADPR was added in a concentration of 0.5-5 mM to the concentrated protein. Using the vapor diffusion technique in sitting drops, various commercial crystallization screens were set up at the EBML SPC facility. In an automated set up, a composition of 100-200 nL protein sample and the equivalent volume precipitant agent was pipetted in a 96-well SWISSCI crystallization plate (Molecular Dimensions, USA), which contained the corresponding reservoir solutions. Plates were stored at 19 °C as well as in the cold room and regularly inspected for crystal formation. When necessary, 30 % glycerol or 10 % polyethylene glycol 400 was added as cryo-protectant prior to crystal harvesting. Crystals were stored in liquid nitrogen. X-ray diffraction data were collected at 100 K at the P13 and P14 beamlines of the PETRA III storage ring (DESY, Hamburg, Germany). Data processing was performed using XDS (168) and AIMLESS (169) software. Electron density modification and backbone building was performed using Coot (170).

6.2.14 Small-angle X-ray scattering (SAXS)

Studying dynamic processes of proteins in different environments has become an important aspect in modern structural biology (171, 172). Large conformational changes, complex formation or oligomerization can be analyzed by SAXS (173, 174). SAXS measurements are carried out very close to the primary beam ("small angles"), which makes brilliant X-rays generated by synchrotrons particularly useful. In a standard SAXS set up, a sample in solution is irradiated by a collimated, monochromatic X-ray beam, the scattered radiation is detected by a 2D detector (172, 175). The resolution is limited to

~10 Å due to the random distribution and the rotational averaging of the molecules in solution. Therefore, the detected scattering intensity only depends on the magnitude of the scattering vector q and not on its direction.

$$q = \frac{4\pi \sin \theta}{\lambda} \quad (7)$$

2θ is defined as scattering angle between the incident and scattered beam and λ is the wavelength of incident the X-ray beam (176). Scattering curves were obtained by integration of the 2D detector images around the beam centers. Because the detected scattering intensity is generated from the protein and the surrounding solvent, individual measurements of the sample and the buffer were required and the scattering of the sample is subtracted by the solvent scattering (Figure 6.2A). The global overall particle flexibility is described by the Kratky plot which is related to the particle volume as well as the scattering contrast between the protein and the solvent (Figure 6.2B). Global structural parameters were obtained from the scattering curve such as the radius of gyration (R_G), the molecular mass, general shape information, and the maximum protein dimension (D_{\max} , Figure 6.2C) (177–179).

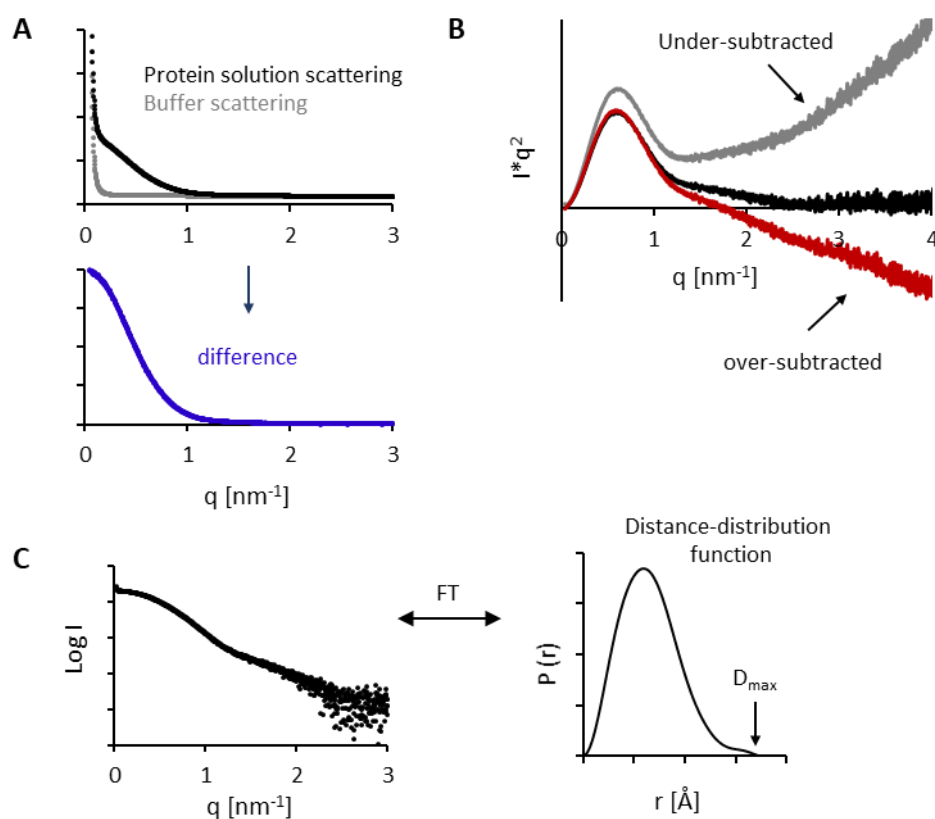


Figure 6.2: SAXS data analysis. (A) Scattering function of the sample is obtained from protein solution scattering subtracted by the buffer scattering. (B) Kratky plot describes the overall particle flexibility and helps to assess buffer subtraction, inter-particle repulsion, and particle aggregation. (C) The distance distribution function is obtained from the scattering curve by indirect Fourier transformation (FT) (177).

R_g is the radial distance from the center of mass and depicts the size and mass distribution within a particle. The plot of $\ln I(q)$ against q^2 results in a linear fit in the low q range, the slope of the fit corresponds to R_g (180).

SAXS data are highly sensitive to sample quality and experimental procedures. Inter-particle interference, aggregation or poor buffer subtraction are some of the main problems. However, a major strength of SAXS is the ability to compute structural parameters independently, e.g. both R_g and mass information can be derived by Guinier or pair-distance distribution analysis (172).

All data were collected on the P12 beamline at Deutsches Elektronen Synchrotron (DESY, Hamburg, Germany). Data were processed using the software PRIMUS (32) as following: Data averages were normalized and the background subtracted using automatic procedures on the beamline. Forward scattering intensity of bovine serum albumin (BSA) was used for calibration of the scattering intensity into absolute units of cm^{-1} . The scattering curves of all samples were buffer subtracted and the radii of gyration extracted by the Guinier approximation. Using the program GNOM (177), the maximal protein dimension (D_{max}) was calculated from the entire scattering curve.

All measurements were carried out at room temperature, buffer conditions were 20 mM HEPES (pH 7.5), 150 mM NaCl, 5 mM CaCl_2 or MgCl_2 . 160 μM and 80 μM of each NUDT9 variant was measured alone or supplemented by 1 mM ADPR or 2'-deoxy-ADPR, respectively.

6.2.15 Nuclear magnetic resonance (NMR) spectroscopy

6.2.15.1 Expression of uniformly labeled protein

Uniformly labelled Calmodulin and NudT9trC_{W339}-RIL were expressed using *E.coli* strain BL21 (2DE3) Gold grown in M9 minimal media containing $^{15}\text{NH}_4\text{Cl}$ as only nitrogen source.

For triple labelled NUDTtrC_{W339}-RIL, a cell adaption to increasing D₂O concentrations was carried out over several days. The following protocol describes the quantities required for 1 kg (909 mL) of culture. A starter culture in rich Media (LB media) of transformed *E.coli* BL21 (2DE3) Gold cells were 1:20 diluted in 50 % D₂O starter culture. For a total volume of 2 mL 50 % D₂O starter culture, 1.8 mL media containing 200 µL 10x M9 (in D₂O), 200 µL 10x NH₄Cl, 40 µL 20 % glucose, 200 µL 10x YNB (17 g/L; Y1251, Sigma), 2 µL Ampicillin (1000 x stock containing 0.1 g/mL in H₂O), 800 µL D₂O and 558 µL H₂O were prepared and mixed with 200 µL of the rich starter culture. After 24 h incubation at 37 °C, 2 mL 50 % D₂O starter culture were inoculated into 50 mL 78 % D₂O starter culture (5 mL/50 mL 10x M9 in D₂O, 5 mL/50 mL 10x NH₄Cl, 1 mL/50 mL 20 % glucose, 5 mL/50 mL 10x YNB, 0.5 mL 1000 x Ampicillin (in D₂O), 33.5 mL/50 mL D₂O). After 24 h incubation at 37 °C, 1.5 g YNB, 0.9 g ¹⁵N-NH₄Cl and 3.5 g ¹³C-glucose were dissolved in D₂O, filter sterilized and added into the media containing 1x M9 (in D₂O), 1x Ampicillin and the 50 mL 78 % D₂O starter culture (total volume of 909 mL). The cells were grown at 37 °C until OD (measured at 600 nm) reached 1.0-1.2, protein expression was induced using 0.2 mM IPTG (dissolved in D₂O) and carried out for 14 h at 20 °C.

Protein purification was carried out as described in section 6.2.5.

6.2.15.2 NMR data acquisition

All NMR measurements were performed by Trevor J. Rutherford at the laboratory for Molecular Biology in Cambridge (UK).

For Calmodulin binding studies, NMR spectra were acquired on a Avance III spectrometer (Bruker, USA) operating at 600 MHz ¹H frequency and equipped with cryogenic inverse probe and single-axis gradients. BEST-TROSY spectra (181) were acquired at 298 K with concentrations of VL24 and uniformly labeled ¹⁵N-Calmodulin of 250 µM and 130 µM, respectively; buffer conditions were 25 mM Tris (pH 7.2), 150 mM NaCl, 5 mM CaCl₂, 5 % (v/v) D₂O. Spectra were acquired with 2048 and 256 data points in *t*₂ and *t*₁, respectively, covering spectral widths of 14.0 and 31.0 ppm.

For NUDT9trC_{W339}-RIL binding studies, MNR spectra were acquired on a an Avance III spectrometer (Bruker, USA) equipped with an inverse detection cryogenic probe operating at 700 or 800 MHz ¹H frequency. All spectra were acquired in 20 mM HEPES

(pH 7.5), 150 mM NaCl, 5 mM CaCl₂, 5 % D₂O (v/v) except the pH control sample, which was acquired in 20 mM HEPES (pH 7.2), 150 mM NaCl, 5 mM CaCl₂, 5 % D₂O (v/v). For binding studies, 800 MHz BEST-TROSY spectra (181) were acquired at a sample temperature with 100-130 μM uniformly labelled ¹⁵N-NUDT9trC_{W339}-RIL alone or supplemented with 1 mM ADPR or 2'-deoxy-ADPR, respectively. The raw data matrix was 128 complex x 2048 points in *t*₁ and *t*₂, respectively, with an interscan relaxation delay of 0.6 s. A control experiment acquired with a small pH offset was used to identify TROSY peaks that are perturbed by small general changes to buffer conditions and may not necessarily be reflective of ligand binding interactions. For backbone resonance assignment, TROSY-based 3D HN(CA)CO, HNCO, HNCA, HN(CO)CA, Cβ-optimized HNCACB and HN(CO)CACB spectra were acquired for 230 μM triple labelled ²D,¹³C,¹⁵N-NUDT9trC_{W339}-RIL at 700 MHz ¹H, temperature was set to 298 K. A non-TROSY (H)N(COCA)NH spectrum was also acquired for the same sample. All spectra were acquired with unmodified Bruker pulse programs, processed with TopSpin version 3.2 software (Bruker), and analyzed using NMRFAM-Sparky (182).

6.2.16 HEK293 cell culture and transfection

Human embryonic kidney (HEK293) cells were cultured in Dulbecco's Modified Eagle Medium (DMEM) with 4.5 g/L glucose and GlutaMax-I (Gibco) supplemented with 10% (v/v) fetal bovine serum (Biochrom, Germany) at 37 °C and 5 % CO₂.

JetPEI was used to transfect HEK293 cells for patch clamp analyses (section 6.2.18). 5 μL jetPEI reagent (PolyPlus Transfection, Strasbourg, France) and 2.5 μg plasmid DNA were mixed in a total volume of 250 μL (150 mM NaCl) and incubated at room temperature for 30 min to form a transfection complex. HEK293 cells grown to a density of approx. 80 % were detached and counted using the Neubauer cell counting chamber. 2.5 × 10⁵ cells/mL were mixed with the transfection complex, seeded to 350 mm cell culture at a low density and incubated for 24 h at 37 °C and 5 % CO₂.

Lipofectamine transfection was used to transfect HEK293 cells for the surface expression assay. 6 μg of Plus reagent (Invitrogen) and 7.5 μg plasmid DNA were mixed in 1.5 ml Opti-MEM (Gibco) and incubated for 5 min at room temperature. 18 μl Lipofectamine LTX (Invitrogen) was added and the complex was incubated for an additional 30 min at room

temperature to form the transfection complex. HEK293 cells were grown in T25 culture flasks to a cell density of approx. 70 % confluency. The medium was replaced by 6.5 mL fresh DMEM medium and the transfection complex added dropwise. After incubation at 37 °C and 5 % CO₂ for 5-6 h, half of the medium was replaced by fresh medium and further incubated for additional 43 h.

The pIRES2-EGFP vector used for all expressions co-expresses EGFP that allows identification of transfected cells using fluorescence microscopy.

6.2.17 Surface expression assay

Cells were carefully washed with D-PBS (with Ca²⁺ and Mg²⁺) and incubated for 30 min at room temperature with 1 mg/ml EZ-Link Sulfo-NHS-LC-Biotin (Pierce/Thermo Scientific) to biotinylate surface proteins. Biotinylated cells were detached using 2 mM EDTA in D-PBS (without Mg²⁺ and Ca²⁺), collected and centrifuged at 500 x g for 5 min at room temperature. Cells were washed twice with 2 mL D-PBS and centrifuged as before. Membrane proteins were extracted using the ProteoExtract Native Membrane kit (EMD Milipore) according to the manufacturer's instructions. Briefly, cells were washed twice with 2mL ice-cold washing buffer and centrifuged at 500 x g at 4 °C for 10 min. 2 mL extraction buffer I supplemented by 10 µL protease inhibitor were added, the cells carefully resuspended and incubated for 10 min in the cold room under continuous rolling. Following centrifugation at 16.000 x g at 4 °C for 15 min, 2 mL extraction buffer II supplemented by 10 µL protease inhibitor were added, the cells carefully resuspended and incubated for 30 min in the cold room under continuous rolling. Following centrifugation at 16.000 x g at 4 °C and 4 °C, the supernatant containing the solubilized membrane proteins was collected and the protein concentration determined by absorption measurement at 280 nm using the NanoDrop (Spektralphotometer, Thermo-Scientific, Germany).

For pull-down of biotinylated membrane proteins, 600 µg membrane proteins were mixed with 100 µL of the 50 % slurry of NeutraVidin Agarose Beads (Pierce/Thermo Scientific) and incubated for 12 h in the cold room while rotating.

Western Blot analyses was used to detect TRPM2 expressed on the surface (biotinylated) and in other membranes. Both, the biotinylated proteins from the pull-down (300 µg of

membrane protein) and 10 µg total membrane proteins were incubated for 7 min at 75 °C in SDS loading buffer and separated on a 4–15% Protean precast SDS PAGE gel (BioRad, USA); the pre-stained broad range protein ladder (Thermo Fisher Scientific, USA) served as molecular reference. Proteins were transferred in blotting buffer onto a PVDF membrane for 90 min at 300 mA/h. The membrane was cut between the 100 and 140 kDa bands to allow simultaneous detection of TRPM2 and the reference Na⁺/K⁺-ATPase. The part of the membrane containing the high molecular weight range was probed using an anti-hsTRPM2 antibody from rabbit (Novus #nb500-241 at 1:50.000 dilution), the other part of the membrane was probed with an anti-Na⁺/K⁺-ATPase antibody from rabbit (Cell Signaling Technology #3010 at 1:1000 dilution); antibodies were incubated over-night in the cold room. The membranes were washed twice using TBS buffer supplemented by 0.1 % Tween 20, and both primary antibodies were detected by an HRP-conjugated anti-rabbit secondary antibody (Dianova #111-035-045 at 1:10.000 dilution) incubated for 1 h at room temperature. Membranes were washed twice in TBS buffer supplemented by Tween 20 and three time in TBS buffer alone. After incubation of the membranes with a mixture of SuperSignal West Dura/Pico chemiluminescent substrates (Pierce/Thermo Fisher Scientific, USA), the chemiluminescence was recorded using a LAS-4000 Intelligent Dark Box (Fujifilm, Tokyo, Japan). Densitometric analysis of the images was performed using Fiji (<http://fiji.sc>) (183).

6.2.18 Electrophysiology and patch clamp technique

The cell membrane (phospholipid bilayer) is an effective barrier for charged ions contributing to different ion concentrations in the extra- and intracellular space. Concentration gradients and a charge imbalance across the membrane lead to a resting membrane potential which is typically -50 to -80 mV (cytosol is more negatively charged, (184), with the equilibrium potential for potassium ions contributing most to this. Membrane spanning ion channels establish and control the membrane permeability for ions and other small water-soluble molecules. The movement of ions across the membrane is a current (and can be expressed in Ampere).

The cell membrane as effective barrier between the very ion-conductive intra- and extracellular media forms an insulator between two conductors. Ion channels,

transporters and some leakage make the insulation imperfect. The so-called membrane resistance R_m limits the current I whereas the driving force (difference between equilibrium and membrane potential E) is proportional to current (Ohm's law).

The current, mainly caused by ion flux through K^+ channels charge the membrane like a capacitor until the potential reaches the K^+ channel equilibrium potential. Biological membranes exhibit a specific capacitance of approx. $1 \mu\text{F}/\text{cm}^2$, thus the capacitance is proportional to the membrane surface area (184). From an electronic perspective, an intact cell can be described as an electronic circuit with membrane resistance R_m (or membrane conductance $G = \text{reciprocal membrane resistance}$), capacitance C_m , and membrane potential E (Figure 6.3).

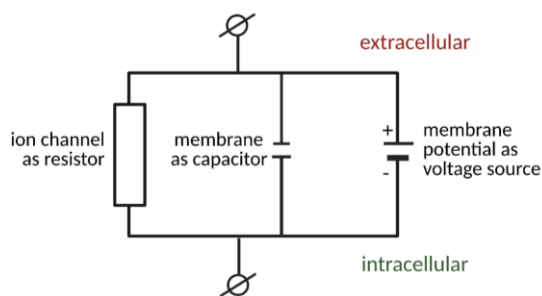


Figure 6.3: Electronic model of the plasma membrane of an intact cell. Adopted from (184).

Changes in membrane potential reflect ion channel activity. To record the activity, voltage clamp controls the membrane potential and directly measures the membrane current. Voltage clamp occurs when a measured potential is compared with a set holding potential (command voltage); any measured alterations of the membrane to the holding potential are corrected by compensatory current injections. The compensatory current injection represents the ionic current over the membrane (opposite in sign). By using specific protocols, varying the command voltage enables the measurement of channel-specific properties.

Patch clamp is an application of the voltage clamp technique. Different patch clamp configurations exist: the cell-attached, outside-out and inside-out excised patch allow single channel measurements; the whole-cell configuration and the perforated patch record macro-currents from all channels in the cell membrane. The rupture of the cell membrane patch under the pipette establishes the whole-cell configuration leading to

the disruption of the membrane potential. The pipette electrode has direct electrical contact with the cytoplasm. The possibility to exchange and therefore to control both the intra- and the extracellular medium during a measurement is an advantage of the patch-clamp technique (185, 186).

6.2.18.1 TRPM2 recordings

Every day prior to the first experiment, the intracellular electrode consisting of an Ag/AgCl wire was carefully sanded and freshly covered with molten silver chloride. Thin-walled borosilicate glass capillaries (1.10 mm × 1.50 mm × 80 mm) were used to prepare patch pipettes using the Sutter P-97 horizontal puller (Flaming/Brown micropipette puller P-97, Sutter instruments Co, USA). Pipettes were not older than 4 h and had a resistance of 1.5 – 5 MΩ (recorded with the pipette in the bath solution without contact to the cell). 4 μL of the pipette solution with or without the respective ligand were filled in the patch pipette.

24 h post transfection, the media was removed from the cells immediately before the experiment. Cells were carefully washed twice with 2 mL bath solution; the experiments were carried out in 2 mL bath solution. The bath solution contained NMDG instead of Na⁺, that prevents cells rupture due to high currents as TRPM2 is impermeable to NMDG. The 35 mm petri dish was placed in the holder and the bath electrode (Ag/AgCl barrel) was entirely dipped in the bath solution (without contact to the dish bottom). For temperature control, an open culture dish incubator (DH-35i, Warner Instruments) connected to a single channel heater controller (TC-324C, Warner Instruments) was used. Cells were continuously perfused at a flow rate of 0.3 mL/min with bath solution pre-warmed in a water bath.

The patch pipette was mounted in the pipette holder and the pipette electrode was connected to a HEKA EPC-10 amplifier (HEKA Elektronik Dr. Schulze GmbH, Germany), and the currents were recorded using the Patch Master software (HEKA Elektronik Dr. Schulze GmbH, Germany). The pipette holder was connected via tubing and a three-way valve to a 5 mL syringe. Using this syringe, a positive pressure was applied before the micropipette tip was dipped into the bath solution.

Based on the co-expressed GFP, transfected HEK293 cells were identified by fluorescence microscopy. The patch pipette was lowered to the cell using a micromanipulator device (PatchMan NP2, Eppendorf, Germany) until a small indentation due to liquid jet emitting from the pipette tip became visible on the cell surface and decreased voltage reflections of the applied test pulse indicated increasing resistance. The cell attached mode was established by opening the three-way valve to release pressure and creating a gigaseal, a tight connection between the cell membrane and the pipette tip. Fast capacitive transients (the small membrane patch acting as capacitor) were compensated using the Auto C-Fast Macro in the PatchMaster Software. Whole cell configuration was established by suction using the syringe that disrupts the cell membrane and was reflected by small capacitive transients (C-slow, compensated, measure of the cell surface area). A proper gigaseal prevents ion leakage and allows ion current recordings. Initially after break-in, the holding potential was set to -50 mV and the voltage protocol was started, the initial membrane potential (V_0) and R_{series} (the sum of access resistance and pipette resistance) were noted for quality control. R_{series} had to be below 4.5 M Ω . To record TRPM2 activity, repetitive voltage ramps from -85 mV to +20 mV over 140 ms were applied every 5 s for 450 s. Cells were clamped to a holding potential of -50 mV before and in between the ramps. Series resistance compensation was set to 70 %. Maximum outward currents recorded at +15 mV were analyzed.

7 References

1. J. M. Pascal, T. Ellenberger, The rise and fall of poly(ADP-ribose): An enzymatic perspective. *DNA Repair (Amst)*. **32**, 10–16 (2015).
2. A. E. Ringel, S. A. Tucker, M. C. Haigis, Chemical and Physiological Features of Mitochondrial Acylation. *Mol. Cell*. **72**, 610–624 (2018).
3. A. L. Perraud, A. Fleig, C. A. Dunn, L. A. Bagley, P. Launay, C. Schmitz, A. J. Stokes, Q. Zhu, M. J. Bessman, R. Penner, J. P. Kinet, A. M. Scharenberg, ADP-ribose gating of the calcium-permeable LTRPC2 channel revealed by Nudix motif homology. *Nature*. **411**, 595–599 (2001).
4. A. L. Perraud, C. L. Takanishi, B. Shen, S. Kang, M. K. Smith, C. Schmitz, H. M. Knowles, D. Ferraris, W. Li, J. Zhang, B. L. Stoddard, A. M. Scharenberg, Accumulation of free ADP-ribose from mitochondria mediates oxidative stress-induced gating of TRPM2 cation channels. *J. Biol. Chem*. **280**, 6138–6148 (2005).
5. F. Di Lisa, M. Ziegler, Pathophysiological relevance of mitochondria in NAD⁺ metabolism. *FEBS Lett*. **492**, 4–8 (2001).
6. L. R. Stein, S. I. Imai, The dynamic regulation of NAD metabolism in mitochondria. *Trends Endocrinol. Metab*. **23**, 420–428 (2012).
7. C. Dölle, J. G. M. Rack, M. Ziegler, NAD and ADP-ribose metabolism in mitochondria. *FEBS J*. **280**, 3530–3541 (2013).
8. E. Michishita, J. Y. Park, J. M. Burneskis, J. C. Barrett, I. Horikawa, Evolutionarily Conserved and Nonconserved Cellular Localizations and Functions of Human SIRT Proteins. *Mol. Biol. Cell*. **16**, 4623–4635 (2005).
9. A. S. Hebert, K. E. Dittenhafer-Reed, W. Yu, D. J. Bailey, E. S. Selen, M. D. Boersma, J. J. Carson, M. Tonelli, A. J. Balloon, A. J. Higbee, M. S. Westphall, D. J. Pagliarini, T. A. Prolla, F. Assadi-Porter, S. Roy, J. M. Denu, J. J. Coon, Calorie Restriction and SIRT3 Trigger Global Reprogramming of the Mitochondrial Protein Acetylome. *Mol. Cell*. **49**, 186–199 (2013).
10. J. L. Feldman, K. E. Dittenhafer-Reed, J. M. Denu, Sirtuin catalysis and regulation. *J. Biol. Chem*. **287**, 42419–42427 (2012).
11. J. M. Denu, The Sir2 family of protein deacetylases. *Curr. Opin. Chem. Biol*. **9**, 431–440 (2005).
12. D. Corda, NEW EMBO MEMBER'S REVIEW: Functional aspects of protein mono-ADP-ribosylation. *EMBO J*. **22**, 1953–1958 (2003).
13. M. C. Haigis, R. Mostoslavsky, K. M. Haigis, K. Fahie, D. C. Christodoulou, A. J. J. Murphy, D. M. Valenzuela, G. D. Yancopoulos, M. Karow, G. Blander, C. Wolberger, T. A. Prolla, R. Weindruch, F. W. Alt, L. Guarente, SIRT4 Inhibits Glutamate Dehydrogenase and Opposes the Effects of Calorie Restriction in Pancreatic β Cells. *Cell*. **126**, 941–954 (2006).
14. A. Herrero-Yraola, S. M. A. Bakhit, P. Franke, C. Weise, M. Schweiger, D. Jorcke, M. Ziegler,

- Regulation of glutamate dehydrogenase by reversible ADP-ribosylation in mitochondria. *EMBO J.* **20**, 2404–2412 (2001).
15. C. Richter, G. E. N. Kass, Oxidative stress in mitochondria: Its relationship to cellular Ca²⁺ homeostasis, cell death, proliferation, and differentiation. *Chem. Biol. Interact.* **77**, 1–23 (1991).
 16. Hon Cheung Lee, R. Aarhus, A derivative of NADP mobilizes calcium stores insensitive to inositol trisphosphate and cyclic ADP-ribose. *J. Biol. Chem.* **270**, 2152–2157 (1995).
 17. H. C. Lee, T. F. Walseth, G. T. Bratt, R. N. Hayes, D. L. Clapper, Structural determination of a cyclic metabolite of NAD⁺ with intracellular Ca²⁺-mobilizing activity. *J. Biol. Chem.* **264**, 1608–1615 (1989).
 18. H. Hiltz, R. Koch, W. Fanick, K. Klapproth, P. Adamietz, Nonenzymic ADP-ribosylation of specific mitochondrial polypeptides. *Proc. Natl. Acad. Sci. U. S. A.* **81**, 3929–3933 (1984).
 19. A. Masmoudi, F. Islam, P. Mandel, ADP-Ribosylation of Highly Purified Rat Brain Mitochondria. *J. Neurochem.* **51**, 188–193 (1988).
 20. A. Masmoudi, P. Mandel, ADP-ribosyl NAD Activities. **10**, 1965–1969 (1987).
 21. T. Ono, A. Kasamatsu, S. Oka, J. Moss, The 39-kDa poly(ADP-ribose) glycohydrolase ARH3 hydrolyzes O-acetyl-ADP-ribose, a product of the Sir2 family of acetyl-histone deacetylases. *Proc. Natl. Acad. Sci. U. S. A.* **103**, 16687–16691 (2006).
 22. C. Mueller-Dieckmann, S. Kernstock, M. Lisurek, J. P. Von Kries, F. Haag, M. S. Weiss, F. Koch-Nolte, The structure of human ADP-ribosylhydrolase 3 (ARH3) provides insights into the reversibility of protein ADP-ribosylation. *Proc. Natl. Acad. Sci. U. S. A.* **103**, 15026–15031 (2006).
 23. M. Niere, M. Mashimo, L. Agledal, C. Dölle, A. Kasamatsu, J. Kato, J. Moss, M. Ziegler, ADP-ribosylhydrolase 3 (ARH3), not poly(ADP-ribose) glycohydrolase (PARG) isoforms, is responsible for degradation of mitochondrial matrix-associated poly(ADP-ribose). *J. Biol. Chem.* **287**, 16088–16102 (2012).
 24. T. V. Zharova, A. D. Vinogradov, A competitive inhibition of the mitochondrial NADH-ubiquinone oxidoreductase (Complex I) by ADP-ribose. *Biochim. Biophys. Acta - Bioenerg.* **1320**, 256–264 (1997).
 25. D. Bernet, R. M. Pinto, M. J. Costas, J. Canales, J. C. Cameselle, Rat liver mitochondrial ADP-ribose pyrophosphatase in the matrix space with low K_m for free ADP-ribose. *Biochem. J.* **299**, 679–682 (1994).
 26. S. Lin, L. Gasmi, Y. Xie, K. Ying, S. Gu, Z. Wang, H. Jin, Y. Chao, C. Wu, Z. Zhou, R. Tang, Y. Mao, A. G. McLennan, Cloning, expression and characterisation of a human Nudix hydrolase specific for adenosine 5'-diphosphoribose (ADP-ribose). *Biochim. Biophys. Acta - Protein Struct. Mol. Enzymol.* **1594**, 127–135 (2002).
 27. P. Bernardi, The mitochondrial permeability transition pore: A mystery solved? *Front. Physiol.* **4** MAY, 1–12 (2013).

7 REFERENCES

28. J. C. Amé, C. Spenlehauer, G. De Murcia, The PARP superfamily. *BioEssays*. **26**, 882–893 (2004).
29. D. D'Amours, S. Desnoyers, I. D'Silva, G. G. Poirier, Poly(ADP-ribosyl)ation reactions in the regulation of nuclear functions. *Biochem. J.* **342** (Pt 2, 249–68 (1999).
30. C. J. SKIDMORE, M. I. DAVIES, P. M. GOODWIN, H. HALLDORSSON, P. J. LEWIS, S. SHALL, A. -A ZIA'EE, The Involvement of Poly(ADP-ribose) Polymerase in the Degradation of NAD Caused by γ -Radiation and N-Methyl-N-Nitrosourea. *Eur. J. Biochem.* **101**, 135–142 (1979).
31. H. Juarez-Salinas, J. L. Sims, M. K. Jacobson, Poly(ADP-ribose) levels in carcinogen-treated cells. *Nature*. **282**, 740–741 (1979).
32. P. V Konarev, V. V Volkov, A. V Sokolova, M. H. J. Koch, D. I. Svergun, PRIMUS : a Windows PC-based system for small-angle scattering data analysis. *J. Appl. Crystallogr.* **36**, 1277–1282 (2003).
33. O. Leidecker, J. J. Bonfiglio, T. Colby, Q. Zhang, I. Atanassov, R. Zaja, L. Palazzo, A. Stockum, I. Ahel, I. Matic, Serine is a new target residue for endogenous ADP-ribosylation on histones. *Nat. Chem. Biol.* **12**, 998–1000 (2016).
34. K. Crawford, J. J. Bonfiglio, A. Mikoč, I. Matic, I. Ahel, Specificity of reversible ADP-ribosylation and regulation of cellular processes. *Crit. Rev. Biochem. Mol. Biol.* **53**, 64–82 (2018).
35. J. A. Tucker, N. Bennett, C. Brassington, S. T. Durant, G. Hassall, G. Holdgate, M. McAlister, J. W. M. Nissink, C. Truman, M. Watson, Structures of the Human Poly (ADP-Ribose) Glycohydrolase Catalytic Domain Confirm Catalytic Mechanism and Explain Inhibition by ADP-HPD Derivatives. *PLoS One*. **7**, e50889 (2012).
36. E. Barkauskaite, A. Brassington, E. S. Tan, J. Warwicker, M. S. Dunstan, B. Banos, P. Lafite, M. Ahel, T. J. Mitchison, I. Ahel, D. Leys, Visualization of poly(ADP-ribose) bound to PARG reveals inherent balance between exo- and endo-glycohydrolase activities. *Nat. Commun.* **4** (2013), doi:10.1038/ncomms3164.
37. D. Slade, M. S. Dunstan, E. Barkauskaite, R. Weston, P. Lafite, N. Dixon, M. Ahel, D. Leys, I. Ahel, The structure and catalytic mechanism of a poly(ADP-ribose) glycohydrolase. *Nature*. **477**, 616–620 (2011).
38. M. L. Meyer-Ficca, R. G. Meyer, D. L. Coyle, E. L. Jacobson, M. K. Jacobson, Human poly(ADP-ribose) glycohydrolase is expressed in alternative splice variants yielding isoforms that localize to different cell compartments. *Exp. Cell Res.* **297**, 521–532 (2004).
39. E. Winstall, E. B. Affar, R. Shah, S. Bourassa, I. A. Scovassi, G. G. Poirier, Preferential perinuclear localization of poly(ADP-ribose) glycohydrolase. *Exp. Cell Res.* **251**, 372–378 (1999).
40. V. Quarona, G. Zaccarello, A. Chillemi, E. Brunetti, V. K. Singh, E. Ferrero, A. Funaro, A. L. Horenstein, F. Malavasi, CD38 and CD157: A long journey from activation markers to multifunctional molecules. *Cytom. Part B Clin. Cytom.* **84B**, 207–217 (2013).

41. M. Howard, J. C. Grimaldi, J. F. Bazan, F. E. Lund, L. Santos-Argumedo, R. M. Parkhouse, T. F. Walseth, H. C. Lee, Formation and hydrolysis of cyclic ADP-ribose catalyzed by lymphocyte antigen CD38. *Science*. **262**, 1056–9 (1993).
42. S. Takasawa, A. Tohgo, N. Noguchi, T. Koguma, K. Nata, T. Sugimoto, H. Yonekura, H. Okamoto, Synthesis and hydrolysis of cyclic ADP-ribose by human leukocyte antigen CD38 and inhibition of the hydrolysis by ATP. *J. Biol. Chem.* **268**, 26052–26054 (1993).
43. R. H. G. Wright, A. Lioutas, F. Le Dily, D. Soronellas, A. Pohl, J. Bonet, A. S. Nacht, S. Samino, J. Font-Mateu, G. P. Vicent, M. Wierer, M. A. Trabado, C. Schelhorn, C. Carolis, M. J. Macias, O. Yanes, B. Oliva, M. Beato, ADP-ribose-derived nuclear ATP synthesis by NUDIX5 is required for chromatin remodeling. *Science*. **352**, 1221–5 (2016).
44. Q. Liu, I. A. Kriksunov, R. Graeff, C. Munshi, H. C. Lee, Q. Hao, Structural Basis for the Mechanistic Understanding of Human CD38-controlled Multiple Catalysis. *J. Biol. Chem.* **281**, 32861–32869 (2006).
45. D. G. Jackson, J. I. Bell, Isolation of a cDNA encoding the human CD38 (T10) molecule, a cell surface glycoprotein with an unusual discontinuous pattern of expression during lymphocyte differentiation. *J. Immunol.* **144**, 2811–5 (1990).
46. J. Camacho-Pereira, M. G. Tarragó, C. C. S. Chini, V. Nin, C. Escande, G. M. Warner, A. S. Puranik, R. A. Schoon, J. M. Reid, A. Galina, E. N. Chini, CD38 Dictates Age-Related NAD Decline and Mitochondrial Dysfunction through an SIRT3-Dependent Mechanism. *Cell Metab.* **23**, 1127–1139 (2016).
47. Y. J. Zhao, C. M. C. Lam, H. C. Lee, The Membrane-Bound Enzyme CD38 Exists in Two Opposing Orientations. *Sci. Signal.* **5**, ra67–ra67 (2012).
48. Y. Q. Shen, S. Y. Song, Z. J. Lin, Structures of D-glyceraldehyde-3-phosphate dehydrogenase complexed with coenzyme analogues. *Acta Crystallogr. Sect. D Biol. Crystallogr.* **58**, 1287–1297 (2002).
49. V. F. Lazarev, I. V. Guzhova, B. A. Margulis, Glyceraldehyde-3-phosphate dehydrogenase is a multifaceted therapeutic target. *Pharmaceutics*. **12** (2020), doi:10.3390/pharmaceutics12050416.
50. E. V. Koonin, A highly conserved sequence motif defining the family of mutT-related proteins from eubacteria, eukaryotes and viruses. *Nucleic Acids Res.* **21**, 4847 (1993).
51. A. G. McLennan, The MutT motif family of nucleotide phosphohydrolases in man and human pathogens (Review). *Int. J. Mol. Med.* **4**, 79–89 (1999).
52. M. J. Bessman, D. N. Frick, S. F. O’Handley, The MutT proteins or “Nudix” hydrolases, a family of versatile, widely distributed, “housecleaning” enzymes. *J. Biol. Chem.* **271** (1996), pp. 25059–25062.
53. A. S. Mildvan, Z. Xia, H. F. Azurmendi, V. Saraswat, P. M. Legler, M. A. Massiah, S. B. Gabelli, M. A. Bianchet, L. W. Kang, L. M. Amzel, Structures and mechanisms of Nudix hydrolases. *Arch. Biochem. Biophys.* **433**, 129–143 (2005).

54. S. B. Gabelli, M. A. Bianchet, M. J. Bessman, L. M. Amzel, The structure of adp-ribose pyrophosphatase reveals the structural basis for the versatility of the nudix family. *Nat. Struct. Biol.* **8**, 467–472 (2001).
55. J. Carreras-Puigvert, M. Zitnik, A. S. Jemth, M. Carter, J. E. Unterlass, B. Hallström, O. Loseva, Z. Karem, J. M. Calderón-Montanõ, C. Lindskog, P. H. Edqvist, D. J. Matuszewski, H. Ait Blal, R. P. A. Berntsson, M. Häggblad, U. Martens, M. Studham, B. Lundgren, C. Wählby, E. L. L. Sonnhammer, E. Lundberg, P. Stenmark, B. Zupan, T. Helleday, A comprehensive structural, biochemical and biological profiling of the human NUDIX hydrolase family. *Nat. Commun.* **8** (2017), doi:10.1038/s41467-017-01642-w.
56. T. Arimori, H. Tamaoki, T. Nakamura, H. Kamiya, S. Ikemizu, Y. Takagi, T. Ishibashi, H. Harashima, M. Sekiguchi, Y. Yamagata, Diverse substrate recognition and hydrolysis mechanisms of human NUDT5. *Nucleic Acids Res.* **39**, 8972–8983 (2011).
57. B. W. Shen, A. L. Perraud, A. Scharenberg, B. L. Stoddard, The crystal structure and mutational analysis of human NUDT9. *J. Mol. Biol.* **332**, 385–398 (2003).
58. L. Gasmi, J. L. Cartwright, A. G. M. C. Lennan, 5 h -diphosphosugar pyrophosphatase possessing a MutT motif. **337**, 331–337 (1999).
59. H. Yang, M. M. Slupska, Y. F. Wei, J. H. Tai, W. M. Luther, Y. R. Xia, D. M. Shih, J. H. Chiang, C. Baikalov, S. Fitz-Gibbon, I. T. Phan, A. Conrad, J. H. Miller, Cloning and characterization of a new member of the nudix hydrolases from human and mouse. *J. Biol. Chem.* **275**, 8844–8853 (2000).
60. R. H. G. Wright, A. Lioutas, F. Le Dily, D. Soronellas, A. Pohl, J. Bonet, A. S. Nacht, S. Samino, J. Font-Mateu, G. P. Vicent, M. Wierer, M. A. Trabado, C. Schelhorn, C. Carolis, M. J. Macias, O. Yanes, B. Oliva, M. Beato, ADP-ribose-derived nuclear ATP synthesis by NUDIX5 is required for chromatin remodeling. *Science.* **352**, 1221–5 (2016).
61. M. Zha, C. Zhong, Y. Peng, H. Hu, J. Ding, Crystal Structures of Human NUDT5 Reveal Insights into the Structural Basis of the Substrate Specificity. *J. Mol. Biol.* **364**, 1021–1033 (2006).
62. RCSB PDB - 3Q91: Crystal Structure of Human Uridine Diphosphate Glucose Pyrophosphatase (NUDT14), (available at <https://www.rcsb.org/structure/3Q91>).
63. S. R. Abdelraheim, D. G. Spiller, A. G. McLennan, Mammalian NADH diphosphatases of the Nudix family: Cloning and characterization of the human peroxisomal NUDT12 protein. *Biochem. J.* **374**, 329–335 (2003).
64. S. Y. Choi, J. H. Jang, K. R. Kim, Analysis of differentially expressed genes in human rectal carcinoma using suppression subtractive hybridization. *Clin. Exp. Med.* **11**, 219–226 (2011).
65. B. Yoon, E. G. Yang, S. Y. Kim, The ADP-ribose reactive NUDIX hydrolase isoforms can modulate HIF-1 α in cancer cells. *Biochem. Biophys. Res. Commun.* **504**, 321–327 (2018).
66. D. N. Li, C. C. Yang, J. Li, Q. G. Ou Yang, L. T. Zeng, G. Q. Fan, T. H. Liu, X. Y. Tian, J. J. Wang, H. Zhang, D. P. Dai, J. Cui, J. P. Cai, The high expression of MTH1 and NUDT5 promotes tumor metastasis and indicates a poor prognosis in patients with non-small-cell lung

- cancer. *Biochim. Biophys. Acta - Mol. Cell Res.* **1868**, 118895 (2021).
67. B. Tóth, I. Iordanov, L. Csanády, Ruling out pyridine dinucleotides as true TRPM2 channel activators reveals novel direct agonist ADP-ribose-2'-phosphate. *J. Gen. Physiol.* **145**, 419–430 (2015).
68. L. A. Rafty, M. T. Schmidt, A. L. Perraud, A. M. Scharenberg, J. M. Denu, Analysis of O-acetyl-ADP-ribose as a target for nudix ADP-ribose hydrolases. *J. Biol. Chem.* **277**, 47114–47122 (2002).
69. F. J. P. Kühn, J. M. Watt, B. V. L. Potter, A. Lückhoff, Different substrate specificities of the two ADPR binding sites in TRPM2 channels of *Nematostella vectensis* and the role of IDPR. *Sci. Rep.* **9**, 1–12 (2019).
70. A. L. Perraud, B. Shen, C. A. Dunn, K. Rippe, M. K. Smith, M. J. Bessman, B. L. Stoddard, A. M. Scharenberg, NUDT9, a member of the Nudix hydrolase family, is an evolutionarily conserved mitochondrial ADP-ribose pyrophosphatase. *J. Biol. Chem.* **278**, 1794–1801 (2003).
71. A. Carlotto, M. J. Costas, J. C. Cameselle, A. G. McLennan, J. M. Ribeiro, The specific, submicromolar-Km ADP-ribose pyrophosphatase purified from human placenta is enzymically indistinguishable from recombinant NUDT9 protein, including a selectivity for Mn²⁺ as activating cation and increase in Km for ADP-ribose, both elicited. *Biochim. Biophys. Acta - Gen. Subj.* **1760**, 1545–1551 (2006).
72. K. Nagamine, J. Kudoh, S. Minoshima, K. Kawasaki, S. Asakawa, F. Ito, N. Shimizu, Molecular cloning of a novel putative Ca²⁺ channel protein (TRPC7) highly expressed in brain. *Genomics.* **54**, 124–131 (1998).
73. X. Zhu, M. Jiang, M. Peyton, G. Boulay, R. Hurst, E. Stefani, L. Birnbaumer, trp, a novel mammalian gene family essential for agonist-activated capacitative Ca²⁺ entry. *Cell.* **85**, 661–671 (1996).
74. C. Zitt, A. Zobel, A. G. Obukhov, C. Harteneck, F. Kalkbrenner, A. Lückhoff, G. Schultz, Cloning and functional expression of a human Ca²⁺-permeable cation channel activated by calcium store depletion. *Neuron.* **16**, 1189–1196 (1996).
75. Y. Sano, K. Inamura, A. Miyake, S. Mochizuki, H. Yokoi, H. Matsushime, K. Furuichi, Immunocyte Ca²⁺ influx system mediated by LTRPC2. *Science.* **293**, 1327–30 (2001).
76. D. E. Clapham, TRP channels as cellular sensors. *Nature.* **426**, 517–524 (2003).
77. A. Fleig, R. Penner, The TRPM ion channel subfamily: Molecular, biophysical and functional features. *Trends Pharmacol. Sci.* **25** (2004), pp. 633–639.
78. F. J. P. Kühn, A. Lückhoff, Sites of the NUDT9-H domain critical for ADP-ribose activation of the cation channel TRPM2. *J. Biol. Chem.* **279**, 46431–46437 (2004).
79. R. Fliegert, J. M. Watt, A. Schöbel, M. D. Rozewitz, C. Moreau, T. Kirchberger, M. P. Thomas, W. Sick, A. C. Araujo, A. Harneit, B. V. L. Potter, A. H. Guse, Ligand-induced activation of human TRPM2 requires the terminal ribose of ADPR and involves Arg1433 and Tyr1349.

- Biochem. J.* **474**, 2159–2175 (2017).
80. B. Tóth, I. Iordanov, L. Csanády, Putative chanzyme activity of TRPM2 cation channel is unrelated to pore gating. *Proc. Natl. Acad. Sci. U. S. A.* **111**, 16949–16954 (2014).
 81. Y. Hara, M. Wakamori, M. Ishii, E. Maeno, M. Nishida, T. Yoshida, H. Yamada, S. Shimizu, E. Mori, J. Kudoh, N. Shimizu, H. Kurose, Y. Okada, K. Imoto, Y. Mori, LTRPC2 Ca²⁺-permeable channel activated by changes in redox status confers susceptibility to cell death. *Mol. Cell.* **9**, 163–73 (2002).
 82. E. Wehage, J. Einfeld, I. Heiner, E. Jüngling, C. Zitt, A. Lückhoff, Activation of the cation channel long transient receptor potential channel 2 (LTRPC2) by hydrogen peroxide: A splice variant reveals a mode of activation independent of ADP-ribose. *J. Biol. Chem.* **277**, 23150–23156 (2002).
 83. B. Buelow, Y. Song, A. M. Scharenberg, The Poly(ADP-ribose) Polymerase PARP-1 Is Required for Oxidative Stress-induced TRPM2 Activation in Lymphocytes. *J. Biol. Chem.* **283**, 24571–24583 (2008).
 84. B. Tóth, L. Csanády, Identification of direct and indirect effectors of the transient receptor potential melastatin 2 (TRPM2) cation channel. *J. Biol. Chem.* **285**, 30091–30102 (2010).
 85. Y. Huang, B. Roth, W. Lü, J. Du, Ligand recognition and gating mechanism through three Ligand-binding sites of human TRPM2 channel. *Elife.* **8**, 1–18 (2019).
 86. Y. Yin, M. Wu, A. L. Hsu, W. F. Borschel, M. J. Borgnia, G. C. Lander, S. Y. Lee, Visualizing structural transitions of ligand-dependent gating of the TRPM2 channel. *Nat. Commun.* **10**, 1–14 (2019).
 87. Y. Huang, P. A. Winkler, W. Sun, W. Lü, J. Du, Architecture of the TRPM2 channel and its activation mechanism by ADP-ribose and calcium. *Nature.* **562**, 145–149 (2018).
 88. F. J. P. Kühn, C. Kühn, A. Lückhoff, Functional characterisation of a TRPM2 orthologue from the sea anemone *Nematostella vectensis* in human cells. *Sci. Rep.* **5**, 8032 (2015).
 89. Z. Zhang, B. Tóth, A. Szollosi, J. Chen, L. Csanády, Structure of a TRPM2 channel in complex with Ca²⁺ explains unique gating regulation. *Elife.* **7**, 1–22 (2018).
 90. A. M. Peier, A. Moqrich, A. C. Hergarden, A. J. Reeve, D. A. Andersson, G. M. Story, T. J. Earley, I. Dragoni, P. McIntyre, S. Bevan, A. Patapoutian, A TRP channel that senses cold stimuli and menthol. *Cell.* **108**, 705–715 (2002).
 91. F. J. P. Kühn, K. Witschas, C. Kühn, A. Lückhoff, Contribution of the S5-pore-S6 domain to the gating characteristics of the cation channels TRPM2 and TRPM8. *J. Biol. Chem.* **285**, 26806–26814 (2010).
 92. B. Tóth, L. Csanády, Pore collapse underlies irreversible inactivation of TRPM2 cation channel currents. *Proc. Natl. Acad. Sci. U. S. A.* **109**, 13440–13445 (2012).
 93. T. Rohács, C. M. B. Lopes, I. Michailidis, D. E. Logothetis, PI(4,5)P₂ regulates the activation and desensitization of TRPM8 channels through the TRP domain. *Nat. Neurosci.* **8**, 626–634 (2005).

94. Y. Yin, S. C. Le, A. L. Hsu, M. J. Borgnia, H. Yang, S.-Y. Lee, Structural basis of cooling agent and lipid sensing by the cold-activated TRPM8 channel. *Science*. **363** (2019), doi:10.1126/science.aav9334.
95. L. Wang, T.-M. Fu, Y. Zhou, S. Xia, A. Greka, H. Wu, Structures and gating mechanism of human TRPM2. *Science*. **362** (2018), doi:10.1126/science.aav4809.
96. I. Iordanov, C. Mihályi, B. Tóth, L. Csanády, The proposed channel-enzyme transient receptor potential melastatin 2 does not possess ADP ribose hydrolase activity. *Elife*. **5**, 1–20 (2016).
97. Y. Huang, R. Fliegert, A. H. Guse, W. Lü, J. Du, A structural overview of the ion channels of the TRPM family. *Cell Calcium*. **85**, 102111 (2020).
98. J. Starkus, A. Beck, A. Fleig, R. Penner, Regulation of TRPM2 by extra- and intracellular calcium. *J. Gen. Physiol.* **130**, 427–440 (2007).
99. D. McHugh, R. Flemming, S. Z. Xu, A. L. Perraud, D. J. Beech, Critical intracellular Ca²⁺ dependence of transient receptor potential melastatin 2 (TRPM2) cation channel activation. *J. Biol. Chem.* **278**, 11002–11006 (2003).
100. I. Heiner, J. Einfeld, M. Warnstedt, N. Radukina, E. Jüngling, A. Lückhoff, Endogenous ADP-ribose enables calcium-regulated cation currents through TRPM2 channels in neutrophil granulocytes. *Biochem. J.* **398**, 225–232 (2006).
101. L. Csanády, B. Töröcsik, Four Ca²⁺ Ions Activate TRPM2 channels by binding in deep crevices near the pore but intracellularly of the gate. *J. Gen. Physiol.* **133**, 189–203 (2009).
102. Y. Huang, B. Roth, W. Lü, J. Du, Ligand recognition and gating mechanism through three Ligand-binding sites of human TRPM2 channel. *Elife*. **8**, 1–18 (2019).
103. H. E. Autzen, A. G. Myasnikov, M. G. Campbell, D. Asarnow, D. Julius, Y. Cheng, Structure of the human TRPM4 ion channel in a lipid nanodisc. *Science*. **359**, 228–232 (2018).
104. S. Yamaguchi, A. Tanimoto, S. Iwasa, K. I. Otsuguro, TRPM4 and TRPM5 channels share crucial amino acid residues for Ca²⁺ sensitivity but not significance of Pi(4,5)p₂. *Int. J. Mol. Sci.* **20** (2019), doi:10.3390/ijms20082012.
105. E. Pidcock, G. R. Moore, Structural characteristics of protein binding sites for calcium and lanthanide ions. *J. Biol. Inorg. Chem.* **6**, 479–89 (2001).
106. J. L. Gifford, M. P. Walsh, H. J. Vogel, Structures and metal-ion-binding properties of the Ca²⁺-binding helix-loop-helix EF-hand motifs. *Biochem. J.* **405**, 199–221 (2007).
107. Y. Luo, X. Yu, C. Ma, J. Luo, W. Yang, Identification of a novel EF-loop in the N-terminus of TRPM2 channel involved in calcium sensitivity. *Front. Pharmacol.* **9**, 1–15 (2018).
108. Q. Tong, W. Zhang, K. Conrad, K. Mostoller, J. Y. Cheung, B. Z. Peterson, B. A. Miller, Regulation of the transient receptor potential channel TRPM2 by the Ca²⁺ sensor calmodulin. *J. Biol. Chem.* **281**, 9076–9085 (2006).
109. T. Rohacs, B. Nilius, Regulation of transient receptor potential (TRP) channels by

- phosphoinositides. *Pflugers Arch. Eur. J. Physiol.* **455**, 157–168 (2007).
110. H. Wang, J. Siemens, TRP ion channels in thermosensation, thermoregulation and metabolism. *Temperature.* **2**, 178–187 (2015).
 111. K. Togashi, Y. Hara, T. Tominaga, T. Higashi, Y. Konishi, Y. Mori, M. Tominaga, TRPM2 activation by cyclic ADP-ribose at body temperature is involved in insulin secretion. *EMBO J.* **25**, 1804–1815 (2006).
 112. K. Song, H. Wang, G. B. Kamm, J. Pohle, F. de C. Reis, P. Heppenstall, H. Wende, J. Siemens, The TRPM2 channel is a hypothalamic heat sensor that limits fever and can drive hypothermia. *Science.* **353**, 1393–1398 (2016).
 113. C.-H. Tan, P. A. McNaughton, The TRPM2 ion channel is required for sensitivity to warmth. *Nature.* **536**, 460–3 (2016).
 114. M. Kashio, T. Sokabe, K. Shintaku, T. Uematsu, N. Fukuta, N. Kobayashi, Y. Mori, M. Tominaga, Redox signal-mediated sensitization of transient receptor potential melastatin 2 (TRPM2) to temperature affects macrophage functions. *Proc. Natl. Acad. Sci. U. S. A.* **109**, 6745–6750 (2012).
 115. O. Grubisha, L. A. Rafty, C. L. Takanishi, X. Xu, L. Tong, A. L. Perraud, A. M. Scharenberg, J. M. Denu, Metabolite of SIR2 reaction modulates TRPM2 ion channel. *J. Biol. Chem.* **281**, 14057–14065 (2006).
 116. R. Fliegert, A. Bauche, A.-M. Wolf Pérez, J. M. Watt, M. D. Rozewitz, R. Winzer, M. Janus, F. Gu, A. Rosche, A. Harneit, M. Flato, C. Moreau, T. Kirchberger, V. Wolters, B. V. L. Potter, A. H. Guse, 2'-Deoxyadenosine 5'-diphosphoribose is an endogenous TRPM2 superagonist. *Nat. Chem. Biol.* **13**, 1036–1044 (2017).
 117. R. Aarhus, R. M. Graeff, D. M. Dickey, T. F. Walseth, C. L. Hon, ADP-ribosyl Cyclase and CD38 Catalyze the Synthesis of a Calcium-mobilizing Metabolite from NADP⁺. *J. Biol. Chem.* **270**, 30327–30333 (1995).
 118. F. Schmid, S. Bruhn, K. Weber, H.-W. Mittrücker, A. H. Guse, CD38: A NAADP degrading enzyme. *FEBS Lett.* **585**, 3544–3548 (2011).
 119. J. Chen, R. A. Chaurio, C. Maueröder, A. Derer, M. Rauh, A. Kost, Y. Liu, X. Mo, A. Hueber, R. Bilyy, M. Herrmann, Y. Zhao, L. E. Muñoz, Inosine released from dying or dead cells stimulates cell proliferation via adenosine receptors. *Front. Immunol.* **8** (2017), doi:10.3389/fimmu.2017.00504.
 120. A. H. Guse, C. P. Da Silva, I. Berg, A. L. Skapenko, K. Weber, P. Heyer, M. Hohenegger, G. A. Ashamu, H. Schulze-Koops, B. V. L. Potter, G. W. Mayr, Regulation of calcium signalling in T lymphocytes by the second messenger cyclic ADP-ribose. *Nature.* **398**, 70–73 (1999).
 121. A. H. Guse, I. Berg, C. P. Da Silva, B. V. L. Potter, G. W. Mayr, Ca²⁺ entry induced by cyclic ADP-ribose in intact T-lymphocytes. *J. Biol. Chem.* **272**, 8546–8550 (1997).
 122. M. Kolisek, A. Beck, A. Fleig, R. Penner, Cyclic ADP-ribose and hydrogen peroxide synergize with ADP-ribose in the activation of TRPM2 channels. *Mol. Cell.* **18**, 61–69 (2005).

7 REFERENCES

123. R. Fliegert, W. M. Riekehr, A. H. Guse, Does Cyclic ADP-Ribose (cADPR) Activate the Non-selective Cation Channel TRPM2? *Front. Immunol.* **11**, 1–6 (2020).
124. P. Yu, Z. Liu, X. Yu, P. Ye, H. Liu, X. Xue, L. Yang, Z. Li, Y. Wu, C. Fang, Y. J. Zhao, F. Yang, J. H. Luo, L. H. Jiang, L. Zhang, L. Zhang, W. Yang, Direct Gating of the TRPM2 Channel by cADPR via Specific Interactions with the ADPR Binding Pocket. *Cell Rep.* **27**, 3684-3695.e4 (2019).
125. S. Partida-Sanchez, A. Gasser, R. Fliegert, C. C. Siebrands, W. Dammermann, G. Shi, B. J. Mousseau, A. Sumoza-Toledo, H. Bhagat, T. F. Walseth, A. H. Guse, F. E. Lund, Chemotaxis of Mouse Bone Marrow Neutrophils and Dendritic Cells Is Controlled by ADP-Ribose, the Major Product Generated by the CD38 Enzyme Reaction. *J. Immunol.* **179**, 7827–7839 (2007).
126. K. Uchida, K. Dezaki, B. Damdindorj, H. Inada, T. Shiuchi, Y. Mori, T. Yada, Y. Minokoshi, M. Tominaga, Lack of TRPM2 impaired insulin secretion and glucose metabolisms in mice. *Diabetes.* **60**, 119–126 (2011).
127. F. Kühn, C. Kühn, A. Lückhoff, Different principles of ADP-ribose-mediated activation and opposite roles of the NUDT9 homology domain in the TRPM2 orthologs of man and sea anemone. *Front. Physiol.* **8**, 1–14 (2017).
128. B. Tóth, I. Iordanov, L. Csanády, Selective profiling of N- And C-terminal nucleotide-binding sites in a TRPM2 channel. *J. Gen. Physiol.* **152**, 1–13 (2020).
129. F. J. P. Kühn, Structure-Function Relationship of TRPM2: Recent Advances, Contradictions, and Open Questions. *Int. J. Mol. Sci.* **21**, 1–17 (2020).
130. T. J. Lambert, FPbase: a community-editable fluorescent protein database. *Nat. Methods.* **16**, 277–278 (2019).
131. R. Arai, H. Ueda, A. Kitayama, N. Kamiya, T. Nagamune, Design of the linkers which effectively separate domains of a bifunctional fusion protein. *Protein Eng.* **14**, 529–532 (2001).
132. N. Panchuk-Voloshina, R. P. Haugland, J. Bishop-Stewart, M. K. Bhalgat, P. J. Millard, F. Mao, W. Y. Leung, R. P. Haugland, Alexa dyes, a series of new fluorescent dyes that yield exceptionally bright, photostable conjugates. *J. Histochem. Cytochem.* **47**, 1179–1188 (1999).
133. S. B. Gabelli, M. A. Bianchet, Y. Ohnishi, Y. Ichikawa, M. J. Bessman, L. M. Amzel, Mechanism of the Escherichia coli ADP-ribose pyrophosphatase, a Nudix hydrolase. *Biochemistry.* **41**, 9279–9285 (2002).
134. M. J. Kadhim, M. I. Gamaj, Short Review Article Estimation of the Diffusion Coefficient and Hydrodynamic Radius (Stokes Radius) for Inorganic Ions in Solution Depending on Molar Conductivity as Electro-Analytical Technique-A Review. **2**, 182–188 (2020).
135. R. D. Shannon, Revised effective ionic radii and systematic studies of interatomic distances in halides and chalcogenides. *Acta Crystallogr. Sect. A.* **32**, 751–767 (1976).
136. F. J. P. Kühn, C. Kühn, M. Winking, D. C. Hoffmann, A. Lückhoff, ADP-Ribose activates the

- trpm2 channel from the sea anemone *Nematostella vectensis* independently of the nudt9h domain. *PLoS One*. **11**, 1–21 (2016).
137. I. Iordanov, C. Mihályi, B. Tóth, L. Csanády, The proposed channel-enzyme transient receptor potential melastatin 2 does not possess ADP ribose hydrolase activity. *Elife*. **5**, 1–20 (2016).
 138. L. Lindenburg, M. Merckx, Engineering genetically encoded FRET sensors. *Sensors (Switzerland)*. **14**, 11691–11713 (2014).
 139. J. Y. Jiang, J. L. Falcone, S. Curci, A. M. Hofer, Interrogating cyclic AMP signaling using optical approaches. *Cell Calcium*. **64**, 47–56 (2017).
 140. E. A. Rodriguez, R. E. Campbell, J. Y. Lin, M. Z. Lin, A. Miyawaki, A. E. Palmer, X. Shu, J. Zhang, R. Y. Tsien, The Growing and Glowing Toolbox of Fluorescent and Photoactive Proteins. *Trends Biochem. Sci.* **42**, 111–129 (2017).
 141. H. W. Ai, J. N. Henderson, S. J. Remington, R. E. Campbell, Directed evolution of a monomeric, bright and photostable version of *Clavularia cyan* fluorescent protein: Structural characterization and applications in fluorescence imaging. *Biochem. J.* **400**, 531–540 (2006).
 142. T. Nagai, K. Ibata, E. S. Park, M. Kubota, K. Mikoshiba, A. Miyawaki, A variant of yellow fluorescent protein with fast and efficient maturation for cell-biological applications. *Nat. Biotechnol.* **20**, 87–90 (2002).
 143. T. H. Evers, E. M. W. M. Van Dongen, A. C. Faesen, E. W. Meijer, M. Merckx, Quantitative understanding of the energy transfer between fluorescent proteins connected via flexible peptide linkers. *Biochemistry*. **45**, 13183–13192 (2006).
 144. R. Arai, W. Wriggers, Y. Nishikawa, T. Nagamune, T. Fujisawa, Conformations of variably linked chimeric proteins evaluated by synchrotron X-ray small-angle scattering. *Proteins Struct. Funct. Genet.* **57**, 829–838 (2004).
 145. G. S. Baird, D. A. Zacharias, R. Y. Tsien, Circular permutation and receptor insertion within green fluorescent proteins. *Proc. Natl. Acad. Sci. U. S. A.* **96**, 11241–11246 (1999).
 146. R. D. Fritz, M. Letzelter, A. Reimann, K. Martin, L. Fusco, L. Ritsma, B. Ponsioen, E. Fluri, S. Schulte-Merker, J. Van Rheenen, O. Pertz, A versatile toolkit to produce sensitive FRET biosensors to visualize signaling in time and space. *Sci. Signal.* **6**, 1–14 (2013).
 147. H. Chen, S. S. Ahsan, M. B. Santiago-Berrios, H. D. Abruña, W. W. Webb, Mechanisms of quenching of alexa fluorophores by natural amino acids. *J. Am. Chem. Soc.* **132**, 7244–7245 (2010).
 148. L. E. Jansen, L. J. Negrón-Piñeiro, S. Galarza, S. R. Peyton, Control of Thiol-Maleimide Reaction Kinetics in PEG Hydrogel Networks. *bioRxiv*. **1133**, 120–128 (2017).
 149. M. Suzuki, S. Tanaka, Y. Ito, M. Inoue, T. Sakai, K. Nishigaki, Simple and tunable Förster resonance energy transfer-based bioprobes for high-throughput monitoring of caspase-3 activation in living cells by using flow cytometry. *Biochim. Biophys. Acta - Mol. Cell Res.*

- 1823**, 215–226 (2012).
150. A. Binolfi, A. Limatola, S. Verzini, J. Kosten, F. X. Theillet, H. May Rose, B. Bekei, M. Stuiver, M. Van Rossum, P. Selenko, Intracellular repair of oxidation-damaged α -synuclein fails to target C-terminal modification sites. *Nat. Commun.* **7** (2016), doi:10.1038/ncomms10251.
 151. F. X. Theillet, A. Binolfi, B. Bekei, A. Martorana, H. M. Rose, M. Stuiver, S. Verzini, D. Lorenz, M. Van Rossum, D. Goldfarb, P. Selenko, Structural disorder of monomeric α -synuclein persists in mammalian cells. *Nature.* **530**, 45–50 (2016).
 152. R. Todorova, Estimation of methods of protein delivery into mammalian cells - A comparative study by electroporation and Bioporter assay. *Appl. Biochem. Microbiol.* **45**, 444–448 (2009).
 153. O. Zelphati, Y. Wang, S. Kitada, J. C. Reed, P. L. Felgner, J. Corbeil, Intracellular Delivery of Proteins with a New Lipid-mediated Delivery System. *J. Biol. Chem.* **276**, 35103–35110 (2001).
 154. G. W. Gordon, G. Berry, X. H. Liang, B. Levine, B. Herman, Using Fluorescence Microscopy. **74**, 2702–2713 (1998).
 155. M. A. Schumacher, M. Crum, M. C. Miller, Crystal structures of apocalmodulin and an apocalmodulin/SK potassium channel gating domain complex. *Structure.* **12**, 849–860 (2004).
 156. D. Vinayagam, D. Quentin, O. Sitsel, F. Merino, M. Stabrin, O. Hofnagel, M. Yu, M. W. Ledebor, G. Malojcic, S. Raunser, Structural basis of TRPC4 regulation by calmodulin and pharmacological agents. *bioRxiv*, 1–26 (2020).
 157. T. E. T. Hughes, R. A. Pumroy, A. T. Yazici, M. A. Kasimova, E. C. Fluck, K. W. Huynh, A. Samanta, S. K. Molugu, Z. H. Zhou, V. Carnevale, T. Rohacs, V. Y. Moiseenkova-Bell, Structural insights on TRPV5 gating by endogenous modulators. *Nat. Commun.* **9**, 1–11 (2018).
 158. F. M. Bokhovchuk, N. Bate, N. V. Kovalevskaya, B. T. Goult, C. A. E. M. Spronk, G. W. Vuister, The Structural Basis of Calcium-Dependent Inactivation of the Transient Receptor Potential Vanilloid 5 Channel. *Biochemistry.* **57**, 2623–2635 (2018).
 159. S. Linse, A. Helmersson, S. Forsen, Calcium binding to calmodulin and its globular domains. *J. Biol. Chem.* **266**, 8050–8054 (1991).
 160. E. Fonfria, I. C. B. Marshall, C. D. Benham, I. Boyfield, J. D. Brown, K. Hill, J. P. Hughes, S. D. Skaper, S. McNulty, TRPM2 channel opening in response to oxidative stress is dependent on activation of poly(ADP-ribose) polymerase. *Br. J. Pharmacol.* **143**, 186–192 (2004).
 161. H. Nam Tran, J. Hederih, T. Numata, M. X. Mori, S. Maegawa, H. Hosokawa, Y. Mori, Functional Characterization of Zebrafish Transient Receptor Potential Melastatin 2. *Biophys. J.* **114**, 641a-642a (2018).
 162. L. Stryer, Fluorescence Energy Transfer as a Spectroscopic Ruler. *Annu. Rev. Biochem.* **47**, 819–846 (1978).

163. L. Stryer, R. P. Haugland, Energy transfer: a spectroscopic ruler. *Proc. Natl. Acad. Sci.* **58**, 719–726 (1967).
164. T. Förster, Zwischenmolekulare Energiewanderung und Fluoreszenz. *Ann. Phys.* **437**, 55–75 (1948).
165. T. Förster, 10th Spiers Memorial Lecture. Transfer mechanisms of electronic excitation. *Discuss. Faraday Soc.* **27**, 7–17 (1959).
166. C. G. Dos Remedios, P. D. J. Moens, Fluorescence resonance energy transfer spectroscopy is a reliable “ruler” for measuring structural changes in proteins. Dispelling the problem of the unknown orientation factor. *J. Struct. Biol.* **115** (1995), pp. 175–185.
167. R. E. Campbell, Fluorescent-Protein-Based Biosensors: Modulation of Energy Transfer as a Design Principle. *Anal. Chem.* **81**, 5972–5979 (2009).
168. W. Kabsch, XDS. *Acta Crystallogr. Sect. D Biol. Crystallogr.* **66**, 125–132 (2010).
169. P. Evans, Scaling and assessment of data quality. *Acta Crystallogr. Sect. D Biol. Crystallogr.* **62**, 72–82 (2006).
170. P. Emsley, K. Cowtan, Coot : model-building tools for molecular graphics. *Acta Crystallogr. Sect. D Biol. Crystallogr.* **60**, 2126–2132 (2004).
171. M. A. Graewert, D. I. Svergun, Impact and progress in small and wide angle X-ray scattering (SAXS and WAXS). *Curr. Opin. Struct. Biol.* **23**, 748–754 (2013).
172. S. Skou, R. E. Gillilan, N. Ando, Synchrotron-based small-angle X-ray scattering of proteins in solution. *Nat. Protoc.* **9**, 1727–1739 (2014).
173. H. D. T. Mertens, D. I. Svergun, Structural characterization of proteins and complexes using small-angle X-ray solution scattering. *J. Struct. Biol.* **172**, 128–141 (2010).
174. G. L. Hura, A. L. Menon, M. Hammel, R. P. Rambo, F. L. Poole, S. E. Tsutakawa, F. E. Jenney, S. Classen, K. A. Frankel, R. C. Hopkins, S. J. Yang, J. W. Scott, B. D. Dillard, M. W. W. Adams, J. A. Tainer, Robust, high-throughput solution structural analyses by small angle X-ray scattering (SAXS). *Nat. Methods.* **6**, 606–612 (2009).
175. C. E. Blanchet, A. Spilotros, F. Schwemmer, M. A. Graewert, A. Kikhney, C. M. Jeffries, D. Franke, D. Mark, R. Zengerle, F. Cipriani, S. Fiedler, M. Roessle, D. I. Svergun, Versatile sample environments and automation for biological solution X-ray scattering experiments at the P12 beamline (PETRA III, DESY). *J. Appl. Crystallogr.* **48**, 431–443 (2015).
176. B. Jacrot, The study of biological structures by neutron scattering from solution. *Reports Prog. Phys.* **39**, 911–953 (1976).
177. D. I. Svergun, Determination of the regularization parameter in indirect-transform methods using perceptual criteria. *J. Appl. Crystallogr.* **25**, 495–503 (1992).
178. S. A. Rice, Small angle scattering of X-rays. A. Guinier and G. Fournet. Translated by C. B. Wilson and with a bibliographical appendix by K. L. Yudowitch. Wiley, New York, 1955. 268 pp. \$7.50. *J. Polym. Sci.* **19**, 594–594 (1956).

7 REFERENCES

179. D. I. Svergun, M. H. J. Koch, Small-angle scattering studies of biological macromolecules in solution. *Reports Prog. Phys.* **66**, 1735–1782 (2003).
180. A. Guinier, The diffusion of X-rays under the extremely weak angles applied to the study of fine particles and colloidal suspension. *C. R. Hebd. Seances Acad. Sci.*, 1374–1376 (1938).
181. E. Lescop, P. Schanda, B. Brutscher, A set of BEST triple-resonance experiments for time-optimized protein resonance assignment. *J. Magn. Reson.* **187**, 163–169 (2007).
182. W. Lee, M. Tonelli, J. L. Markley, NMRFAM-SPARKY: Enhanced software for biomolecular NMR spectroscopy. *Bioinformatics.* **31**, 1325–1327 (2015).
183. J. Schindelin, I. Arganda-Carreras, E. Frise, V. Kaynig, M. Longair, T. Pietzsch, S. Preibisch, C. Rueden, S. Saalfeld, B. Schmid, J. Y. Tinevez, D. J. White, V. Hartenstein, K. Eliceiri, P. Tomancak, A. Cardona, Fiji: An open-source platform for biological-image analysis. *Nat. Methods.* **9**, 676–682 (2012).
184. A. Mollemann, in *Patch Clamping: An Introductory Guide To Patch Clamp Electrophysiology* (2003), pp. 5–42.
185. B. Sakmann, E. Neher, Patch clamp techniques for studying ionic channels in excitable membranes. *Annu. Rev. Physiol.* **VOL. 46**, 455–472 (1984).
186. F. J. Sigworth, E. Neher, Single Na⁺ channel currents observed in cultured rat muscle cells. *Nature.* **287**, 447–449 (1980).

8 Safety and Disposal

8.1 GHS hazards statements

H225	Highly flammable liquid and vapor
H226	Flammable liquid and vapor
H228	Flammable solid
H272	May intensify fire; oxidizer
H290	May be corrosive to metals
H301	Toxic if swallowed
H302	Harmful if swallowed
H303	May be harmful if swallowed
H311	Toxic in contact with skin
H312	Harmful in contact with skin
H313	May be harmful in contact with skin
H314	Causes severe skin burns and eye damage
H315	Causes skin irritation
H316	Causes mild skin irritation
H317	May cause an allergic skin reaction
H318	Causes serious eye damage
H319	Causes serious eye irritation
H330	Fatal if inhaled
H331	Toxic if inhaled
H332	Harmful if inhaled
H333	May be harmful if inhaled
H334	May cause allergy or asthma symptoms or breathing difficulties if inhaled
H335	May cause respiratory irritation
H336	May cause drowsiness or dizziness
H340	May cause genetic defects
H341	Suspected of causing genetic defects
H350	May cause cancer
H350i	May cause cancer by inhalation
H360	May damage fertility or the unborn child
H360D	May damage the unborn child
H360F	May damage fertility
H360Fd	May damage fertility. Suspected of damaging the unborn child
H360FD	May damage fertility. May damage the unborn child
H361	Suspected of damaging fertility or the unborn child
H361d	Suspected of damaging the unborn child.
H361f	Suspected of damaging fertility
H370	Cause damage to organs

H372	Causes damage to organs through prolonged or repeated exposure
H373	May cause damage to organs through prolonged or repeated exposure.
H400	Very toxic to aquatic life with long-lasting effects
H410	Very toxic to aquatic life with long lasting effects
H411	Toxic to aquatic life with long lasting effects
H412	Harmful to aquatic life with long lasting effects.
EUH032	Contact with acids liberates very toxic gas
EUH066	Repeated exposure may cause skin dryness or cracking

8.2 GHS precautional statements

P101	If medical advice is needed, have product container or label at hand
P201	Obtain special instructions before use
P210	Keep away from heat/sparks/open flames/hot surfaces – No smoking
P233	Keep container tightly closed
P260	Do not breathe dust/fume/gas/mist/vapours/spray
P261	Avoid breathing dust/fume/gas/mist/vapours/spray
P264	Wash thoroughly after handling
P270	Do not eat, drink or smoke when using this product
P273	Avoid release to the environment
P281	Use personal protective equipment as required
P280	Wear protective gloves/protective clothing/eye protection/face protection
P284	Wear respiratory protection
P309	IF exposed or you feel unwell
P310	Immediately call a POISON CENTER or doctor/physician
P311	Call a POISON CENTER or doctor/physician
P312	Call a POISON CENTER or doctor/physician if you feel unwell
P321	Specific treatment (see respective MSDS)
P330	Rinse mouth
P362	Take off contaminated clothing and wash before reuse
P391	Collect spillage
P405	Store locked up
P501	Dispose of contents/container in accordance with local/regional/national/ international regulations
P301+P310	IF SWALLOWED: Immediately call a POISON CENTER or doctor/physician
P301+P312	IF SWALLOWED: Call a POISON CENTER or doctor/physician if you feel unwell
P301+P330+P331	IF SWALLOWED: Rinse mouth. Do NOT induce vomiting
P302+P352	IF ON SKIN: Wash with soap and water
P303+P361+P353	IF ON SKIN (or hair): Remove/Take off immediately all contaminated clothing. Rinse skin with water/shower
P304+P341	IF INHALED: If breathing is difficult, remove victim to fresh air and keep at rest in a position comfortable for breathing

P305+P351+P338	IF IN EYES: Rinse cautiously with water for several minutes. Remove contact lenses if present and easy to do - continue rinsing
P308+P313	IF exposed or concerned: Get medical advice/attention
P309+P311	IF exposed or you feel unwell: Call a POISON CENTER or doctor/physician
P332+P313	If skin irritation occurs: Get medical advice/attention
P333+P313	If skin irritation or rash occurs: Get medical advice/attention
P337+P313	If eye irritation persists: Get medical advice/attention
P342+P311	Call a POISON CENTER or doctor/physician
P370+P378	In case of fire: Use for extinction: Alcohol resistant foam
P370+P378	In case of fire: Use for extinction: Fire-extinguishing powder
P370+P378	In case of fire: Use for extinction: Carbon dioxide
P403+P233	Store in a well-ventilated place. Keep container tightly closed
P403+P235	Store in a well-ventilated place. Keep cool

8.3 Disposal

All chemicals used during the experiments were handled and disposed according to their GHS safety and precautionary statements. Solvents and contaminated waste were stored in the indicated boxes and disposed according to the safety instructions. Genetically modified organisms and related waste were autoclaved according to the “Gentechnikgesetz” before disposal for 20 min at 121°C and 5 bar.

9 Appendix

9.1 NMR backbone resonance assignment of NUdT9trC_{W339} RIL/ADPR

All assigned backbone resonances obtained from TROSY-based 3D HN(CA)CO, HNCO, HNCA, HN(CO)CA, C β -optimized HNCACB and HN(CO)CACB spectra are listed in Table 9-1. NMR assignment data have been deposited to the Biological Magnetic Resonance Data Bank (BMRB) with accession code 50870.

Table 9-1: Assigned NMR backbone resonances of the NUdT9trC_{W339}-RIL/ADPR complex.

no.	amino acid	ω				
		H	C	C α	C β	N
61	SER	8.082	174.312	57.521	63.477	116.578
62	HIS	8.461	174.626	55.194	30.383	121.252
63	ASN	9.403	176.896	54.767	41.285	121.913
64	LYS	10.285	180.813	58.433	29.296	127.190
65	ALA	9.454	173.362	52.808	18.084	123.931

9 APPENDIX

no.	amino acid	ω				
		H	C	C α	C β	N
66	ARG	6.698	176.513	54.456	30.150	109.651
67	THR	7.532	173.423	64.524	70.266	116.650
68	SER	8.474	173.129	55.388	65.223	121.457
71	PRO		174.927	64.369	30.965	
72	GLY	8.441	173.902	45.320		110.185
73	SER	8.369	172.623	57.056	68.132	117.714
74	LYS	8.477	176.917	54.127	30.965	117.565
75	VAL	8.492	174.859	63.166	31.120	125.044
76	GLU	8.174	177.094	54.806	29.025	127.424
77	ARG	8.126	178.188	55.620	31.042	121.744
78	SER	8.777	174.148	58.996	62.119	119.500
79	GLN	8.696	176.329	56.959	28.210	125.385
80	VAL	8.616	173.232	58.879	33.370	126.365
83	GLU	9.402	176.773	57.948	27.473	116.631
84	LYS	7.625	174.558	53.719	32.982	117.367
85	VAL	6.873	176.322	65.785	31.585	120.789
86	GLY	8.075	175.570	45.688		103.708
87	TRP	7.683	177.245	58.569	29.335	123.571
88	LEU	8.017	178.188	55.640	40.354	115.930
89	VAL	7.759	175.160	62.138	30.616	122.976
90	GLU	8.498	176.424	56.939	29.219	129.548
91	TRP	9.313	175.720	53.855	27.279	127.184
93	ASP	7.952	174.250	52.963	39.306	114.807
94	TYR	6.226	174.941	56.707	36.940	121.241
95	LYS	8.221	172.343	52.691	31.818	131.780
96	PRO		175.754	61.750	31.236	
97	VAL	7.078	173.970	60.936	32.788	121.085
98	GLU	8.380	176.151	54.806	29.723	127.033
99	TYR	9.110	173.574	58.821	40.780	128.064
100	THR	7.316	170.573	61.867	71.236	124.225
101	ALA	8.172	179.254	51.411	19.248	128.199
102	VAL	8.696	177.853	65.708	30.810	121.164
103	SER	7.905	175.874	59.772	61.343	112.551
104	VAL	6.738	179.521	64.738	31.508	122.472
105	LEU	7.760	177.703	56.183	40.392	121.317
106	ALA	7.369	177.648	52.594	17.425	119.275
107	GLY	7.293	171.810	47.318		106.534
110	TRP	6.146	174.011	52.827	29.025	112.698
111	ALA	7.031	177.539	48.928	20.761	120.310
112	ASP	7.873	175.228	53.254	42.177	120.135
113	PRO		175.440	61.731	30.460	
114	GLN	8.399	176.999	57.250	29.296	116.903
115	ILE	7.299	175.604	61.110	37.017	120.886
116	SER	7.753	174.743	57.657	62.623	113.121
117	GLU	7.597	177.833	56.901	28.908	124.806
118	SER	8.632	175.854	60.257	62.507	121.534
119	ASN	8.639	174.254	53.390	37.405	117.608

9 APPENDIX

no.	amino acid	ω				
		H	C	C α	C β	N
120	PHE	7.732	173.963	55.407	38.491	122.041
121	SER	8.709		53.487	62.468	125.121
122	PRO		176.390	61.033	29.452	
123	LYS	7.874	174.702	52.691	29.452	124.405
124	PHE	7.300	175.932	59.500	38.026	117.516
125	ASN	7.776	171.721	56.610	36.823	107.042
126	GLU	7.293	174.408	54.844	33.137	115.157
127	LYS	8.423	174.654	57.541	31.081	121.207
128	ASP	8.963	176.233	50.810	41.207	131.641
129	GLY	8.534	174.709	46.736		115.206
131	VAL	7.864	174.626	61.906	32.167	122.950
132	GLU	9.019	175.707	55.698	28.521	130.328
133	ARG	7.919	178.222	55.000	28.171	126.061
134	LYS	8.953	178.373	57.871	31.042	124.476
135	SER	9.677	177.286	56.280	63.632	120.016
136	LYS	11.332	177.422	57.269	31.624	130.544
137	ASN	8.797	174.196	53.506	40.276	116.696
138	GLY	7.363	173.628	43.904		107.407
139	LEU	8.353	177.641	55.426	42.100	122.001
140	TYR	8.318	175.877	53.933	39.539	120.240
141	GLU	9.284	174.572	55.446	30.460	122.519
142	ILE	8.202	175.802	58.511	36.784	120.997
148	ARG	8.225	175.262	54.146	32.090	122.011
149	ASN	8.863	174.442	50.693	37.832	126.213
150	PRO		177.327	63.574	31.353	
151	ALA	8.178	177.299	51.857	17.657	121.979
152	GLY	7.031	171.448	43.128		105.906
153	ARG	8.244	179.316	56.998	31.314	115.674
154	THR	10.174	177.122	61.401	70.499	111.783
156	LEU	7.746	174.606	54.631	47.570	125.058
157	VAL	9.548	175.891	59.636	33.797	121.091
158	GLY	8.706	174.647	43.496		104.997
159	ARG	7.298	175.925	56.222	31.857	118.187
160	GLY	8.818	175.002	45.669		108.837
161	LEU	9.289	176.127	55.174	44.117	128.734
162	LEU	8.640	175.679	54.359	39.345	121.804
163	GLY	9.430	176.452	46.542		106.205
164	ARG	9.918	177.286	51.527	28.676	122.752
165	TRP	8.403	175.789	57.036	29.684	122.108
166	GLY	9.243	169.752	41.382		113.779
167	PRO		175.016	61.828	30.732	
168	ASN	8.611	173.184	52.361	40.548	122.689
169	HIS	7.889	175.495	58.802	31.935	120.576
170	ALA	9.368	174.845	49.995	22.429	128.377
171	ALA	8.531	175.672	51.139	22.274	120.048
172	ASP	7.941	173.095	52.478	44.544	120.505
180	ARG	8.318	176.807	53.700	34.069	126.136

9 APPENDIX

no.	amino acid	ω				
		H	C	C α	C β	N
181	ASP	8.503	178.468	51.838	40.548	120.838
183	SER	8.125	174.059	58.162	63.399	117.753
184	GLY	8.029	174.524	44.835		109.152
185	ASN	8.488	175.495	52.536	38.685	122.412
186	LYS	8.395	176.500	57.095	32.051	120.804
187	ILE	8.425	174.941	60.567	38.957	123.917
188	MET	8.694	175.358	54.010	33.991	127.529
189	HIS	9.096	176.288	56.358	30.887	130.094
190	PRO		177.375	64.059	31.469	
191	VAL	9.496	177.662	63.729	32.167	121.252
192	SER	8.398	177.108	59.442	63.322	115.202
193	GLY		8.045	173.382	45.843	109.860
194	LYS	8.045	176.691	54.088	33.758	118.953
195	HIS	9.039	175.713	57.483	30.926	121.646
200	VAL	8.021	175.440	58.821	31.857	121.252
201	ALA	9.213	174.770	49.898	22.546	128.110
202	ILE	8.578	175.515	51.081	22.197	120.182
203	LYS	7.605	176.103	53.700	32.129	124.401
204	ARG	8.477	178.913	57.347	31.198	128.668
206	ASP	8.496	178.373	56.028	37.677	118.088
207	CYS	8.331	175.768	55.756	30.344	113.443
208	GLY	7.761	172.890	46.464		113.109
209	GLU	6.741	176.377	55.213	31.353	117.875
210	TRP	8.962	175.960	57.347	28.908	124.479
211	ALA	9.920	176.691	50.635	24.641	123.359
212	ILE	10.534	174.996	60.780	38.724	125.658
213	PRO		172.500	62.487	29.025	
214	GLY	7.122	174.032	44.796		104.839
215	GLY	8.372	170.552	44.951		106.905
216	MET	8.924	177.252	54.146	29.840	118.479
217	VAL	8.337	176.698	62.216	31.935	122.148
218	ASP	8.111	174.709	52.148	39.811	130.418
221	GLU	7.878	176.937	55.543	31.120	122.782
222	LYS	8.489	178.762	55.426	32.284	125.199
223	ILE	8.609	176.739	62.487	36.474	124.529
224	SER	8.058	176.407	61.149		114.739
225	ALA	7.140	180.506	54.165	17.541	124.908
226	THR	8.248	176.315	66.930	68.132	119.101
227	LEU	8.311	177.142	58.239	41.712	118.684
228	LYS	6.831	178.660	58.957	31.508	116.692
229	ARG	7.923	178.619	59.151	28.986	121.459
230	ILE	8.508	178.086	63.147	36.746	119.003
231	LEU	7.639	179.548	57.483	41.013	118.675
232	GLY	7.927	175.543	46.833		103.871
233	GLU	8.390	179.278	59.132	29.723	119.978
234	GLU	8.379	176.670	58.588	29.180	115.355
238	SER	8.588	176.315	61.227	62.158	113.764

9 APPENDIX

no.	amino acid	ω				
		H	C	C α	C β	N
239	LEU	8.233	179.125	56.687	40.548	120.091
240	GLN	7.498	175.611	54.262	27.822	116.361
241	LYS	7.028	177.081	53.603	32.594	119.420
242	THR	8.890	175.693	61.013	70.848	112.443
244	ALA	8.396	180.772	54.903	17.696	124.036
245	GLU	7.636	180.109	58.472	30.228	119.775
246	LYS	8.821	178.742	59.869	31.818	120.639
247	ARG	7.787	178.632	58.918	28.753	119.986
248	GLU	7.472	179.275	58.996	28.792	119.925
249	ILE	7.900	177.621	65.436	37.560	120.267
250	GLU	8.329	179.378	59.287	28.210	119.687
251	GLU	8.050	179.931	59.132	28.637	119.943
252	LYS	7.915	179.378	59.035	31.896	120.646
253	LEU	8.760	179.200	57.036	40.082	118.125
254	HIS	8.522	178.735	59.675	29.413	120.214
255	LYS	7.505	179.391	59.054	31.275	119.395
256	LEU	7.982	178.051	57.929	41.401	121.283
257	PHE	8.344	176.199	59.112	36.823	113.937
258	SER	7.485	174.859	58.841	63.166	114.632
259	GLN	7.400	175.214	55.000	29.723	120.503
260	ASP	8.405	174.729	55.058	40.548	120.144
261	HIS	7.843	173.710	54.068	30.848	119.381
262	LEU	7.948	176.226	52.885	44.621	119.781
263	VAL	9.094	175.426	64.098	29.956	127.757
264	ILE	8.566	174.989	58.685	36.202	129.916
265	TYR	7.530	172.213	57.929	41.091	118.091
266	LYS	7.247	174.456	53.971	35.116	125.818
267	GLY	8.854	173.034	43.496		106.821
268	TYR	8.689	175.378	60.819	39.849	121.889
269	VAL	8.179	173.485	61.227	33.487	130.862
270	ASP	7.411	171.441	52.691	38.802	125.824
271	ASP	7.040	174.319	49.199	45.358	126.935
272	PRO		174.640	63.302	30.771	
273	ARG	9.331	178.578	54.844	30.266	114.851
274	ASN	8.298	175.262	54.127	38.259	120.930
275	THR	10.235	175.543	59.325	71.818	113.279
276	ASP	9.755	177.525	57.366	40.354	118.809
277	ASN	9.159	173.023	52.070	43.923	113.277
278	ALA	8.129	173.929	51.488	22.003	125.556
279	TRP	7.752	173.540	56.804	31.275	119.250
280	MET	8.117	176.848	52.090	30.926	120.027
281	GLU	8.503	174.797	55.135	33.525	120.073
282	THR	8.845	173.799	58.045	70.499	113.942
283	GLU	7.366	173.492	56.881	30.228	123.897
284	ALA	7.422	173.478	56.804	30.228	123.827
285	VAL	8.049	173.444	60.489	34.922	123.748
286	ASN	9.261	173.519	50.286	43.263	125.149

9 APPENDIX

no.	amino acid	ω				
		H	C	C α	C β	N
288	HIS	8.484	173.874	54.204	34.767	123.845
289	ASP	8.137	175.296	51.100	40.858	127.385
290	GLU	8.339	176.130	58.045	29.413	125.131
291	THR	7.885	176.923	61.324	70.227	103.878
292	GLY	8.193	174.380	45.649		113.551
293	GLU	7.949	177.710	58.065	29.723	118.542
294	ILE	8.879	178.516	63.729	37.715	120.837
295	MET	8.948	178.940	54.631	30.422	115.451
296	ASP	8.019	177.081	56.862	39.578	121.016
297	ASN	7.833	174.360	52.594	38.685	115.059
298	LEU	7.185	175.522	54.185	42.100	121.510
299	MET	8.717	174.941	54.379	31.120	126.085
300	LEU	8.088	177.238	54.553	40.354	124.475
301	GLU	8.636	172.842	56.183	31.857	125.223
302	ALA	8.068	178.106	51.896	17.812	127.937
303	GLY	8.087	173.587	44.195		108.618
304	ASP	8.470	175.877	55.582	40.392	118.840
305	ASP	8.673	174.886	53.971	38.918	118.736
306	ALA	8.242	176.575	50.906	20.179	125.225
307	GLY	8.965	173.943	44.796		108.611
313	ASP	8.363	176.274	54.301	39.461	126.945
314	ILE	9.172	176.048	64.195	36.513	123.644
315	ASN	7.037	172.965	52.594	39.772	117.987
316	ASP	7.675	176.623	54.204	38.453	117.758
317	LYS	7.891	177.094	54.127	30.732	119.978
318	LEU	6.963	176.664	55.388	42.177	121.039
319	LYS	8.567	175.625	54.922	31.585	128.569
320	LEU	8.171	175.836	52.245	47.454	123.337
321	TYR	8.926	173.608	56.648	40.742	120.571
322	ALA	7.716	176.561	52.361	16.455	124.269
323	SER	6.139	174.606	55.776	60.955	112.399
324	HIS	8.613	178.448	58.414	32.206	121.527
325	SER	9.497	176.076	62.875	61.653	116.058
326	GLN	7.505	178.209	57.851	26.464	120.803
327	PHE	6.740	177.846	55.679	35.310	118.690
329	LYS	7.510	178.222	59.345	31.469	123.138
330	LEU	6.796	179.644	57.133	41.595	116.868
333	GLU	7.935	180.745	58.782	28.753	117.088
334	LYS	8.146	178.626	57.715	31.198	119.358
335	ARG	7.763	174.428	54.767	27.977	115.147
336	ASP	7.769	173.765	54.786	38.918	120.877
337	ALA	8.709	176.322	49.529	23.593	119.192
338	HIS	8.709	173.998	59.422	30.460	118.987
339	TRP	7.664	172.357	58.006		123.697
340	GLU	7.917	175.727	54.418	31.042	116.786
341	ASN	8.609	174.811	53.021	37.638	123.418
342	LEU	7.852	176.035	54.612	42.100	121.770

9 APPENDIX

no.	amino acid	ω				
		H	C	C α	C β	N
343	TYR	7.979	175.194	57.133	38.220	121.064
344	PHE	8.022	174.428	57.327	39.073	123.282
345	GLN	7.653	180.171	56.959	29.801	126.913

Acknowledgement

Above all, I would like to thank my supervisor Henning for his support throughout my whole PhD, his supervision and for the project. I would like to express the same thank you to Ralf. Thank you both for the freedom of independent scientific work in your labs, the helpful discussions, and all the knowledge you have given me. I was aiming for an interdisciplinary thesis - you really made that possible for me. I enjoyed the time and learned a lot.

More, I would like to thank the current and former Tidow lab members Kesha, Simon, Anne, Dominique, Katha, Julius, Steffi and Yasser for the teamwork, the help and discussions, and the great time together in- and outside the lab. I would also thank all the members of the Fliegert/Guse lab, especially Frederike, Franzi, Anke and Andreas who supported me a lot, especially when I was not allowed to do everything in the lab. Special thanks go to Trevor at the LMB for performing all of the NMR experiments that have contributed a lot to my work.

I would like to thank the Center of Ultrafast Imaging (CUI) and the CUI Graduate School, for the support in all aspects of my PhD training and of course for funding.

I thank all my friends, especially Tanita, Steffi, Jiny and Irina for your interest in my work and your mental support.

Mein besonderer Dank gilt meiner Familie, insbesondere meinen Papa und Birgit. Ihr habt mich während meines gesamten Studiums mental und finanziell unterstützt, mir immer interessiert zugehört und mich angespornt. Omi, du warst immer ein Vorbild mit deinem Tatendrang und deiner positiven Ausstrahlung für mich.

Zuletzt danke ich meinen beiden Jungs, meinem Sausewind und Sonnenschein Matthes und meinem Liebsten, Andre. Mit euch ist die Welt auch außerhalb des Labors spannend, abwechslungsreich und nie langweilig. Andre, durch deine Unterstützung kann ich beides haben: eine Familie und einen spannenden Beruf.

Eidesstattliche Versicherung

Hiermit versichere ich an Eides statt, die vorliegende Dissertation selbst verfasst und keine anderen als die angegebenen Hilfsmittel benutzt zu haben. Die eingereichte schriftliche Fassung entspricht der auf dem elektronischen Speichermedium. Ich versichere, dass diese Dissertation nicht in einem früheren Promotionsverfahren eingereicht wurde.

Hamburg, 10.5.2021

Ellen Gattkowski